

The Vera C. Rubin Observatory Data Preview 1

VERA C. RUBIN OBSERVATORY TEAM,¹ TATIANA ACERO-CUELLAR ,² EMILY ACOSTA ,¹ CHRISTINA L. ADAIR ,³
PRAKRUTH ADARI ,⁴ JENNIFER K. ADELMAN-MCCARTHY ,⁵ ANASTASIA ALEXOV ,¹ RUSS ALLBERRY ,¹
ROBYN ALLSMAN,¹ YUSRA ALSAYYAD ,⁶ JHONATAN AMADO ,⁵ NATHAN AMOUROUX ,⁷ PIERRE ANTILOGUS,⁸
ALEXIS ARACENA ALCAYAGA,⁹ GONZALO ARAVENA-ROJAS ,⁹ CLAUDIO H. ARAYA CORTES,⁹ ÉRIC AUBOURG ,¹⁰
TIM S. AXELROD ,¹¹ JOHN BANOVETZ ,¹² CARLOS BARRÍA,⁹ AMANDA E. BAUER ,¹³ BRIAN J. BAUMAN,¹⁴
ELLEN BECHTOL ,¹⁵ KEITH BECHTOL ,^{1,16} ANDREW C. BECKER ,¹⁷ VALERIE R. BECKER ,¹⁸ MARK G. BECKETT ,¹⁹
ERIC C. BELL ,²⁰ PEDRO H. BERNARDINELLI ,²¹ FEDERICA B. BIANCO ,^{2,22,23} ROBERT D. BLUM ,¹⁸
JOANNE BOGART,²⁴ ADAM BOLTON ,³ MICHAEL T. BOOTH,¹ JAMES F. BOSCH ,⁶ ALEXANDRE BOUCAUD ,²⁵
DOMINIQUE BOUTIGNY ,⁷ ROBERT A. BOVILL,¹ ANDREW BRADSHAW,^{3,24} JOHAN BREGEON ,²⁶ BRIAN J. BRONDEL ,²⁷
ALEX BROUGHTON ,²⁴ AUDREY BUDLONG,²⁸ DIMITRI BUFFAT,²⁶ RODOLFO CANESTRARI ,²⁹ NEVEN CAPLAR ,²⁰
JEFFREY L. CARLIN ,¹ ROSS CEBALLO ,¹⁸ COLIN ORION CHANDLER ,^{30,20,31} CHIHWAY CHANG ,³²
GLENAYER CHARLES-EMERSON,¹ HSIN-FANG CHIANG ,³ JAMES CHIANG ,²⁴ YUMI CHOI ,³³ ERIC J. CHRISTENSEN,⁹
CHARLES F. CLAVER,¹ ANDY W. CLEMENTS,¹ JOSEPH J. COCKRUM,¹ FRANCO COLLEONI,⁹ CÉLINE COMBET ,²⁶
ANDREW J. CONNOLLY ,²¹ JULIO EDUARDO CONSTANZO CÓRDOVA ,⁹ HANS E CONTRERAS,⁹
JOHN FRANKLIN CRENSHAW ,²¹ SYLVIE DAGORET-CAMPAGNE ,³⁴ SCOTT F. DANIEL,²⁰ FELIPE DARUICH,⁹
GUILLAUME DAUBARD ,⁸ GREG DAUES,³⁵ ERIK DENNHY ,¹ STEPHANIE JH DEPPE ,¹⁸ SETH W. DIGEL ,³
PETER E. DOHERTY,³⁶ ALEX DRLICA-WAGNER ,⁵ GREGORY P. DUBOIS-FELSMANN ,³⁷ FROSSIE ECONOMOU ,¹
ORION EIGER ,^{3,24} LUKAS EISERT ,³ ALAN M. EISNER ,³⁸ ANTHONY ENGLERT ,³⁹ BADEN ERB,⁹ JUAN A. FABREGA,⁹
PARKER FAGRELIUS,¹ KEVIN FANNING ,³ ANGELO FAUSTI NETO ,¹ PETER S. FERGUSON ,^{21,16} AGNÈS FERTÉ ,³
MERLIN FISHER-LEVINE ,⁴⁰ GLORIA FONSECA ALVAREZ ,³³ MICHAEL D. FOSS,³ DOMINIQUE FOUCHEZ ,⁴¹
DAN C. FUCHS ,³ EMMANUEL GANGLER ,⁴² IGOR GAPONENKO,³ JULEN GARCIA ,⁴³ JOHN H. GATES,³
RANPAL K. GILL ,²⁷ ENRICO GIRO ,⁴⁴ THOMAS GLANZMAN ,³ ROBINSON GODOY,⁹ IAIN GOODENOW,¹
MIRANDA R. GORSUCH ,¹⁶ MICHELLE GOWER ,³⁵ MIKAEL GRANVIK ,^{45,46} SARAH GREENSTREET ,³³ WEN GUAN ,¹²
THIBAULT GUILLEMIN ,⁷ LEANNE P. GUY ,⁹ DIANE HASCALL,³ AREN NATHANIEL HEINZE ,²¹ FABIO HERNANDEZ ,⁴⁷
KENNETH HERNER ,⁵ ARDIS HERROLD,¹ CLARE R. HIGGS ,¹⁸ JOSHUA HOBLITT ,¹ ERIN LEIGH HOWARD ,²⁰
MINHEE HYUN ,⁹ PATRICK INGRAHAM ,¹¹ DAVID H. IRVING ,¹⁸ ŽELJKO IVEŽIĆ ,^{1,20} SUZANNE H. JACOBY,¹
BUELL T. JANNUZI ,⁴⁸ SREEVANI JARUGULA ,⁵ M. JAMES JEE ,^{49,50} TIM JENNESS ,¹ TOBY C. JENNINGS ,³
ANDREA JEREMIE ,⁷ GARRETT JERNIGAN,^{51,*} DAVID JIMÉNEZ MEJÍAS,⁹ ANTHONY S. JOHNSON ,³ R. LYNNE JONES ,²⁰
ROGER WILLIAM LEWIS JONES ,⁵² CLAIRE JURAMY-GILLES ,⁸ MARIO JURIĆ ,²¹ STEVEN M. KAHN ,⁵³
J. BRYCE KALMBACH ,³ YIJUNG KANG ,^{24,9} ARUN KANNAWADI ,^{54,6} JEFFREY P. KANTOR,¹ EDWARD KARAVAKIS ,¹²
KSHITIJA KELKAR ,⁹ LEE S. KELVIN ,⁶ IVAN V. KOTOV,¹² GÁBOR KOVÁCS ,²¹ MIKOŁAJ KOWALIK ,³⁵
VICTOR L. KRABBENDAM,¹ K. SIMON KRUGHOFF ,^{1,*} PETR KUBÁNEK ,⁹ JACOB A. KURLANDER ,²¹ MILE KUSULJA,²⁶
CRAIG S. LAGE ,⁵⁰ P. J. A. LAGO ,²⁷ KATHERINE LALIOTIS ,⁵⁵ TRAVIS LANGE ,³ DIDIER LAPORTE,⁸
RYAN M. LAU ,³³ JUAN CARLOS LAZARTE,³ QUENTIN LE BOULC'H ,⁴⁷ PIERRE-FRANÇOIS LÉGET ,⁶
LAURENT LE GUILLOU ,⁸ BENJAMIN LEVINE ,⁴ MING LIANG,¹ SHUANG LIANG,³ KIAN-TAT LIM ,³
ANJA VON DER LINDEM ,⁴ HUAN LIN ,⁵ MARGAUX LOPEZ ,³ JUAN J. LOPEZ TORO,⁹ PETER LOVE,⁵²
ROBERT H. LUPTON ,⁶ NATE B. LUST ,⁶ LAUREN A. MACARTHUR ,⁶ SEAN PATRICK MACBRIDE ,⁵⁶
GREG M. MADEJSKI,²⁴ GABRIELE MAINETTI ,⁴⁷ STEVEN J. MARGHEIM ,²⁷ THOMAS W. MARKIEWICZ ,³
PHIL MARSHALL ,³ STUART MARSHALL,²⁴ GUIDO MAULEN,⁹ MORGAN MAY,^{57,12} JEREMY MCCORMICK ,³
DAVID MCKAY ,⁵⁸ ROBERT MCKERCHER,¹ GUILLEM MEGIAS HOMAR ,^{59,24} AARON M. MEISNER ,³³
FELIPE MENANTEAU,³⁵ HEATHER R. MENTZER ,³⁸ KRISTEN METZGER,¹⁸ JOSHUA E. MEYERS ,²⁴ MICHELLE MILLER,³³
DAVID J. MILLS,¹ JOACHIM MOEYENS ,²¹ MARC MONIEZ,³⁴ FRED E. MOOLEKAMP ,⁶⁰ C. A. L. MORALES MARÍN ,⁹
FRITZ MUELLER ,³ JAMES R. MULLANEY ,⁶¹ FREDDY MUÑOZ ARANCIBIA,¹ KATE NAPIER ,²⁴ HOMER NEAL,³
ERIC H. NEILSEN, JR. ,⁵ JEREMY NEVEU ,³⁴ TIMOTHY NOBLE,⁶² ERFAN NOURBAKHS ,⁶ KNUT OLSEN ,³³
WILLIAM O'MULLANE ,⁹ DMITRY ONOPRIENKO,³ MARCO ORIUNNO ,³ SHAWN OSIER,³ RUSSELL E. OWEN,²⁰
AASHAY PAI ,³² JOHN K. PAREJKO ,²⁰ HYE YUN PARK ,⁵⁴ JAMES B. PARSONS,^{35,*} MARIA T. PATTERSON ,²⁰
MARINA S. PAVLOVIC ,⁹ KARLA PEÑA RAMÍREZ ,⁹ JOHN R. PETERSON ,⁶³ STEPHEN R. PIETROWICZ ,³⁵
ANDRÉS A. PLAZAS MALAGÓN ,^{3,24} REBEKAH POLEN,⁵⁴ HANNAH MARY MARGARET POLLEK,³ PAUL A. PRICE ,⁶

50 BRUNO C. QUINT ,¹ JOSÉ MIGUEL QUINTERO MARIN,⁹ MARKUS RABUS ,⁶⁴ BENJAMIN RACINE ,⁴¹ VELJKO RADEKA,¹²
 51 MANON RAMEL,²⁶ ARIANNA RANABHAT ,⁶⁵ ANDREW P. RASMUSSEN ,²⁴ DAVID A. RATHFELDER,⁶⁶
 52 MEREDITH L. RAWLS ,^{20,21} SOPHIE L. REED ,⁶ KEVIN A. REIL ,³ DAVID J. REISS,²⁰ MICHAEL A. REUTER ,¹
 53 TIAGO RIBEIRO ,¹ MICKAEL RIGAULT ,⁶⁷ VINCENT J. RIOT ,¹⁴ STEVEN M. RITZ ,³⁸ MARIO F. RIVERA,⁹
 54 BRANT E. ROBERTSON ,³⁸ WILLIAM ROBY ,³⁷ GABRIELE RODEGHIERO ,⁶⁸ AARON ROODMAN ,²⁴
 55 LUCA ROSIGNOLI ,^{69,68} CÉCILE ROUCELLE ,²⁵ MATTHEW R. RUMORE ,¹² STEFANO RUSSO,⁸ ELI S. RYKOFF ,²⁴
 56 ANDREI SALNIKOV ,³ BRUNO O. SÁNCHEZ ,⁴¹ DAVID SANMARTIM ,⁹ CLARE SAUNDERS ,⁶ RAFE H. SCHINDLER,²⁴
 57 SAMUEL J. SCHMIDT ,⁵⁰ JACQUES SEBAG,⁹ BRIAN SELVY,¹ EDGARD ESTEBAN SEPULVEDA VALENZUELA,⁹
 58 GONZALO SERICHE ,⁹ JACQUELINE C. SERON-NAVARRETE ,⁹ IGNACIO SEVILLA-NOARBE ,⁷⁰ ALYSHA SHUGART ,⁹
 59 JONATHAN SICK ,^{71,1} CRISTIÁN SILVA ,⁹ MATHEW C. SIMS ,⁷² JALADH SINGHAL ,³⁷ KEVIN BENJAMIN SIRUNO,⁹
 60 COLIN T. SLATER ,²⁰ BRIANNA M. SMART ,²⁰ ADAM SNYDER ,⁵⁰ CHRISTINE SOLDAHL,³
 61 IOANA SOTUELA ELORRIAGA ,⁹ BRIAN STALDER ,¹ HERNAN STOCKEBRAND ,⁹ ALAN L. STRAUSS ,¹⁸
 62 MICHAEL A. STRAUSS ,⁶ KRZYSZTOF SUBERLAK ,²⁰ IAN S. SULLIVAN ,²⁰ JOHN D. SWINBANK ,^{73,6} DIEGO TAPIA ,⁹
 63 ALESSIO TARANTO ,^{68,69} DAN S. TARANU ,⁶ JOHN GREGG THAYER ,³ SANDRINE THOMAS ,¹
 64 ADAM J. THORNTON ,¹ ROBERTO TIGHE,⁹ LAURA TORIBIO SAN CIPRIANO,⁷⁰ TE-WEI TSAI ,¹ DOUGLAS L. TUCKER ,⁵
 65 MAX TURRI,³ J. ANTHONY TYSON ,⁵⁰ ELANA K. URBACH ,⁷⁴ YOUSUKE UTSUMI ,⁷⁵ BRIAN VAN KLAVEREN,³
 66 WOUTER VAN REEVEN ,⁹ PETER ANTHONY VAUCHER ,³ PAULINA VENEGAS,⁹ APRAJITA VERMA ,⁷⁶
 67 ANTONIA SIERRA VILLARREAL ,³ STELIOS VOUTSINAS ,¹ CHRISTOPHER W. WALTER ,⁵⁴ YUANKUN (DAVID) WANG ,²¹
 68 CHRISTOPHER Z. WATERS ,⁶ CHRISTINA C. WILLIAMS ,³³ BETH WILLMAN ,⁷⁷ MATTHIAS WITTGEN ,³
 69 W. M. WOOD-VASEY ,⁷⁸ WEI YANG ,³ ZHAOYU YANG ,¹² BRIAN P. YANNY ,⁵ PETER YOACHIM ,²⁰
 70 TIANQING ZHANG ,⁷⁸ AND CONGHAO ZHOU ,³⁸

¹ *Vera C. Rubin Observatory Project Office, 950 N. Cherry Ave., Tucson, AZ 85719, USA*

² *Department of Physics and Astronomy, University of Delaware, Newark, DE 19716-2570, USA*

³ *SLAC National Accelerator Laboratory, 2575 Sand Hill Rd., Menlo Park, CA 94025, USA*

⁴ *Department of Physics and Astronomy, Stony Brook University, Stony Brook, NY 11794, USA*

⁵ *Fermi National Accelerator Laboratory, P. O. Box 500, Batavia, IL 60510, USA*

⁶ *Department of Astrophysical Sciences, Princeton University, Princeton, NJ 08544, USA*

⁷ *Université Savoie Mont-Blanc, CNRS/IN2P3, LAPP, 9 Chemin de Bellevue, F-74940 Annecy-le-Vieux, France*

⁸ *Sorbonne Université, Université Paris Cité, CNRS/IN2P3, LPNHE, 4 place Jussieu, F-75005 Paris, France*

⁹ *Vera C. Rubin Observatory, Avenida Juan Cisternas #1500, La Serena, Chile*

¹⁰ *Université Paris Cité, CNRS/IN2P3, CEA, APC, 4 rue Elsa Morante, F-75013 Paris, France*

¹¹ *Steward Observatory, The University of Arizona, 933 N. Cherry Ave., Tucson, AZ 85721, USA*

¹² *Brookhaven National Laboratory, Upton, NY 11973, USA*

¹³ *Yerkes Observatory, 373 W. Geneva St., Williams Bay, WI 53191, USA*

¹⁴ *Lawrence Livermore National Laboratory, 7000 East Avenue, Livermore, CA 94550, USA*

¹⁵ *Wisconsin IceCube Particle Astrophysics Center, University of Wisconsin—Madison, Madison, WI 53706, USA*

¹⁶ *Department of Physics, University of Wisconsin-Madison, Madison, WI 53706, USA*

¹⁷ *Amazon Web Services, Seattle, WA 98121, USA*

¹⁸ *Vera C. Rubin Observatory/NSF NOIRLab, 950 N. Cherry Ave., Tucson, AZ 85719, USA*

¹⁹ *Institute for Astronomy, University of Edinburgh, Royal Observatory, Blackford Hill, Edinburgh EH9 3HJ, UK*

²⁰ *University of Washington, Dept. of Astronomy, Box 351580, Seattle, WA 98195, USA*

²¹ *Institute for Data-intensive Research in Astrophysics and Cosmology, University of Washington, 3910 15th Avenue NE, Seattle, WA 98195, USA*

²² *Joseph R. Biden, Jr., School of Public Policy and Administration, University of Delaware, Newark, DE 19717 USA*

²³ *Data Science Institute, University of Delaware, Newark, DE 19717 USA*

²⁴ *Kavli Institute for Particle Astrophysics and Cosmology, SLAC National Accelerator Laboratory, 2575 Sand Hill Rd., Menlo Park, CA 94025, USA*

²⁵ *Université Paris Cité, CNRS/IN2P3, APC, 4 rue Elsa Morante, F-75013 Paris, France*

²⁶ *Université Grenoble Alpes, CNRS/IN2P3, LPSC, 53 avenue des Martyrs, F-38026 Grenoble, France*

²⁷ *Vera C. Rubin Observatory/NSF NOIRLab, Casilla 603, La Serena, Chile*

²⁸ *University of Washington, Dept. of Physics, Box 351580, Seattle, WA 98195, USA*

²⁹ *INAF Istituto di Astrofisica Spaziale e Fisica Cosmica di Palermo, Via Ugo la Malfa 153, 90146, Palermo, Italy*

³⁰ *LSST Interdisciplinary Network for Collaboration and Computing, Tucson, USA*

³¹ *Department of Astronomy and Planetary Science, Northern Arizona University, P.O. Box 6010, Flagstaff, AZ 86011, USA*

³² *Department of Astronomy and Astrophysics, University of Chicago, 5640 South Ellis Avenue, Chicago, IL 60637, USA*

³³ *NSF NOIRLab, 950 N. Cherry Ave., Tucson, AZ 85719, USA*

106 ³⁴Université Paris-Saclay, CNRS/IN2P3, IJCLab, 15 Rue Georges Clemenceau, F-91405 Orsay, France
 107 ³⁵NCSA, University of Illinois at Urbana-Champaign, 1205 W. Clark St., Urbana, IL 61801, USA
 108 ³⁶Smithsonian Astrophysical Observatory, 60 Garden St., Cambridge MA 02138, USA
 109 ³⁷Caltech/IPAC, California Institute of Technology, MS 100-22, Pasadena, CA 91125-2200, USA

110 ³⁸Santa Cruz Institute for Particle Physics and Physics Department, University of California-Santa Cruz, 1156 High St., Santa Cruz,
 111 CA 95064, USA

112 ³⁹Department of Physics, Brown University, 182 Hope Street, Providence, RI 02912, USA

113 ⁴⁰D4D CONSULTING LTD., Suite 1 Second Floor, Everdene House, Deansleigh Road, Bournemouth, UK BH7 7DU

114 ⁴¹Aix Marseille Université, CNRS/IN2P3, CPPM, 163 avenue de Luminy, F-13288 Marseille, France

115 ⁴²Université Clermont Auvergne, CNRS/IN2P3, LPCA, 4 Avenue Blaise Pascal, F-63000 Clermont-Ferrand, France

116 ⁴³C. Iñaki Goenaga, 5, 20600, Guipúzcoa, Spain

117 ⁴⁴INAF Osservatorio Astronomico di Trieste, Via Giovan Battista Tiepolo 11, 34143, Trieste, Italy

118 ⁴⁵Department of Physics, P.O. Box 64, 00014 University of Helsinki, Finland

119 ⁴⁶Asteroid Engineering Laboratory, Luleå University of Technology, Box 848, SE-981 28 Kiruna, Sweden

120 ⁴⁷CNRS/IN2P3, CC-IN2P3, 21 avenue Pierre de Coubertin, F-69627 Villeurbanne, France

121 ⁴⁸University of Arizona, Department of Astronomy and Steward Observatory, 933 N. Cherry Ave, Tucson, AZ 85721, USA

122 ⁴⁹Department of Astronomy, Yonsei University, 50 Yonsei-ro, Seoul 03722, Republic of Korea

123 ⁵⁰Physics Department, University of California, One Shields Avenue, Davis, CA 95616, USA

124 ⁵¹Space Sciences Lab, University of California, 7 Gauss Way, Berkeley, CA 94720-7450, USA

125 ⁵²Lancaster University, Lancaster, UK

126 ⁵³Physics Department, University of California, 366 Physics North, MC 7300 Berkeley, CA 94720, USA

127 ⁵⁴Department of Physics, Duke University, Durham, NC 27708, USA

128 ⁵⁵Center for Cosmology and Astro-Particle Physics, The Ohio State University, Columbus, OH 43210, USA

129 ⁵⁶Physik-Institut, University of Zurich, Winterthurerstrasse 190, 8057 Zurich, Switzerland

130 ⁵⁷Department of Physics Columbia University, New York, NY 10027, USA

131 ⁵⁸EPCC, University of Edinburgh, 47 Potterrow, Edinburgh, EH8 9BT, UK

132 ⁵⁹Department of Aeronautics and Astronautics, Stanford University, Stanford, CA 94305, USA

133 ⁶⁰soZen Inc., 105 Clearview Dr, Penfield, NY 14526

134 ⁶¹Astrophysics Research Cluster, School of Mathematical and Physical Sciences, University of Sheffield, Sheffield, S3 7RH, United
 135 Kingdom

136 ⁶²Science and Technology Facilities Council, Rutherford Appleton Laboratory, Harwell, UK

137 ⁶³Department of Physics and Astronomy, Purdue University, 525 Northwestern Ave., West Lafayette, IN 47907, USA

138 ⁶⁴Departamento de Matemática y Física Aplicadas, Facultad de Ingeniería, Universidad Católica de la Santísima Concepción, Alonso de
 139 Rivera 2850, Concepción, Chile

140 ⁶⁵Australian Astronomical Optics, Macquarie University, North Ryde, NSW, Australia

141 ⁶⁶AURA, 950 N. Cherry Ave., Tucson, AZ 85719, USA

142 ⁶⁷Université Claude Bernard Lyon 1, CNRS/IN2P3, IP2I, 4 Rue Enrico Fermi, F-69622 Villeurbanne, France

143 ⁶⁸INAF Osservatorio di Astrofisica e Scienza dello Spazio Bologna, Via P. Gobetti 93/3, 40129, Bologna, Italy

144 ⁶⁹Department of Physics and Astronomy (DIFA), University of Bologna, Via P. Gobetti 93/2, 40129, Bologna, Italy

145 ⁷⁰Centro de Investigaciones Energéticas, Medioambientales y Tecnológicas, Av. Complutense 40, 28040 Madrid, Spain

146 ⁷¹J.Sick Codes Inc., Penetanguishene, Ontario, Canada

147 ⁷²Science and Technology Facilities Council, UK Research and Innovation, Polaris House, North Star Avenue, Swindon, SN2 1SZ, UK

148 ⁷³ASTRON, Oude Hoogeveensedijk 4, 7991 PD, Dwingeloo, The Netherlands

149 ⁷⁴Department of Physics, Harvard University, 17 Oxford St., Cambridge MA 02138, USA

150 ⁷⁵National Astronomical Observatory of Japan, Chile Observatory, Los Abedules 3085, Vitacura, Santiago, Chile

151 ⁷⁶Department of Physics, University of Oxford, Denys Wilkinson Building, Keble Road, Oxford, OX1 3RH, UK

152 ⁷⁷LSST Discovery Alliance, 933 N. Cherry Ave., Tucson, AZ 85719, USA

153 ⁷⁸Department of Physics and Astronomy, University of Pittsburgh, 3941 O'Hara Street, Pittsburgh, PA 15260, USA

154 (Dated: December 12, 2025)

ABSTRACT

155 We present Rubin Data Preview 1 (DP1), the first data from the NSF-DOE Vera C. Rubin Observatory, comprising raw and calibrated single-epoch images, coadds, difference images, detection
 156 catalogs, and ancillary data products. DP1 is based on 1792 optical/near-infrared exposures ac-
 157 quired over 48 distinct nights by the Rubin Commissioning Camera, LSSTComCam, on the Si-

159 Simonyi Survey Telescope at the Summit Facility on Cerro Pachón, Chile in late 2024. DP1 covers
 160 ~ 15 deg 2 distributed across seven roughly equal-sized non-contiguous fields, each independently ob-
 161 served in six broad photometric bands, *ugrizy*. The median FWHM of the point-spread function
 162 across all bands is approximately 1''.14, with the sharpest images reaching about 0''.58. The 5 σ point
 163 source depths for coadded images in the deepest field, Extended Chandra Deep Field South, are:
 164 $u = 24.55, g = 26.18, r = 25.96, i = 25.71, z = 25.07, y = 23.1$. Other fields are no more than 2.2
 165 magnitudes shallower in any band, where they have nonzero coverage. DP1 contains approximately
 166 2.3 million distinct astrophysical objects, of which 1.6 million are extended in at least one band in
 167 coadds, and 431 solar system objects, of which 93 are new discoveries. DP1 is approximately 3.5 TB
 168 in size and is available to Rubin data rights holders via the Rubin Science Platform, a cloud-based
 169 environment for the analysis of petascale astronomical data. While small compared to future LSST
 170 releases, its high quality and diversity of data support a broad range of early science investigations
 171 ahead of full operations in late 2025.

172 *Keywords:* Rubin Observatory – LSST

1. INTRODUCTION

173 The National Science Foundation (NSF)–Department
 174 of Energy (DOE) Vera C. Rubin Observatory is a
 175 ground-based, wide-field optical/near-infrared facility
 176 located on Cerro Pachón in northern Chile. Named in
 177 honor of Vera C. Rubin, a pioneering astronomer whose
 178 groundbreaking work in the 20th century provided the
 179 first convincing evidence for the existence of dark matter
 180 (V. C. Rubin & W. K. Ford 1970; V. C. Rubin et al.
 181 1980), the observatory’s prime mission is to carry out the
 182 Legacy Survey of Space and Time (formerly Large Syn-
 183 optic Survey Telescope) (LSST) (Ž. Ivezić et al. 2019a).
 184 This 10-year survey is designed to obtain rapid-cadence,
 185 multi-band imaging of the entire visible southern sky
 186 approximately every 3–4 nights. Over its main 18,000
 187 deg 2 footprint, the LSST is expected to reach a depth
 188 of ~ 27 magnitude in the r-band, with ~ 800 visits per
 189 pointing in all filters (F. B. Bianco et al. 2022).

190 The Rubin Observatory system consists of four main
 191 components: the Simonyi Survey Telescope, featuring
 192 an 8.4 m diameter (6.5 m effective aperture) primary
 193 mirror that delivers a wide field of view; a 3.2-gigapixel
 194 camera, capable of imaging 9.6 square degrees per
 195 exposure⁷⁹ with seeing-limited quality in six broadband
 196 filters, *ugrizy* (320–1050 nm); an automated Data Man-
 197 agement System that processes and archives tens of ter-
 198 abytes of data per night, generating science-ready data
 199 products within minutes for a global community of sci-
 200 entists; and an Education and Public Outreach (EPO)

202 program that provides real-time data access, interactive
 203 tools, and educational content to engage the public. The
 204 integrated system’s étendue⁸⁰ of 319 m 2 deg 2 , is over an
 205 order of magnitude larger than that of any previous op-
 206 tical observatory, enabling a fast, large-scale survey with
 207 exceptional depth in a fraction of the time compared to
 208 other observatories.

209 The observatory’s design is driven by four key science
 210 themes: probing dark energy and dark matter; taking
 211 an inventory of the solar system; exploring the tran-
 212 sient and variable optical sky; and mapping the Milky
 213 Way (Ž. Ivezić et al. 2019a). These themes inform the
 214 optimization of a range of system parameters, includ-
 215 ing image quality, photometric and astrometric accu-
 216 racy, the depth of a single visit and the co-added survey
 217 depth, the filter complement, the total number of visits
 218 per pointing as well as the distribution of visits on the
 219 sky, and total sky coverage. Additionally, they inform
 220 the design of the data processing and access systems.
 221 By optimizing the system parameters to support a wide
 222 range of scientific goals, we maximize the observatory’s
 223 scientific output across all areas, making Rubin a pow-
 224 erful discovery machine capable of addressing a broad
 225 range of astrophysical questions.

226 Throughout the duration of the LSST, Rubin Obser-
 227 vatory will issue a series of Data Releases, each repre-
 228 senting a complete reprocessing of all LSST data col-
 229 lected up to that point. Prior to the start of the LSST
 230 survey, commissioning activities will generate a signifi-
 231 cant volume of science-grade data. To make this early
 232 data available to the community, the Rubin Early Sci-
 233 ence Program (L. P. Guy et al. 2025) was established.

^{*} Author is deceased

⁷⁹ We define an “exposure” as the process of exposing all detectors in the focal plane. It is synonymous with the term “visit” in DP1. By contrast, an “image” is the output of a single detector following an exposure.

⁸⁰ The product of the primary mirror area and the angular area of its field of view for a given set of observing conditions.

234 One key component of this program is a series of Data
 235 Previews; early versions of the **LSST** Data Releases.
 236 These previews include preliminary data products de-
 237 rived from both simulated and commissioning data,
 238 which, together with early versions of the data access
 239 services, are intended to support high-impact early sci-
 240 ence, facilitate community readiness, and inform the de-
 241 velopment of Rubin’s operational capabilities ahead of
 242 the start of full survey operations. All data and services
 243 provided through the Rubin Early Science Program are
 244 offered on a shared-risk basis⁸¹.

245 This paper describes Rubin’s second of three planned
 246 Data Previews: **Data Preview 1 (DP1)** (NSF-DOE Vera
 247 C. Rubin Observatory 2025a). The first, **Data Preview**
 248 **0 (DP0)**⁸², contained data products produced from the
 249 processing of simulated **LSST**-like data sets, together
 250 with a very early version of the Rubin **Science Platform**
 251 (M. Jurić et al. 2019). **DP1** contains data products de-
 252 rived from the reprocessing of science-grade exposures
 253 acquired by the **Rubin Commissioning Camera (LSST-
 254 ComCam)**, in late 2024. The third and final Data Pre-
 255 view, **Data Preview 2 (DP2)**, is planned to be based
 256 on a reprocessing of all science-grade data taken with
 257 the Rubin’s **LSST Science Camera (LSSTCam)** during
 258 commissioning.

259 All Rubin Data Releases and Previews are subject
 260 to a two-year proprietary period, with immediate ac-
 261 cess granted exclusively to LSST data rights holders (R.
 262 Blum & the Rubin Operations Team 2020). Data rights
 263 holders⁸³ are individuals or institutions with formal au-
 264 thorization to access proprietary data collected by the
 265 Vera C. Rubin Observatory. After the two-year propri-
 266 etary period, **DP1** will be made public.

267 In this paper, we present the contents and validation
 268 of, and the data access and community support ser-
 269 vices for, Rubin **DP1**, the first Data Preview to deliver
 270 data derived from observations conducted by the Vera
 271 C. Rubin Observatory. **DP1** is based on the reprocess-
 272 ing of 1792 science-grade exposures acquired during the
 273 first on-sky commissioning campaign conducted in late
 274 2024. It covers a total area of approximately ~ 15 deg 2
 275 distributed across seven distinct non-contiguous fields.
 276 The data products include raw and calibrated single-
 277 epoch images, coadded images, difference images, de-
 278 tection catalogs, and other derived data products. **DP1**

⁸¹ Shared risk means early access with caveats: the community benefits from getting a head start on science, preparing analyses, and providing feedback, while also accepting that the system may not work as well as it will during full operations.

⁸² See <https://dp0.lsst.io>

⁸³ See <https://www.lsst.org/scientists/international-drh-list>

279 is about 3.5 TB in size and contains around 2.3 million
 280 distinct astronomical objects, detected in 2644 coadded
 281 images. Full **DP1** release documentation is available at
 282 <https://dp1.lsst.io>. Despite Rubin Observatory still be-
 283 ing in commissioning and not yet complete at the time
 284 the observations were acquired, Rubin **DP1** provides an
 285 important first look at the data, showcasing its charac-
 286 teristics and capabilities.

287 The structure of this paper is as follows. In section
 288 **2** we describe the observatory system and overall con-
 289 struction and commissioning status at the time of data
 290 acquisition, the seven fields included in **DP1**, and the
 291 observing strategy used. Section **3** summarizes the con-
 292 tents of **DP1** and the data products contained in the
 293 release. The data processing pipelines are described in
 294 section **4**, followed by a description of the data valida-
 295 tion and performance assessment in section **5**. Section
 296 **6** describes the Rubin **Science Platform** (RSP), a cloud-
 297 based data science infrastructure that provides tools and
 298 services to Rubin data rights holders to access, visual-
 299 ize and analyze peta-scale data generated by the **LSST**.
 300 Section **7** presents the Rubin Observatory’s model for
 301 community support, which emphasizes self-help via doc-
 302 umentation and tutorials, and employs an open platform
 303 for issue reporting that enables crowd-sourced solutions.
 304 Finally, a summary of the **DP1** release and information
 305 on expected future releases of data is given in section **8**.
 306 The appendix contains a useful glossary of terms used
 307 throughout this paper.

308 All magnitudes quoted are in the AB system (J. B.
 309 Oke & J. E. Gunn 1983), unless otherwise specified.

2. ON-SKY COMMISSIONING CAMPAIGN

310 The first Rubin on-sky commissioning campaign was
 311 conducted using the **LSSTComCam**. The campaign’s
 312 primary objective was to optically align the Simonyi
 313 Survey Telescope and verify its ability to deliver accept-
 314 able image quality using **LSSTComCam**. In addition,
 315 the campaign provided valuable operations experience
 316 to facilitate commissioning the full **LSSTCam** (T. Lange
 317 et al. 2024; A. Roodman et al. 2024). We note that
 318 commissioning **LSSTComCam** was not an objective of
 319 the campaign. Instead, **LSSTComCam** was used as a
 320 tool to support broader observatory commissioning, in-
 321 cluding early testing of the **Active Optics System (AOS)**
 322 and the LSST Science Pipelines. As a result, many arti-
 323 facts present in the data are specific to **LSSTComCam**
 324 and will be addressed only if they persist with **LSST-
 325 Cam**. Accordingly, the image quality achieved during
 326 this campaign, and in the **DP1** data, do not reflect the
 327 performance ultimately expected from **LSSTCam**.

329 Approximately 16,000 exposures were collected during
 330 this campaign, the majority in support of [AOS](#) commis-
 331 sioning, system-level verification, and end-to-end testing
 332 of the telescope’s hardware and software. This included
 333 over 10000 exposures for [AOS](#) commissioning, more than
 334 2000 bias and dark calibration frames, and over 2000
 335 exposures dedicated to commissioning the LSST Sci-
 336 ence Pipelines. For [DP1](#), we have selected a subset of
 337 1792 science-grade exposures from this campaign that
 338 are most useful for the community to begin preparing
 339 for early science.

340 At the time of the campaign, the observatory was
 341 still under construction, with several key components,
 342 such as dome thermal control, full mirror control, and
 343 the final [AOS](#) configuration either incomplete or still
 344 undergoing commissioning. As a result, image qual-
 345 ity varied widely throughout the campaign and exhib-
 346 ited a broader distribution than is expected with [LSST-
 347 Cam](#). Despite these limitations, the campaign suc-
 348 cessfully demonstrated system integration and established a
 349 functional observatory.

350 2.1. *Simonyi Survey Telescope*

351 The Simonyi Survey Telescope ([B. Stalder et al. 2024](#))
 352 features a unique three-mirror design, including an 8.4-
 353 meter [Primary Mirror Tertiary Mirror \(M1M3\)](#) fabri-
 354 cated from a single substrate, and a 3.5-meter [Secondary](#)
 355 [Mirror \(M2\)](#). This compact [configuration](#) supports a
 356 wide 3.5-degree field of view while enabling exceptional
 357 stability, allowing the telescope to slew and settle in under
 358 five seconds. To achieve the scientific goals of the
 359 10-year [LSST](#), the Observatory must maintain high im-
 360 age quality across its wide field of view ([Ž. Ivezić et al.](#)
 361 2019b). This is accomplished through the [AOS](#) ([B. Xin et al. 2015; G. Megias Homar et al. 2024](#)), which cor-
 362 rects, between successive exposures, wavefront distor-
 363 tions caused by optical misalignments and mirror surface
 364 deformations, primarily due to the effect of gravitational
 365 and thermal loads.

366 The [AOS](#), which comprises an open-loop component
 367 and a closed-loop component, optimizes image qual-
 368 ity by aligning the camera and [M2](#) relative to [M1M3](#),
 369 as well as adjusting the shapes of all three mirrors
 370 to nanometer precision. The [AOS](#) open-loop compo-
 371 nent corrects for predictable distortions and misalign-
 372 ments, while the closed-loop component addresses un-
 373 predictable or slowly varying aberrations using feed-
 374 back from the corner wavefront sensors. The closed-
 375 loop wavefront sensing technique is curvature wavefront
 376 sensing, which infers wavefront errors in the optical sys-
 377 tem by analyzing extra- and intra-focal star images ([S.](#)
 378 [Thomas et al. 2023](#)). Since [LSSTComCam](#) lacks dedi-

380 cated wavefront sensors, wavefront errors were instead
 381 estimated by defocusing the telescope ± 1.5 mm on ei-
 382 ther side of focus and applying the curvature wavefront
 383 sensing pipeline to the resulting images. Each night be-
 384 gan with an initial alignment correction using a laser
 385 tracker to position the system within the capture range
 386 of the closed-loop [algorithm](#) ([G. Megias Homar et al.](#)
 387 2024). Once this coarse alignment was complete, the
 388 [AOS](#) refined the optical alignment and applied mirror
 389 surfaces corrections to optimize the image quality across
 390 the [LSSTComCam](#) field of view.

391 During LSST [Science Pipelines](#) commissioning ([§2.4](#)),
 392 observations were conducted using the [AOS](#) in open-
 393 loop mode only, without closed-loop corrections between
 394 exposures. Closed-loop operation, which requires ad-
 395 ditional intra- and extra-focal images with [LSSTCom-
 396 Cam](#), was not compatible with the continuous data ac-
 397 quisition needed by the pipelines. The image quality
 398 for these data was monitored by measuring the [Point](#)
 399 [Spread Function \(PSF\) Full Width at Half-Maximum](#)
 400 ([FWHM](#)), and closed-loop sequences were periodically
 401 run when image quality degradation was observed.

402 2.2. *The LSST Commissioning Camera*

403 [LSSTComCam](#) ([B. Stalder et al. 2022, 2020; J.](#)
 404 [Howard et al. 2018; SLAC National Accelerator Lab-](#)
 405 [oratory & NSF-DOE Vera C. Rubin Observatory 2024](#))
 406 is a 144-megapixel version of the 3.2-gigapixel [LSST-
 407 Cam](#). It covers approximately 5% of the [LSSTCam](#) focal
 408 plane area, with a field of view of ~ 0.5 deg 2 (40'x40'),
 409 compared to LSSTCam’s 9.6 deg 2 . It was developed to
 410 validate camera interfaces with other observatory com-
 411 ponents and evaluate overall system performance prior
 412 to the start of [LSSTCam](#) commissioning. Although it
 413 has a smaller imaging area, [LSSTComCam](#) shares the
 414 same plate scale of 0''.2 per pixel and is housed in a sup-
 415 port structure that precisely replicates the total mass,
 416 center of gravity, and physical dimensions of [LSSTCam](#).
 417 All mechanical and utility interfaces to the telescope are
 418 implemented identically, enabling full end-to-end test-
 419 ing of observatory systems, including readout electron-
 420 ics, image acquisition, and data pipelines.

421 The [LSSTCam](#) focal plane is composed of 25 modular
 422 [rafts](#) arranged in a 5x5 grid; 21 [rafts](#) are dedicated to
 423 science imaging, while four corner [rafts](#) are used for guid-
 424 ing and wavefront sensing. Each science [raft](#) is a self-
 425 contained unit comprising nine 4Kx4K [Charge-Coupled](#)
 426 [Device \(CCD\)](#) ([G. E. Smith 2010](#)) sensors arranged in a
 427 3x3 mosaic, complete with integrated readout electron-
 428 ics and cooling systems. Each sensor is subdivided into
 429 16 segments arranged in a 2x8 layout, with each seg-
 430 ment consisting of 512x2048 pixels and read out in par-

allel using individual amplifiers. LSSTCam uses CCD sensors from two vendors: Imaging Technology Laboratory, University of Arizona (UA)) (ITL) and Teledyne (E2V). To maintain uniform performance and calibration each raft is populated with sensors from only one vendor.

LSSTComCam consists of a single science raft equipped exclusively with ITL sensors. The sensors selected for LSSTComCam represent the best performing of the remaining ITL devices after the LSSTCam rafts were fully populated. They exhibit known issues such as high readout noise (e.g., Detector 8, S22 in Figure 2) and elevated Charge Transfer Inefficiency (CTI) (e.g., Detector 5, S12 in Figure 2). As a result, certain image artifacts present in the DP1 dataset may be specific to LSSTComCam. Although the cryostat in LSSTComCam, uses a different cooling system than that of LSSTCam, LSSTComCam incorporated a refrigeration pathfinder to validate the cryogenic refrigeration system intended for LSSTCam,. Figure 1 shows the single-raft LSSTComCam positioned at the center of the full LSSTCam focal plane, corresponding to the central science raft position. LSSTComCam is designated as Raft 22 (R22).

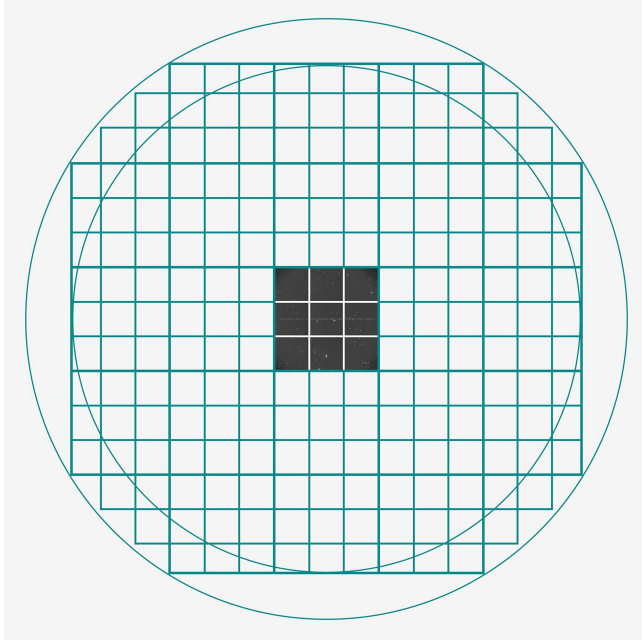


Figure 1. Schematic showing the single-raft LSSTComCam positioned at the center of the full LSSTCam focal plane. The perspective is from above, looking down through the LSSTComCam lenses onto the focal plane. Credit: RubinObs/NOIRLab/SLAC/NSF/DOE/AURA.

The LSSTCam and LSSTComCam focal planes are described in detail in A. A. Plazas Malagón et al. (2025).

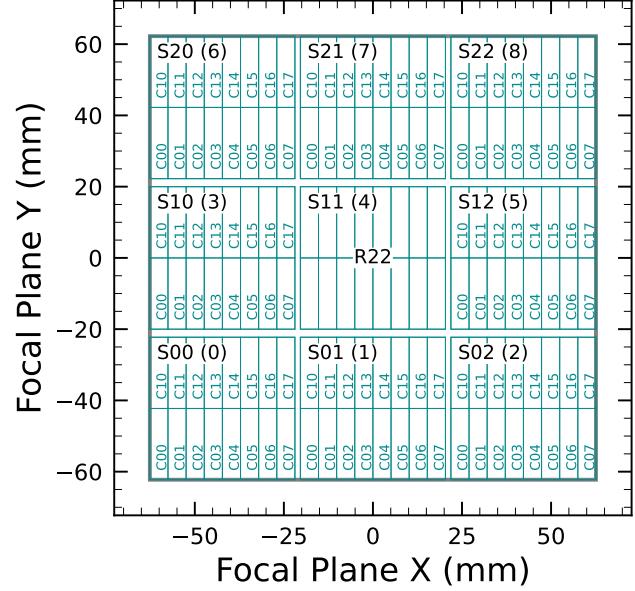


Figure 2. LSSTComCam focal plane layout illustrating the placement and numbering scheme of sensors (S) and amplifiers (C). The view is looking down from above the focal plane through the LSSTComCam lenses. Each sensor contains 16 amplifiers, and a group of nine sensors comprises one raft. LSSTComCam is Raft 22 (R22). The detector number for each sensor is shown in parentheses.

2.2.1. Filter Complement

LSSTComCam supports imaging with six broadband filters *ugrizy* spanning 320–1050 nm, identical in design to LSSTCam. Whereas the LSSTCam filter exchanger holds five filters, the LSSTComCam exchanger holds only three at a time. The full-system throughput of the six LSSTComCam filters, which encompasses contributions from a standard atmosphere at airmass 1.2, telescope optics, camera surfaces, and the mean ITL detector quantum efficiency is shown in Figure 3.

2.2.2. Timing Calibration

The absolute time accuracy of data taken with LSSTComCam relies on the Network Time Protocol (NTP) for clock synchronization, which should be accurate to approximately 1 millisecond. In order to evaluate the absolute timing accuracy of the entire system we observed the geosynchronous satellite EUTELSAT 117 West B with a set of 10 usable 10-second exposures over two nights. EUTELSAT 117 West B is part the GPS system and serves as one of the WAAS (Wide Area Augmentation System) satellites operated for the U.S. Federal Aviation Administration (FAA) and used to broadcast GPS corrections to air traffic.

As these satellites are part of the GPS system, their positions are tracked very precisely and the record of

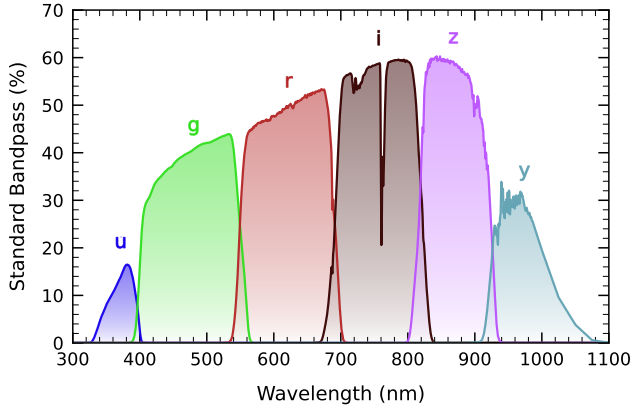


Figure 3. LSSTComCam standard bandpasses, illustrating full system throughput. The bandpasses include a standard atmosphere at airmass 1.2, telescope optics, camera surfaces, and mean ITL detector quantum efficiency.

their locations is published after the fact and can be downloaded. Following the technique previously employed by other surveys, (J. L. Tonry et al. 2018), we observed the satellite while tracking the sky and then downloaded the data-files with its precise locations from the National Satellite Test Bed web site⁸⁴. By comparing the measured and predicted locations of the start of the satellite track on the sky, we determined that (relative to the start of integration-time recorded in the FITS headers) our time was accurate to 53.6 ± 11.0 milliseconds.

This work continues to be an area of ongoing study, as the exact timing of when the shutter open command is issued, and the complete profile of the shutter movement are not yet determined. However the open command is on average near 29 milliseconds later. Incorporating the delays into the fit reduces the offset to 24.8 ± 11.0 milliseconds.

The full shutter takes approximately 396 milliseconds to completely open. As the LSSTComCam sensors are centered in the aperture, the center of the focal plane should be exposed about half-way through the shutter open procedure, 198 milliseconds after the open command. There are uncertainties on the full motion profile, and the blade direction motions are currently not known, but the fraction of the shutter aperture subtended by the focal plane is 52%. This implies that the shutter will pass any pixel between 198 ± 103 milliseconds. Subtracting this from the fitted delay of 24.8 milliseconds and adding the fitted error of 11.0 milliseconds in quadrature, results in a current conservative estimate

of the delay of -173.2 ± 104.1 milliseconds, consistent with and smaller than the constraints on the timing offset determined using astrometric residuals from known asteroid associations presented in §5.10.2.

2.3. Flat Field System

During the on-sky campaign, key components of the Rubin calibration system (P. Ingraham et al. 2022), including the flat field screen, had not yet been installed. As a result, flat fielding for DP1 relied entirely on twilight flats. While twilight flats pose challenges such as non-uniform illumination and star print-through, they were the only available option during LSSTComCam commissioning and for DP1 processing. To mitigate these limitations, dithered, tracked exposures were taken over a broad range of azimuth and rotator angles to construct combined flat calibration frames. Exposure times were dynamically adjusted to reach target signal levels of between 10,000 and 20,000 electrons. Future campaigns will benefit from more stable and uniform flat fielding using the Rubin flat field system, described in P. Fagrelius & E. S. Rykoff (2025).

2.4. LSST Science Pipelines Commissioning

Commissioning of the LSST Science Pipelines, (Rubin Observatory Science Pipelines Developers 2025), began once the telescope was able to routinely deliver sub-arcsecond image quality. The goals included testing the internal astrometric and photometric calibration across a range of observing conditions, validating the difference image analysis and Prompt Processing (K.-T. Lim 2023) framework, and accumulating over 200 visits per band to evaluate deep coadded images with integrated exposure times roughly equivalent to those of the planned LSST Wide Fast Deep (WFD) 10-year depth. To support these goals, seven target fields were selected that span a range of stellar densities, overlap with external reference datasets, and collectively span the full breadth of the four primary LSST science themes. These seven fields form the basis of the DP1 dataset. Figure 4 shows the locations of these seven fields on the sky, overlaid on the LSST baseline survey footprint (R. L. Jones et al. 2021; P. Yoachim 2022; Rubin’s Survey Cadence Optimization Committee et al. 2022, 2023, 2025), along with sky coverage of both the LSSTCam and LSSTComCam focal planes.

Each of the seven target fields was observed repeatedly in multiple bands over many nights. A typical observing epoch on a given target field consisted of 5-20 visits in each of the three loaded filters (§2.2.1). All DP1 images were captured as single 1×30 -second exposures for all bands, rather than as 2×15 -second “snap” exposures. Additionally, some *u*-band exposures were taken

⁸⁴ <https://www.nstb.tc.faa.gov/nstbarchive.html>

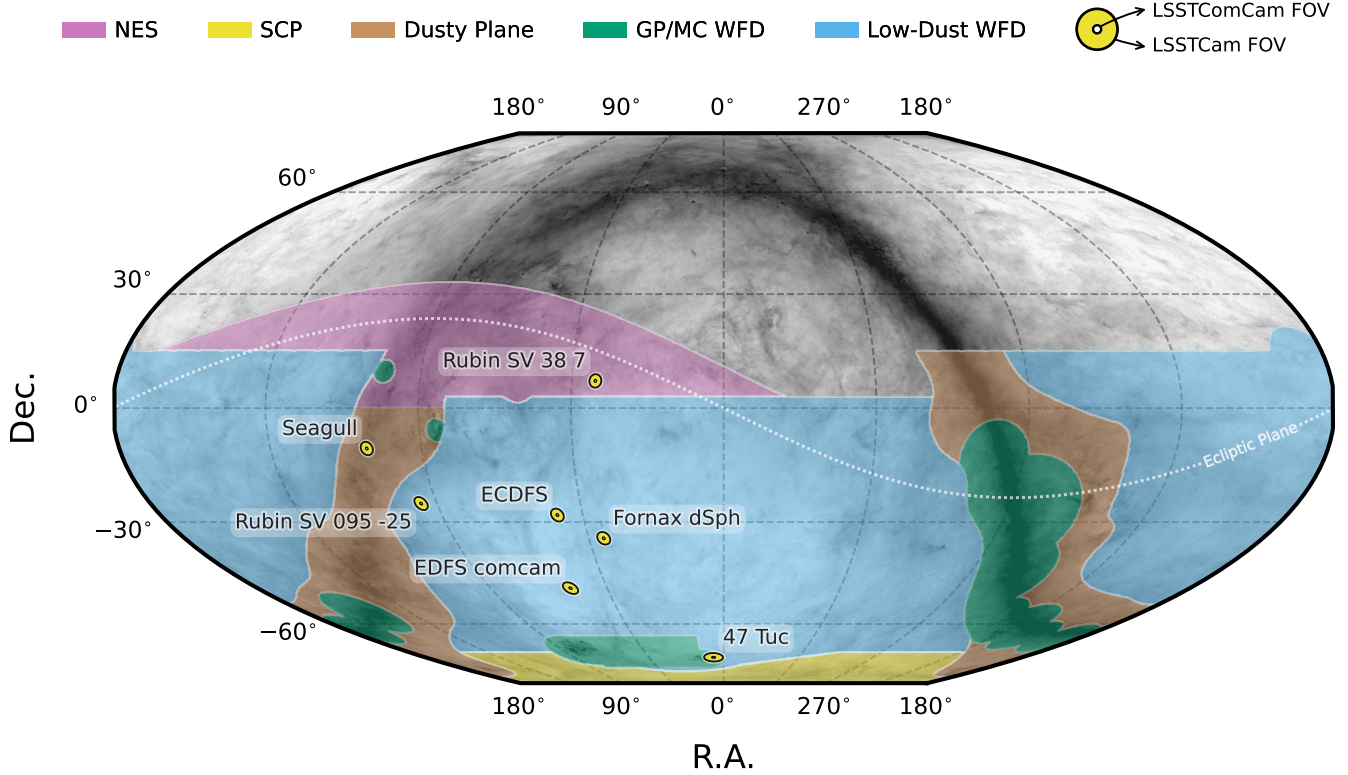


Figure 4. Locations of the seven DP1 fields overlaid on the LSST baseline survey footprint (Rubin’s Survey Cadence Optimization Committee et al. 2025). NES: North Ecliptic Spur, SCP: South Celestial Pole, Low-Dust WFD: regions away from the Galactic Plane (GP) observed with a WFD cadence, GP/MC WFD: Galactic Plane and Magellanic Clouds regions observed with a WFD cadence. The fields of view covered by the LSSTCam and LSSTComCam focal planes are represented as outer and inner concentric circles, respectively, centered on the pointing center of each field.

as 38-second exposures. The exposure time for LSST images will be determined following further testing during the commissioning phase with LSSTCam. All images were acquired using the Rubin Feature-Based Scheduler (FBS), version 3.0 (E. Naghib et al. 2019; P. Yoachim et al. 2024). Table 1 lists the seven DP1 fields and their pointing centers, and provides a summary of the band coverage in each.

The temporal sampling distribution of observations per band and per night is shown in Figure 5. Gaps in coverage across some bands arise from the fact that LSSTComCam can only hold three filters at a time (see §2.2.1). As the campaign progressed, the temporal sampling became denser across all fields, reflecting improved efficiency and increased time allocated for science observations.

It is important to note that the time sampling in the DP1 dataset differs significantly from what will be seen in the final LSST data. Table 2 lists the 5σ point source depths for coadded images per field and per band, where coverage in a band is non-zero.

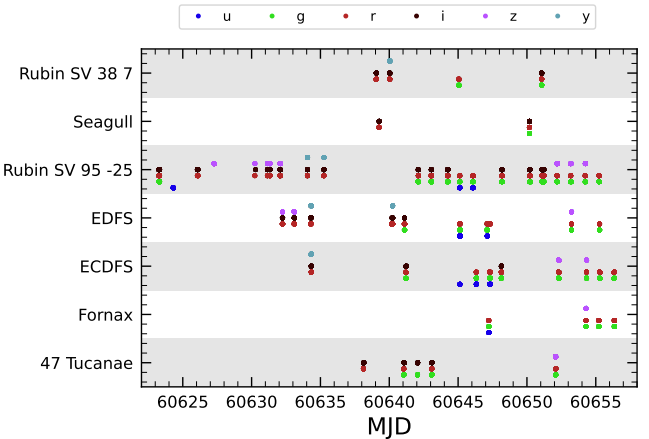


Figure 5. Distribution of DP1 observations by date grouped by field as a function of time over the 48 nights of data taking with LSSTComCam. Each dot represents a single exposure, color-coded by band.

All fields except for the low ecliptic latitude field, Rubin_SV_38_7, used a small random dithering pattern. The random translational dithers of the telescope bore-

Table 1. DP1 fields and pointing centers with the number of exposures in each band per field. ICRS coordinates are in units of decimal degrees, and are specified as J2000.

Field Code	Field Name	RA	DEC	Band						Total
		deg	deg	<i>u</i>	<i>g</i>	<i>r</i>	<i>i</i>	<i>z</i>	<i>y</i>	
47_Tuc	47 Tucanae Globular Cluster	6.128	-72.090	6	10	32	19	0	5	72
ECDFS	Extended Chandra Deep Field South	53.160	-28.100	43	230	237	162	153	30	855
EDFS_comcam	Rubin SV Euclid Deep Field South	59.150	-48.730	20	61	87	42	42	20	272
Fornax_dSph	Fornax Dwarf Spheroidal Galaxy	40.080	-34.450	0	5	25	12	0	0	42
Rubin_SV_095_-25	Rubin SV Low Galactic Latitude Field	95.040	-25.000	33	82	84	23	60	10	292
Rubin_SV_38_7	Rubin SV Low Ecliptic Latitude Field	37.980	7.015	0	44	40	55	20	0	159
Seagull	Seagull Nebula	106.300	-10.510	10	37	43	0	10	0	100
Total				112	469	548	313	285	65	1792

Table 2. Median 5σ coadd point source detection limits per field and band.

Field Code	Band					
	<i>u</i>	<i>g</i>	<i>r</i>	<i>i</i>	<i>z</i>	<i>y</i>
47_Tuc	-	24.03	24.24	23.90	-	21.79
ECDFS	24.55	26.18	25.96	25.71	25.07	23.10
EDFS_comcam	23.42	25.77	25.72	25.17	24.47	23.14
Fornax_dSph	-	24.53	25.07	24.64	-	-
Rubin_SV_095_-25	24.29	25.46	24.95	24.86	24.32	22.68
Rubin_SV_38_7	-	25.46	25.15	24.86	23.52	-
Seagull	23.51	24.72	24.19	-	23.30	-

sight were applied for each visit, with offsets of up to 0.2 degrees around the pointing center (Table 1). The rotational dithers of the camera rotator were typically approximately 1 degree per visit, with larger random offsets at each filter change, which worked to keep operational efficiency high. The Rubin_SV_38_7 field used a different dither pattern to optimize coverage of Solar System Objects and test Solar System Object linking across multiple nights. These observations used a 2×2 grid of LSSTComCam pointings to cover an area of about 1.3 degree \times 1.3 degrees. The visits cycled between the grid’s four pointing centers, using small random translational dithers to fill chip gaps with the goal of acquiring 3-4 visits per pointing center per band in each observing epoch.

2.5. Delivered Image Quality

The delivered image quality is influenced by contributions from both the observing system (i.e., dome, telescope and camera) and the atmosphere. During the

campaign, the Rubin Differential Image Motion Monitor (DIMM) was not operational, so atmospheric seeing was estimated using live data from the Southern Astrophysical Research Telescope (SOAR) Ring-Image Next Generation Scintillation Sensor (RINGSS) seeing monitor, also located on Cerro Pachón. Although accelerometers mounted on the mirror cell and top-end assembly were available to track dynamic optics effects, such as mirror oscillations that can degrade optical alignment, this data was not used during the campaign. Mount encoder data were used to measure the mount jitter in every image, with a measured median contribution of 0.004 arcseconds to image degradation. As the pointing model was not fine-tuned, tracking errors could range from 0.2 to 0.4 arcseconds per image, depending on RA and Dec. Dome and mirror-induced seeing were not measured during the campaign.

The DP1 median delivered image quality across all bands is $1.^{\prime\prime}14$, as measured by the PSF FWHM. The best images achieved a PSF FWHM of approximately $0.^{\prime\prime}58$. Ongoing efforts aim to quantify all sources of image degradation, including contributions from the camera system, static and dynamic optical components, telescope mount motion, observatory-induced seeing from the dome and mirror, and atmospheric conditions.

3. OVERVIEW OF THE CONTENTS OF RUBIN DP1

Here we describe Rubin DP1 data products and provide summary statistics for each, but we also refer the reader to the DOI-registered DP1 release documentation available at <https://dp1.lsst.io> and the catalog schemas

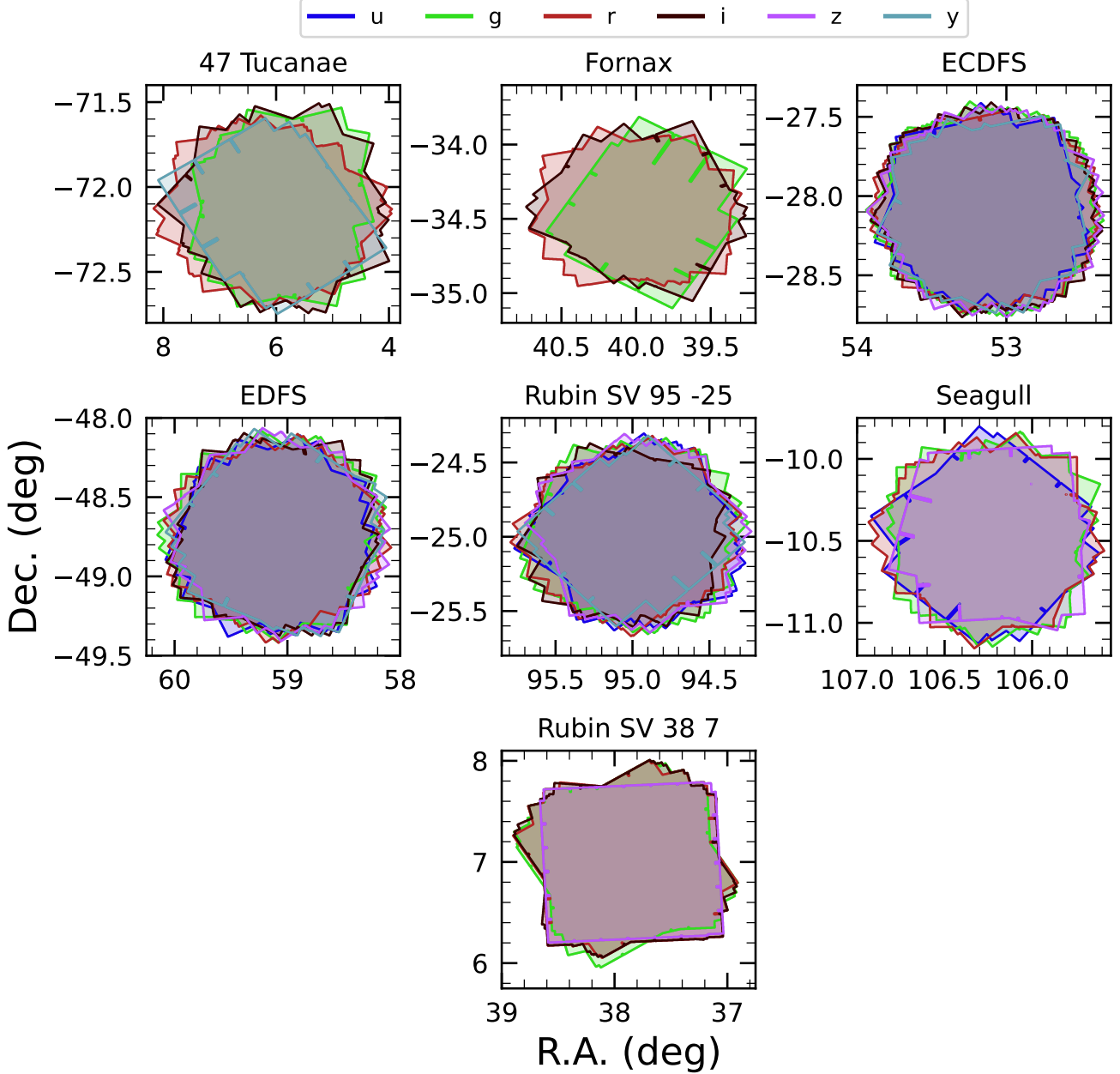


Figure 6. Sky coverage maps showing the distribution of visits in each field, color coded by band. The images clearly show the focal plane chip gaps and dithering pattern. Only the detectors for which single frame processing succeeded are included in the plots, which explains why the central region of 47_Tuc looks thinner than the other fields.

available at <https://sdm-schemas.lsst.io>.⁸⁵ The DP1 science data products are derived from the 15972 individual CCD images taken across 1792 exposures in the seven LSSTComCam commissioning fields (§2.4). To aid legibility, we have separated the descriptions of the

data products from the description of the data release processing pipeline, a summary of which is provided in §4, with a full description provided in Rubin Observatory Science Pipelines Developers (2025). Similarly, because most of the data products described here can be accessed via either the International Virtual Observatory Alliance (IVOA) Services (§6.2.1) or the Data Butler (§6.2.2), we describe them in a manner that is agnostic to the means of access.

⁸⁵ Searchable catalog schemas are also available to Data Rights Holders via the Rubin Science Platform at <https://data.lsst.cloud>.

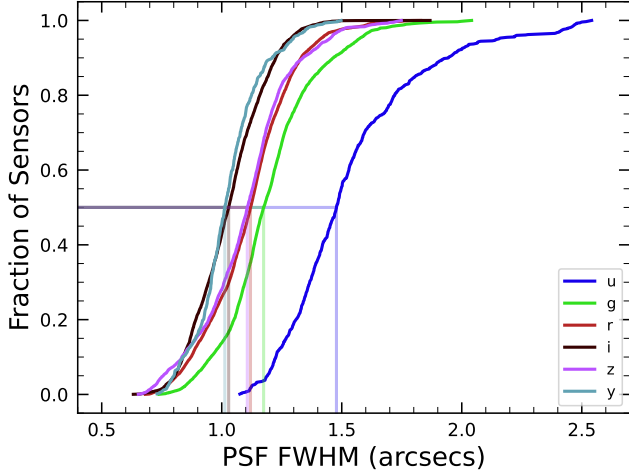


Figure 7. Cumulative distribution of PSF FWHM (arcsec) over all 16071 visits images in the DP1 dataset for each filter. The vertical dashed lines represent the median PSF FWHM at 1.46, 1.36, 1.24, 1.18 and 1.20 arcsec for the *ugrizy* wavebands, respectively.

The data products that comprise DP1 provide an early preview of future LSST data releases and are strongly dependent on the type and quality of the data that was collected during LSSTComCam on-sky campaign (§2.4). Consequently not all anticipated LSST data products, as described in the Data Product Definition Document (DPDD) (M. Jurić et al. 2023) were produced for the DP1 dataset.

Rubin Observatory has adopted the convention by which single-epoch detections are referred to as Sources. By contrast, the astrophysical object associated with a given detection is referred to as an Object⁸⁶. As such, a given Object will likely have multiple associated Sources, since it will be observed in multiple epochs.

At the highest level, the DP1 data products fall into one of five types:

- **Images**, including single-epoch images, deep and template coadded images, and difference images (§3.1);
- **Catalogs** of astrophysical Sources and Objects detected and measured in the aforementioned images. We also provide the astrometric and photometric reference catalog generated from external sources that was used during processing to generate the DP1 data products (§3.2);

⁸⁶ We caution that this nomenclature is not universal; for example, some surveys call “detections” what we call “sources”, and use the term “sources” for what we call “objects”.

- **Maps**, which provide non-science-level visualizations of the data within the release. They include, for example, zoomable multi-band images and coverage maps (§3.3);
- **Ancillary data products**, including, for example, the parameters used to configure the data processing pipelines, log and processing performance files, and calibration data products (§3.6);
- **Metadata** in the form of tables containing information about each visit and processed image, such as pointing, exposure time, and a range of image quality summary statistics (§3.5).

While images and catalogs are expected to be the primary data products for scientific research, we also recognize the value of providing access to other data types to support investigations and ensure transparency.

To facilitate processing, Rubin DP1 uses a single skymap⁸⁷ that covers the entire sky area encompassing the seven DP1 fields. The DP1 skymap divides the entire celestial sphere into 18938 tracts, each covering approximately 2.8 deg^2 . The tracts are arranged in rings of declination, ordered from south to north, then with increasing right ascension within a ring. Each tract is further subdivided into 10×10 equally-sized patches. Both tracts and patches overlap with their neighboring regions. The amount of overlap between tracts changes with declination, with tracts nearest the poles having the greatest degree of overlap; the minimum overlap between tracts is $1.0'$. By contrast, the amount of overlap between patches is constant, with each patch overlapping each of its neighbouring patches by $80.0'$. As a consequence, each patch covers 0.036 deg^2 , which is slightly larger than the tract area divided by the number of patches in a tract. The aerial coverage of a patch is comparable to, but somewhat smaller than, the 0.058 deg^2 field-of-view of a single LSSTComCam or LSSTCam detector, meaning each detector image spans multiple patches. The size of a tract is larger than the LSSTComCam field of view; however, since each observed field extends across more than one tract, each field covers multiple tracts.

The skymap is integral to the production of co-added images. To create a coadded image, the processing pipeline selects all calibrated science images in a given field that meet specific quality thresholds (§3.1 and

⁸⁷ A skymap is a tiling of the celestial sphere, organizing large-scale sky coverage into manageable sections for processing and analysis. While the skymap described here is specific to DP1, we do not anticipate major changes to the skymap in future data releases.

730 §4.5.1) for a given `patch`, warps them onto a single
 731 consistent pixel grid for that `patch`, as defined by the
 732 `skymap`, then coadds them. Each individual coadd im-
 733 age therefore covers a single `patch`.

734 Throughout this section, the data product names are
 735 indicated using monospace font. Data products are ac-
 736 cessed via either the [IVOA](#) Services (§6.2.1) or the Data
 737 Butler (§6.2.2).

738 3.1. *Science Images*

739 Science images are exposures of the night sky, as dis-
 740 tinct from `calibration` images (§3.6.2). Although the re-
 741 lease includes `calibration` images, allowing users to re-
 742 process the raw images if needed, this is expected to be
 743 necessary only in rare cases. Users are strongly encour-
 744 aged to start from the `visit_image` provided. The data
 745 product names shown here are those used by the Data
 746 Butler, but the names used in the [IVOA](#) Services differ
 747 only slightly in that they are prepended by “lsst.”.

- 748 • `raw` images ([NSF-DOE Vera C. Rubin Observatory 2025b](#)) are unprocessed data received directly
 749 from the camera. Each `raw` corresponds to a single `CCD` from a single [LSSTComCam](#) exposure of
 750 30 s duration. Each [LSSTComCam](#) exposure typ-
 751 ically produces up to nine `raws`, one per sensor in
 752 the focal plane. However, a small number of expo-
 753 sures resulted in fewer than nine `raw` images due
 754 to temporary hardware issues or readout faults.

755 In total, [DP1](#) includes 16125 `raw` images. [Ta-](#)
 756 [ble 3](#) provides a summary by target and band. A
 757 `raw` contains 4608×4096 pixels, including pres-
 758 can and overscan, and occupies around 18 MB of
 759 disk space.⁸⁸ The field of view of a single `raw`, ex-
 760 cluding prescan and overscan regions, is roughly
 761 $0^\circ.23 \times 0^\circ.22 \approx 0.051 \text{ deg}^2$, corresponding to a plate
 762 scale of $0''.2$ per pixel.

- 763 • `visit_images` ([NSF-DOE Vera C. Rubin Observatory 2025c](#)) are fully-calibrated processed im-
 764 ages. They have undergone instrument signature
 765 removal (§4.2.1) and all the single frame process-
 766 ing steps described in §4.2 which are, in summary:
 767 `PSF` modeling, `background` subtraction, and ast-
 768 rometric and photometric `calibration`. As with
 769 `raws`, a `visit_image` contains processed data from
 770 a single `CCD` resulting from a single 30 s [LSST-](#)
 771 [ComCam](#) exposure. As a consequence, a single

772 **Table 3.** Number of `raw` images per field and band. Each raw
 773 image corresponds to a single 30-second [LSSTComCam](#) expo-
 774 sure on one `CCD`. Most exposures produce nine raw images, one
 775 per sensor in the focal plane, however some yield fewer due to
 776 occasional hardware or readout issues.

Field Code	Band						Total
	<i>u</i>	<i>g</i>	<i>r</i>	<i>i</i>	<i>z</i>	<i>y</i>	
47_Tuc	54	90	288	171	0	45	648
ECDFS	387	2070	2133	1455	1377	270	7692
EDFS_comcam	180	549	783	378	378	180	2448
Fornax_dSph	0	45	225	108	0	0	378
Rubin_SV_095_-25	297	738	756	207	540	90	2628
Rubin_SV_38_7	0	396	360	495	180	0	1431
Seagull	90	333	387	0	90	0	900
Total	1008	4221	4932	2814	2565	585	16125

777 [LSSTComCam](#) exposure typically results in nine
 778 `visit_images`. The handful of exposures with
 779 fewer than nine `raw` images also have fewer than
 780 nine `visit_images`, but there are an additional
 781 153 `raw` that failed processing and for which there
 782 is thus no corresponding `visit_image`. The ma-
 783 jority of failures – 131 in total – were due to chal-
 784 lenges with astrometric fits or `PSF` models in the
 785 47_Tuc crowded field. The other failures were in
 786 the Rubin_SV_095_-25 (9 failures), ECDFS (8),
 787 Fornax_dSph (3), and EDFS_comcam (2) fields.

788 In total, there are 15972 `visit_images` in [DP1](#).
 789 Each `visit_image` comprises three images: a cal-
 790 ibrated science image, a variance image, and a
 791 pixel-level bitmask that flags issues such as sat-
 792 uration, cosmic rays, or other artifacts. Each
 793 `visit_image` also contains a position-dependent
 794 `PSF` model, [World Coordinate System \(WCS\)](#) in-
 795 formation, and various `metadata` providing infor-
 796 mation about the observation and processing. The
 797 science and variance images and the pixel mask
 798 each contain 4072×4000 pixels. In total, a single
 799 `visit_image`, including all extensions and `meta-`
 800 `data`, occupies around 110 MB of disk space. A
 801 plot showing the normalized cumulative histogram
 802 of the 5σ depths of all the `visit_images` in [DP1](#)
 803 is shown in [Figure 8](#).

- 804 • `deep_coadds` ([NSF-DOE Vera C. Rubin Observatory 2025d](#)) are the product of warping and co-
 805 adding multiple `visit_images` covering a given
 806 `patch`, as defined by the `skymap`. `deep_coadds`
 807 are created on a per-band basis, meaning only

88 Each amplifier image contains 3 and 64 columns of serial prescan and overscan pixels, respectively, and 48 rows of parallel overscan pixels, meaning a `raw` contains 4072×4000 exposed pixels.

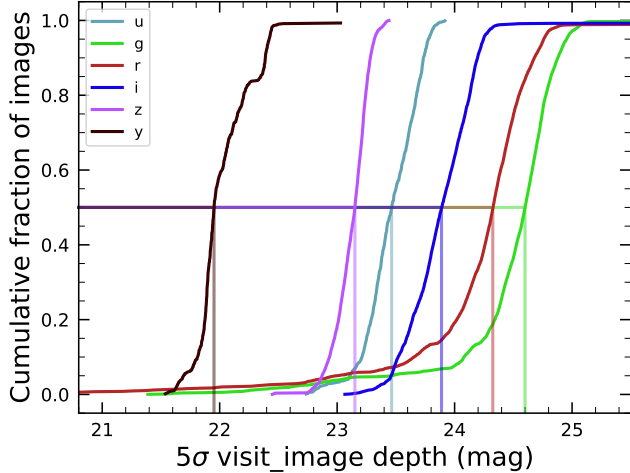


Figure 8. Normalized cumulative histograms of the 5σ depths of all `visit_images` in each band. The vertical lines indicate the 50th percentiles for each band (see legend).

data from exposures taken with a common filter are coadded. As such, there are up to six `deep_coadds` covering each `patch` – one for each of the six LSSTComCam bands. The process of producing `deep_coadds` is described in detail in §4.5 but, to summarize, it involves the selection of suitable `visit_images` (both in terms of `patch` coverage, band, and image quality), the warping of those `visit_images` onto a common pixel grid, and the co-adding of the warped `visit_images`. To be included in a `DP1` `deep_coadd`, a `visit_image` needed to have a `PSF FWHM` smaller than $1.7''$. Of the 15972 `visit_images`, 15375 satisfied this criterion and were therefore used to create `deep_coadds`.

There are a total of 2644 `deep_coadds` in `DP1`. As mentioned above, a single `deep_coadd` covers one `patch`, and includes a small amount of overlap with its neighboring `patch`. The skymap used for `DP1` defines a `patch` as having an on-sky area of 0.028 deg^2 excluding overlap, and 0.036 deg^2 including overlap. A single `deep_coadd` – including overlap – contains 3400×3400 equal-sized pixels, corresponding to a platescale of $0.2''$ per pixel. Each `deep_coadd` contains the science image (i.e., the coadd), a variance image, and a pixel mask; all three contain the same number of pixels. Each `deep_coadd` also contains a position-dependent `PSF` model (which is the weighted sum of the `PSF` models of the input `visit_images`), `WCS` information, plus various `metadata`.

The number of `visit_images` that contributed to a given `deep_coadd` varies across the patch; the

Survey Property Maps can be consulted to gain insights into the total exposure time at all locations covered by the survey. Similarly, since coadds always cover an entire `patch`, it is common for a `deep_coadd` to contain regions that were not covered by any of the selected `visit_images`, particularly if the `patch` is on the outskirts of a field and was thus not fully observed. By the nature of how coadds are produced, such regions may contain seemingly valid `flux` values (i.e., not necessarily zeros or `NaNs`), but will instead be flagged with the `NO_DATA` flag in the pixel mask. It is therefore crucial that the pixel mask be referred to when analyzing `deep_coadds`.

- `template_coadds` (NSF-DOE Vera C. Rubin Observatory 2025e) are those created to use as templates for difference imaging, i.e., the process of subtracting a template image from a `visit_image` to identify either variable or `transient` objects. It should be noted, however, that `template_coadds` are not themselves subtracted from `visit_images` but are, instead, warped to match the `WCS` of a `visit_image`. It is this warped template that is subtracted from the `visit_image` to create a difference image.⁸⁹ As with `deep_coadds`, `template_coadds` are produced by warping and co-adding multiple `visit_images` covering a given skymap-defined `patch`. The process of building `template_coadds` is the same as that for `deep_coadds`, but the selection criteria differ between the two types of coadd. In the case of `template_coadds`, one third of `visit_images` covering the `patch` in question with the narrowest `PSF FWHM` are selected. If one third corresponds to fewer than twelve `visit_images` (i.e., there are fewer than 36 `visit_images` covering the `patch`), then the twelve `visit_images` with the narrowest `PSF FWHM` are selected. Finally, if there are fewer than twelve `visit_images` covering the `patch`, then all `visit_images` are selected. Of the 15972 `visit_images`, 13113 were used to create `template_coadds`. This selection strategy is designed to optimize for `seeing` when a `patch` is well-covered by `visit_images`, yet still enable the production of `template_coadds` for poorly-covered patches. As with `deep_coadds`, the num-

⁸⁹ For storage space reasons, warped templates are not retained for `DP1`, as they can be readily and reliably recreated from the `template_coadds`.

887 ber of `visit_images` that contributed to a `tem-`
 888 `plate_coadd` varies across the patch.

889 DP1 contains a total of 2730 `template_coadds`.⁹⁰
 890 As with `deep_coadds`, a single `template_coadd`
 891 covers a single `patch`. Since the same `skymap` is
 892 used when creating both `deep_coadd` and `tem-`
 893 `plate_coadds`, the on-sky area and pixel count of
 894 `template_coadds` are the same as that of a `deep_`
 895 `coadd` (see above). Similarly, `template_coadds`
 896 contain the science image (i.e., the coadd), a vari-
 897 ance image, and a pixel mask; all three contain the
 898 same number of pixels. Also included are the `PSF`
 899 model, `WCS` information, and `metadata`. As is
 900 the case for `deep_coadd`, those pixels within `tem-`
 901 `plate_coadds` that are not covered by any of the
 902 selected `visit_images` may still have seemingly
 903 valid values, but are indicated with the `NO_DATA`
 904 flag within the pixel mask.

- 905 • `difference_images` (NSF-DOE Vera C. Rubin
 906 Observatory 2025f) are generated by the subtrac-
 907 tion of the warped, scaled, and `PSF`-matched `tem-`
 908 `plate_coadd` from the `visit_image` (see §4.6.1).
 909 In principle, only those sources whose `flux` has
 910 changed relative to the `template_coadd` should be
 911 apparent (at a significant level) within a `difference_`
 912 `image`. In practice, however, there are nu-
 913 merous spurious sources present in `difference_`
 914 `images` due to unavoidably imperfect template
 915 matching.

916 In total, there are 15972 `difference_images` in
 917 DP1, one for each `visit_image`.

918 Like `visit_images`, `difference_images` contain
 919 the science (i.e., difference) image, a variance im-
 920 age, and a pixel mask; all three contain the same
 921 number of pixels, which is the same as that of
 922 the input `visit_image`. Also included is the `PSF`
 923 model, `WCS` information, and `metadata`.

- 924 • Background images contain the model `background`
 925 that has been generated and removed from a
 926 science image. `visit_images`, `deep_coadds` and
 927 `template_coadds` all have associated `background`
 928 images.⁹¹ Background images contain the same
 929 number of pixels as their respective science im-
 930 age, and there is one `background` image for each

⁹⁰ The difference in the number of `deep_coadds` and `template_coadds` is due to the difference in the `visit_image` selection criteria for each coadd.

⁹¹ In future data releases, `background` images may be included as part of their respective science image data product.

931 `visit_image`, `deep_coadd`, and `template_coadd`.
 932 Difference imaging analysis also measures and sub-
 933 tracts a `background` model, but the `difference_`
 934 `background` data product is not written out by
 935 default and is not part of DP1.

936 Background images are not available via the IVOA
 937 Service; they can only be accessed via the Butler
 938 Data Service.

939 3.2. Catalogs

940 Here we describe science-ready tables produced by the
 941 science pipelines. All but one of the catalogs described
 942 here contain data for detections in the images described
 943 in section 3.1, the exception being the `Calibration` cat-
 944 alog, which contains reference data obtained from previ-
 945 ous surveys. Observatory-produced `metadata` tables are
 946 described in §3.5. Each type of catalog contains mea-
 947 surements for either Sources detected in `visit_images`
 948 and `difference_images`, or Objects detected in `deep_`
 949 `coadds`.

950 While the `Source`, `Object`, `ForcedSource`, `Dia-`
 951 `Source`, `DiaObject`, and `ForcedSourceOnDiaObject`
 952 catalogs described below each differ in terms of their
 953 specific columns, in general they each contain: one or
 954 more unique identification numbers, positional informa-
 955 tion, one or more types of `flux` measurements (e.g., aper-
 956 ture fluxes, `PSF` fluxes, Gaussian fluxes, etc.), and a se-
 957 ries of boolean flags (indicating, for example, whether
 958 the source/object is affected by saturated pixels, cosmic
 959 rays, etc.) for each source/object. The Solar System
 960 catalogs `SSObject` and `SSSource` deviate from this gen-
 961 eral structure in that they instead contain orbital pa-
 962 rameters for all known asteroids. Where applicable, all
 963 measured properties are reported with their associated
 964 1σ uncertainties.

965 Since DP1 is a preview, it doesn't include all the cat-
 966 alogs expected in a full LSST Data Release. Additionally,
 967 the catalogs it does include may be missing some
 968 columns planned for future releases. Where this is the
 969 case, we note what data are missing in the catalog de-
 970 scriptions that follow.

971 Catalog data are stored in the `Qserv` database (§6.5.1)
 972 and are accessible via Table Access Protocol (IVOA
 973 standard) (IVOA), and an online DP1 catalog schema
 974 is available at <https://sdm-schemas.lsst.io/dp1.html>. Catalog data are also accessible via the Data Butler
 975 (§6.2.2).

- 977 • The `Source` catalog (NSF-DOE Vera C. Rubin
 978 Observatory 2025g) contains data on all sources
 979 which are, prior to deblending (§4.5.2), detected
 980 with a greater than 5σ significance in each individ-
 981 ual visit. The detections reported in the `Source`

catalog have undergone deblending; in the case of blended detections, only the deblended sources are included in the **Source** catalog. It is important to note that while the criterion for inclusion in a **Source** catalog is a $> 5\sigma$ detection in a **visit_image** prior to deblending, the positions and fluxes are reported post-deblending. Hence, it is possible for the **Source** catalog to contain sources whose **flux-to-error** ratios — potentially of all types (i.e., aperture **flux**, **PSF flux**, etc.) — are less than 5.

In addition to the general information mentioned above (i.e., IDs, positions, fluxes, flags), the **Source** catalog also includes basic **shape** and extendedness information.

The **Source** catalog contains data for 46 million **sources** in **DP1**.

A cumulative histogram showing the PSF magnitudes of all **sources** contained within the **Source** catalogue is presented in the top panel of Figure 9

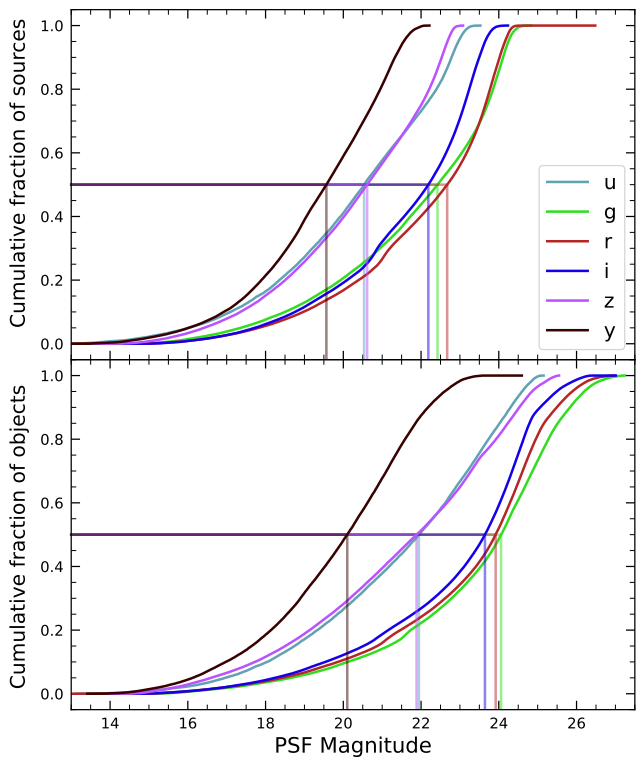


Figure 9. Normalized cumulative histograms of the PSF magnitudes of all $> 5\sigma$ -detected **sources** (top panel) and **objects** (bottom panel) contained in the **Source** and **Object** catalogs, respectively, separated according to band (see legend). The vertical lines indicate the 50th percentile for each band.

- The **Object** catalog (NSF-DOE Vera C. Rubin Observatory 2025h) contains data on all objects detected with a greater than 5σ significance in the **deep_coadds**. With coadd images produced on a per-band basis, a $> 5\sigma$ detection in one or more of the bands will result in an object being included in the **Object** catalog. For cases where an object is detected at $> 5\sigma$ in more than one band, a cross-matching has been performed between bands to associate an object in one band with its counterpart(s) in the other bands. As such, unlike the **Source** catalog, the **Object** catalog contains data from multiple bands. The objects reported in the **Object** catalog have also undergone deblending; in the case of blended detections, only the deblended child objects are included in the catalog. As with the **Source** catalog, the criterion for inclusion in the **Object** catalog is a $> 5\sigma$ detection in one of the **deep_coadds** prior to deblending, yet the positions and fluxes of objects are reported post-deblending. Hence, it is possible for **Object** catalog to contain **objects** whose **flux-to-error** ratios — potentially of all types and in all bands — are less than 5.

In addition to the general information mentioned above (i.e., IDs, positions, fluxes, flags), the **Object** catalog also includes basic **shape** and extendedness information. While they may be included in future data releases, no photometric redshifts, Petrosian magnitudes (V. Petrosian 1976), proper motions or periodicity information are included in the **DP1** object catalogs.

The **Object** catalog contains data for 2.3 million objects in **DP1**.

- The **ForcedSource** catalog (NSF-DOE Vera C. Rubin Observatory 2025i) contains forced PSF photometry measurements performed on both **difference_images** (i.e., the **psfDiffFlux** column) and **visit_images** (i.e., the **psfFlux** column) at the positions of all the objects in the **Object** catalog, to allow assessment of the time variability of the fluxes. We recommend using the **psfDiffFlux** column when generating light curves because this quantity is less sensitive to **flux** from neighboring sources than **psfFlux**. In addition to forced photometry PSF fluxes, a number of boolean flags are also included in the **Forced-Source** catalog.

The **ForcedSource** catalog contains a total of 269 million entries across 2.3 million unique objects.

- The **DiaSource** catalogs (NSF-DOE Vera C. Rubin Observatory 2025j) contains data on all the sources detected at a $> 5\sigma$ significance — including those associated with known Solar System objects — in the **difference_images**. Unlike sources detected in **visit_images**, sources detected in difference images (hereafter, “DiaSources”) have gone through an association step in which an attempt has been made to associate them into underlying objects called “DiaObject”s. The **DiaSource** catalog consolidates all this information across multiple visits and bands. The detections reported in the **DiaSource** catalog have not undergone deblending. 1100
1101
1102
1103
1104
1105
1106
1107
1108
1109
1110
1111
1112
1113
1114
- The **DiaObject** catalog (NSF-DOE Vera C. Rubin Observatory 2025k) contains the astrophysical objects that DiaSources are associated with (i.e., the “DiaObjects”). The **DiaObject** catalog contains only non-Solar System Objects; Solar System Objects are, instead, recorded in the **SSObject** catalog. When a DiaSource is identified, the **DiaObject** and **SSObject** catalogs are searched for objects to associate it with. If no association is found, a new **DiaObject** is created and the **DiaSource** is associated to it. Along similar lines, an attempt has been made to associate **DiaObjects** across multiple bands, meaning the **DiaObject** catalog, like the **Object** catalog, contains data from multiple bands. Since **DiaObjects** are typically **transient** or variable (by the nature of their means of detection), the **DiaObject** catalog contains summary statistics of their fluxes, such as the mean and standard deviation over multiple epochs; users must refer to the **ForcedSourceOnDiaObject** catalog (see below) or the **DiaSource** catalog for single **epoch flux** measurements of **DiaObjects**. 1115
1116
1117
1118
1119
1120
1121
1122
1123
1124
1125
1126
1127
1128
1129
1130
1131
1132
1133
1134
1135
1136
1137
1138
1139
1140
- The **SSObject** catalog (NSF-DOE Vera C. Rubin Observatory 2025m), Minor Planet Center Orbit database (MPCORB) and **SSObject**, carry information about solar system objects. The **MPCORB** table provides the Minor Planet Center-computed orbital elements for all known asteroids, including those that Rubin discovered. For DP1, the **SSObject** catalog serves primarily to provide the mapping between the International Astronomical Union (IAU) designation of an object (listed in MPCORB), and the internal **ssObject** identifier, which is used as a key to find solar system object observations in the **DiaSource** and **SSSource** tables. The **SSObject** catalog contains data for 431 **SSObjects** in **DP1**. 1141
1142
1143
1144
1145
1146
1147
1148
1149
- The **SSSource** catalog (NSF-DOE Vera C. Rubin Observatory 2025n) contains data on all DiaSources that are either associated with previously-known Solar System Objects, or have been confirmed as newly-discovered Solar System Objects by confirmation of their orbital properties. As entries in the **SSSource** catalog stem from the **DiaSource** catalog, they have all been detected at $> 5\sigma$ significance in at least one band. The **SSSource** catalog contains data for 5988 Solar System Sources. 1150
1151
1152
1153
1154
1155
1156
1157
1158
1159
1160
1161
1162
1163
1164
1165
1166
1167
1168
1169
1170
1171
1172
1173
1174
1175
1176
1177
1178
1179
1180
1181
1182
1183
1184
1185
1186
1187
1188
1189
1190
1191
1192
1193
1194
1195
1196
1197
1198
1199
- The **CcdVisit** catalog (NSF-DOE Vera C. Rubin Observatory 2025o) contains data for each individual processed **visit_image**. In addition to technical information, such as the on-sky coordinates of the central pixel and measured pixel scale, the **CcdVisit** catalog contains a range of data quality measurements, such as whole-image summary statistics for the **PSF** size, zeropoint, sky **background**, sky noise, and quality of astrometric solution. It provides an efficient method to access **visit_image** properties without needing to access the image data. When combined with the data contained in the **Visit** table described in §??, it provides a full picture of the telescope pointing and sky conditions at the time of observation. 1190
1191
1192
1193
1194
1195
1196
1197
1198
1199

The **CcdVisit** catalog contains entries summarizing data for all 16071 **visit_images**.

- The **Calibration** catalog is the reference catalog that was used to perform astrometric and photometric **calibration**. It is a whole-sky catalog built specifically for **LSST**, as no single prior reference catalog had both the depth and coverage needed to calibrate **LSST** data. It combines data from multiple previous reference catalogs and contains 1190
1191
1192
1193
1194
1195
1196
1197
1198
1199

only stellar sources. Full details on how the **Calibration** catalog was built are provided in [P. S. Ferguson et al. \(2025\)](#)⁹². We provide a brief summary here.

For the *grizy* bands, the input catalogs were (in order of decreasing priority): **Dark Energy Survey (DES)** Y6 Calibration Stars ([E. S. Rykoff et al. 2023](#)); **Gaia-B or R Photometry (Gaia) (XP)** Synthetic Magnitudes ([Gaia Collaboration et al. 2023a](#)); the **Panoramic Survey Telescope and Rapid Response System (Pan-STARRS)1 3PI Survey** ([K. C. Chambers et al. 2016](#)); **Data Release 2** of the **SkyMapper** survey ([C. A. Onken et al. 2019](#)); and **Data Release 4** of the **VLT Survey Telescope (VST) Asteroid Terrestrial-impact Last Alert System (ATLAS)** survey ([T. Shanks et al. 2015](#)). For the *u*-band, the input catalogs were (in order of decreasing priority): **Standard Stars from Sloan Digital Sky Survey (SDSS) Data Release 16** ([R. Ahumada et al. 2020](#)); **Gaia-XP Synthetic Magnitudes** ([Gaia Collaboration et al. 2023a](#)); and synthetic magnitudes generated using **Single Lens Reflex (SLR)**, which estimates the *u*-band **flux** from the *g*-band **flux** and *g-r* colors. This **SLR** estimates were used to boost the number of *u*-band reference sources, as otherwise the source density from the *u*-band input catalogs is too low to be useful for the **LSST**.

Only stellar sources were selected from each input catalog. Throughout, the **Calibration** catalog uses the **DES** bandpasses for the *grizy* bands and the **SDSS** bandpass for the *u*-band; color transformations derived from high quality sources were used to convert fluxes from the various input catalogs (some of which did not use the **DES/SDSS** bandpasses) to the respective bandpasses. All sources from the input catalogs are matched to **Gaia-Data Release 3 (DR3)** sources for robust astrometric information, selecting only isolated sources (i.e., no neighbors within 1").

After collating the input catalogs and transforming the fluxes to the standard DES/SDSS bandpasses, the catalog was used to identify sources within a specific region of the sky. This process generated a set of standard columns containing positional and flux information, along with their associated uncertainties.

⁹² In [P. S. Ferguson et al. \(2025\)](#), the calibration reference catalog is referred to as “The Monster”. This terminology is also carried over to the DP1 Butler.

3.2.1. *Source and Object Designations*

To refer to individual sources or objects from the DP1 catalogs, one should follow the LSST DP1 naming convention that has been registered with the International Astronomical Union. Because the **Source**, **Object**, **DiaSource**, **DiaObject**, and **SSObject** tables each have their own unique IDs, their designations should differ. In general, source designations should begin with the string “LSST-DP1” (denoting the Legacy Survey of Space and Time, Data Preview 1), followed by a string specifying the table from which the source was obtained. These strings should be “O” (for the **Object** table), “S” (**Source**), “DO” (**DiaObject**), “DS” (**DiaSource**), or “SSO” (**SSObject**). Following the table identifier, the designation should contain the full unique numeric identifier from the specified table (i.e., the **objectId**, **sourceId**, **diaObjectId**, **diaSourceId**, or **ssObjectId**). Each component of the identifier should be separated by dashes, resulting in a designation such as “LSST-DP1-TAB-123456789012345678”. In summary, source designations should adhere to the formats listed below:

- **Object:** LSST-DP1-O-609788942606161356 (for **objectId** 609788942606161356)
- **Source:** LSST-DP1-S-600408134082103129 (for **sourceId** 600408134082103129)
- **DiaObject:** LSST-DP1-DO-609788942606140532 (for **diaObjectId** 609788942606140532)
- **DiaSource:** LSST-DP1-DS-600359758253260853 (for **diaSourceId** 600359758253260853)
- **SSObject:** LSST-DP1-SSO-21163611375481943 (for **ssObjectId** 21163611375481943)

Tables that were not explicitly mentioned in the description above do not have their own unique IDs, but are instead linked to one of the five tables listed above via a unique ID. For example, the **ForcedSource** table is keyed on **objectId**, **ForcedSourceOnDiaObject** uses **diaObjectId**, **SSSource** is linked to **diaSourceId** and **ssObjectId**, and **MPCORB** uses **ssObjectId**.

3.3. *Survey Property Maps*

Maps are two-dimensional visualizations of survey data. In **DP1**, these fall into two categories: **Survey Property Maps** and **Hierarchical Progressive Survey (HiPS) Maps** ([P. Fernique et al. 2015](#)). **Survey Property Maps** ([NSF-DOE Vera C. Rubin Observatory 2025p](#)) summarize how properties such as observing conditions or exposure time vary across the observed sky.

1244 Each map provides the spatial distribution of a spe-
 1245 cific quantity at a defined sky position for each band
 1246 by aggregating information from the images used to
 1247 make the `deep_coadd`. Maps are initially created per-
 1248 `tract` and then combined to produce a final consolidated
 1249 map. At each sky location, represented by a spatial pixel
 1250 in the **Hierarchical Equal-Area iso-Latitude Pixelisation**
 1251 (**HEALPix**) (K. M. Górski et al. 2005) grid, values are
 1252 derived using statistical operations, such as minimum,
 1253 maximum, mean, weighted mean, or sum, depending on
 1254 the property.

1255 DP1 contains 14 survey property maps. The avail-
 1256 able maps describe total exposure times, observation
 1257 epochs, **PSF** size and `shape`, **PSF** magnitude limits,
 1258 sky `background` and noise levels, as well as astro-
 1259 metric shifts and **PSF** distortions due to wavelength-
 1260 dependent atmospheric **Differential Chromatic Refrac-
 1261 tion (DCR)** effects. They all use the dataset type
 1262 format `deep_coadd_<PROPERTY>_consolidated_map_-`
 1263 `<STATISTIC>`. For example, `deep_coadd_exposure_-`
 1264 `time_consolidated_map_sum` provides a spatial map of
 1265 the total exposure time accumulated per sky position in
 1266 units of seconds. All maps are stored in `HealSparse`⁹³
 1267 format. Survey property maps are only available via
 1268 the Data Butler (§6.2.2) and have dimensions `band` and
 1269 `skymap`.

1270 Figure 10 presents three survey property maps for ex-
 1271 posure time, **PSF** magnitude limit, and sky noise, com-
 1272 puted for representative tracts and bands. Because full
 1273 consolidated maps cover widely separated tracts, we use
 1274 clipped per-`tract` views here to make the spatial patterns
 1275 more discernible. Many more survey property maps are
 1276 available in the DP1 repository.

1278 3.4. *HiPS Maps*

1279 **HiPS Maps** (P. Fernique et al. 2015), offer an inter-
 1280 active way to explore seamless, multi-band tiles of the
 1281 sky regions covered by DP1, allowing for smooth panning
 1282 and zooming. DP1 provides multi-band **HiPS** im-
 1283 ages created by combining data from individual bands
 1284 of `deep_coadd` and `template_coadd` images, using an
 1285 improved version (Lust et al. in prep) of the algorithm
 1286 presented in R. Lupton et al. (2004). These images are
 1287 false-color representations generated using various filter
 1288 combinations for the red, green, and blue channels.

1289 The available filter combinations include *gri*, *izy*, *riz*,
 1290 and *ugr* for both `deep_coadd` and `template_coadd`. Ad-
 1291 ditionally, for `deep_coadd` only, we provide color blends

1292 such as *uug* and *grz*. Post-DP1, we plan to also provide
 1293 single-band HiPS images for all *ugrizy* bands in both
 1294 **Portable Network Graphics (PNG)** and **Flexible Image**
 1295 **Transport System (FITS)** formats.

1296 HiPS maps are only accessible through the **HiPS**
 1297 viewer in the **Rubin Science Platform (RSP)** Portal
 1298 (§6.3) and cannot be accessed via the Data Butler
 1299 (§6.2.2). All multi-band **HiPS** images are provided in
 1300 **PNG** format.

1301 3.5. *Metadata*

1302 DP1 also includes `metadata` about the observations,
 1303 which are stored in the `Visit` table. We distinguish it
 1304 from a catalog as the data it contains was produced
 1305 by the observatory directly, rather than the science
 1306 pipelines. The `Visit` table contains technical data for
 1307 each visit, such as telescope pointing, camera rotation,
 1308 `airmass`, exposure start and end time, and total expo-
 1309 sure time. Some of the information contained within
 1310 the `Visit` table is also contained in the `CCDVisit` cat-
 1311 alogue described in §3.2 (e.g., exposure time), although
 1312 the latter also includes information produced by the pro-
 1313 cessing pipelines at a per-detector level, such as the **PSF**
 1314 size and limiting magnitudes.

1315 3.6. *Ancillary Data Products*

1316 DP1 also includes several ancillary data products.
 1317 While we do not expect most users to need these, we
 1318 describe them here for completeness. All the Data Pro-
 1319 ducts described in this section can only be accessed via
 1320 the Data Butler (§6.2.2).

1321 3.6.1. *Task configuration, log, and metadata*

1322 DP1 includes `provenance`-related data products such
 1323 as task logs, `configuration` files, and task metadata.
 1324 Configuration files record the parameters used in each
 1325 processing task, while logs and `metadata` contain infor-
 1326 mation output during processing. These products help
 1327 users understand the processing setup and investigate
 1328 potential processing failures.

1329 3.6.2. *Calibration Data Products*

1330 Calibration data products include a variety of images
 1331 and models that are used to characterize and correct
 1332 the performance of the camera and other system com-
 1333 ponents. These include bias, dark, and flat-field images,
 1334 **Photon Transfer Curve (PTC)** gains, brighter-fatter ker-
 1335 nels (P. Antilogus et al. 2014), charge transfer ineffi-
 1336 ciency (**CTI**) models, linearizers, and illumination cor-
 1337 rections. For flat-field corrections, DP1 processing used
 1338 combined flats, which are averaged from multiple indi-
 1339 vidual flat-field exposures to provide a stable `calibra-
 1340 tion`. These `calibration` products are essential inputs

⁹³ A sparse **HEALPix** representation that efficiently encodes data values on the celestial sphere. <https://healsparse.readthedocs.io>

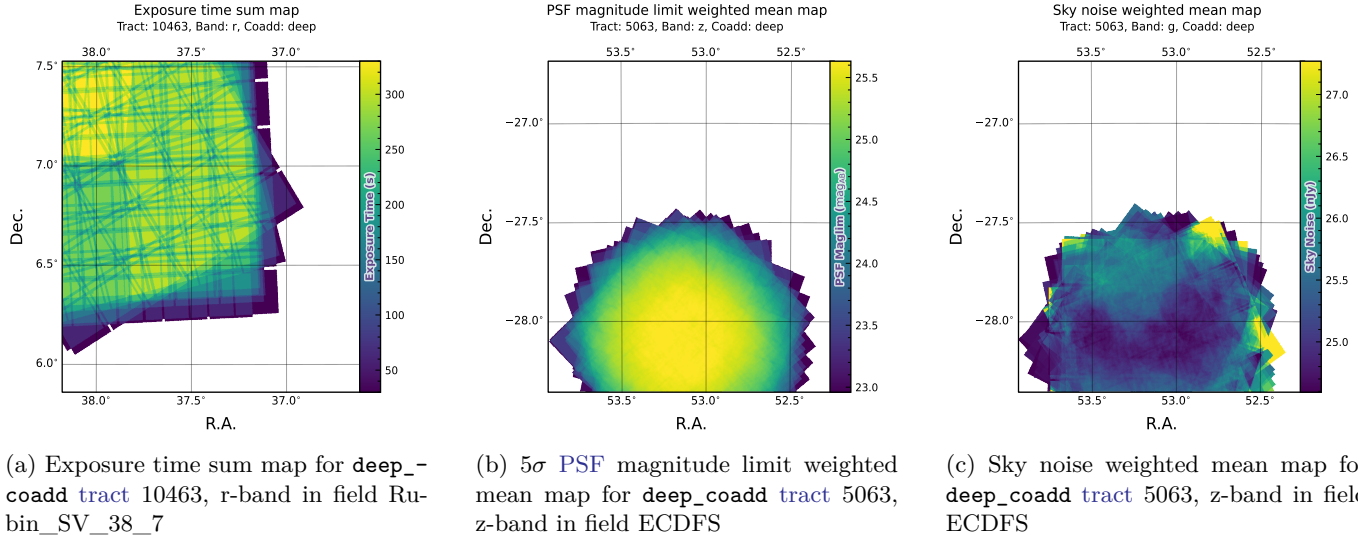


Figure 10. Examples of survey property maps from Rubin DP1 across different bands, clipped to the boundary of a single tract for visual clarity.

to [Instrument Signal Removal \(ISR\)](#) (§4.2.1). While these products are included in DP1 for transparency and completeness, users should not need to rerun ISR for their science and are advised to start with the processed `visit_image`.

by the Rubin scientific community. Version v29.1 of the pipelines was used to produce DP1⁹⁵.

4. DATA RELEASE PROCESSING

[Data Release Processing \(DRP\)](#) is the systematic processing of all Rubin Observatory data collected up to a certain date to produce the calibrated images, catalogs of detections, and derived data products described in Section 3. DP1 was processed entirely at the [United States Data Facility \(USDF\)](#) at SLAC using 17,024 CPU hours.⁹⁴

This section describes the pipeline algorithms used to produce DP1 and how they differ from those planned for full-scale LSST data releases. Data Release Production consists of four major stages: (1) single-frame processing, (2) calibration, (3) coaddition, and (4) difference image analysis (DIA).

1367 by the Rubin scientific community. Version v29.1 of the

1368 pipelines was used to produce DP1⁹⁵.

4.2. Single Frame Processing

4.2.1. Instrument Signature Removal

The first step in processing LSSTComCam images is to correct for the effects introduced by the telescope and detector. Each sensor and its readout amplifiers can vary slightly in performance, causing images of even a uniformly illuminated focal plane to exhibit discontinuities and shifts due to detector effects. The [ISR](#) pipeline aims to recover the original astrophysical signal as best as possible and produce science-ready single-epoch images for source detection and measurement. A detailed description of the [ISR](#) procedures can be found in [P. Fagrelius & E. S. Rykoff \(2025\)](#); [A. A. Plazas Malagón et al. \(2025\)](#). Figure 11 illustrates the model of detector components and readout electronics and their impact on the signal, tracing the process from photons incident on the detector surface to the final quantized values⁹⁶ recorded in the image files. The [ISR pipeline](#) essentially “works backward” through the signal chain, correcting the integer analog-to-digital units (ADU) raw camera output back to a floating-point number of photoelectrons created in the silicon. The physical detector, shown on the left in Figure 11, is the source of effects that arise from the silicon itself, such as the dark current and the brighter-fatter effect ([A. A. Plazas et al. 2018](#);

4.1. LSST Science Pipelines Software

The LSST Science Pipelines software ([Rubin Observatory Science Pipelines Developers 2025](#); [J. D. Swinbank et al. 2020](#)) will be used to generate all Rubin Observatory and LSST data products. It provides both the [algorithms](#) and [middleware](#) frameworks necessary to process raw data into science-ready products, enabling analysis

⁹⁴ For future Data Releases, data processing will be distributed across the USDF, the French (FrDF) and UK (UKDF) data facilities.

⁹⁵ Documentation for this version is available at: https://pipelines.lsst.io/v/v29_1_1

⁹⁶ The images written to disk by the camera have values that are integers that come from the ADC converting an analog voltage.

1394 A. Broughton et al. 2024). After the integration time
 1395 has elapsed, the charge is shifted to the serial register
 1396 and read out, which can introduce charge transfer inef-
 1397 ficiencies and a clock-injected offset level. The signals
 1398 for all amplifiers are transferred via cables to the **Read-**
 1399 **out Electronics Board (REB)**, during which crosstalk
 1400 between the amplifiers may occur. The **Analog Signal**
 1401 **Processing Integrated Circuit (ASPIC)** on the REB con-
 1402 verts the analog signal from the detector into a digital
 1403 signal, adding both quantization and a bias level to the
 1404 image. Although the signal chain is designed to be sta-
 1405 ble and linear, the presence of numerous sources of non-
 1406 linearity indicates otherwise.

1407 The **ISR** processing pipeline for **DP1** performs, in
 1408 the following order: **Analogue-to-Digital Unit (ADU)**
 1409 dithering to reduce quantization effects, serial over-
 1410 scan subtraction, saturation masking, gain normaliza-
 1411 tion, crosstalk correction, parallel overscan subtraction,
 1412 linearity correction, serial **CTI** correction, image assem-
 1413 bly, bias subtraction, dark subtraction, brighter-fatter
 1414 correction, defect masking and interpolation, variance
 1415 plane construction, flat fielding, and amplifier offset
 1416 (amp-offset) correction⁹⁷. Flat fielding for **DP1** was per-
 1417 formed using combined flats produced from twilight flats
 1418 acquired with sufficient rotational dithering to mitigate
 1419 artifacts from print-through stars, as described in §2.3.

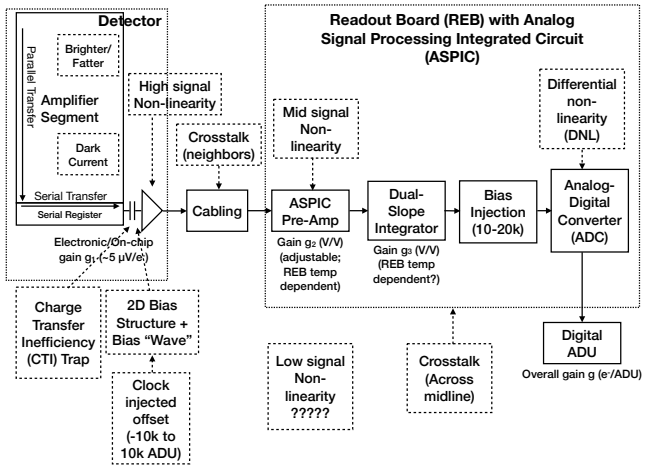


Figure 11. The model of the detector and REB components, labeled with the effects that they impart on signal.

⁹⁷ Amp-offset corrections are designed to address systematic discontinuities in background sky levels across amplifier boundaries. The implementation in the LSST Science Pipelines is based on the Pan-STARRS Pattern Continuity algorithm (C. Z. Waters et al. 2020).

4.2.2. Background Subtraction

1421 The background subtraction algorithms in the LSST
 1422 Science Pipelines estimate and remove large-scale back-
 1423 ground signals from science imaging. Such signals may
 1424 include sky brightness from airglow, moonlight, scat-
 1425 tered light instrumental effects, zodiacal light, and dif-
 1426 fuse astrophysical emission. In so doing, true astrophys-
 1427 ical sources are isolated to allow for accurate detection
 1428 and measurement.

1429 To generate a **background** model, each post-**ISR** image
 1430 is divided into superpixels of 128×128 pixels. Pixels
 1431 with a mask flag set that indicates that they contain
 1432 no useful science data or that they contain **flux** from a
 1433 preliminary source detection are masked. The iterative
 1434 3σ clipped mean of the remaining pixels is calculated
 1435 for each superpixel, constructing a **background** statistics
 1436 image. A sixth-order Chebyshev polynomial is fit to
 1437 these values on the scale of a single detector to allow for
 1438 an extrapolation back to the native pixel resolution of
 1439 the post-**ISR** image.

4.3. Calibration

1441 Stars are detected in each post-**ISR** image using a 5σ
 1442 threshold. Detections of the same star across multiple
 1443 images are then associated to identify a consistent set
 1444 of isolated stars with repeated observations suitable for
 1445 use in PSF modeling, photometric **calibration**, and as-
 1446 trometric **calibration**.

1447 Initial astrometric and photometric solutions are de-
 1448 rived using only the calibration reference catalogs (see
 1449 §3.2), and an initial **PSF** model is fit using PSFEx (E.
 1450 Bertin 2011). These preliminary solutions provide ap-
 1451 proximate source positions, fluxes, and **PSF** shapes that
 1452 serve as essential inputs to the **calibration** process, en-
 1453 abling reliable source matching, selection of high-quality
 1454 stars, and iterative refinement of the final astrometric,
 1455 photometric, and **PSF** models. These preliminary solu-
 1456 tions are subsequently replaced by more accurate fits, as
 1457 described in the following sections.

4.3.1. PSF Modeling

1458 **PSF** modeling in **DP1** uses the Piff (M. Jarvis et al.
 1459 2021) package. Our configuration of Piff utilizes its **Pix-**
 1460 **elGrid** model with a fourth-order polynomial interpola-
 1461 tion per **CCD**, except in the **u**-band, where star counts
 1462 are insufficient to support a fourth-order fit. In this
 1463 case, a second-order polynomial is used instead. Details
 1464 on the choice of polynomial order, overall **PSF** modeling
 1465 performance, and known issues are discussed in §5.2.

4.3.2. Astrometric Calibration

1466 Starting from the astrometric solution calculated in
 1467 single frame processing (§4.2), the final astrometric so-

lution is computed using the ensemble of visits in a given band that overlap a given [tract](#). This allows the astrometric solution to be further refined by using all of the isolated point sources of sufficient signal-to-noise ratio in an image, rather than only those that appear in the reference catalog, as is done in single frame processing. Using multiple whole visits rather than a single detector also allows us to account for effects that impact the full focal plane, and for the proper motion and parallax of the sources.

In order to perform the fit of the astrometric solution, isolated point sources are associated between overlapping visits and with the Gaia [DR3](#) ([Gaia Collaboration et al. 2023b](#)) reference catalog where possible. The model used for [DP1](#) consists of a static map from pixel space to an intermediate frame (the per-detector model), followed by a per-visit map from the intermediate frame to the plane tangent to the telescope boresight (the per-visit model), then finally a deterministic mapping from the tangent plane to the sky. The fit is done using the [gbdes](#) package ([G. M. Bernstein et al. 2017](#)), and a full description is given in [C. Saunders \(2024\)](#).

The per-detector model is intended to capture quasi-static characteristics of the telescope and camera. During [Rubin Operations](#), the astrometric solution will allow for separate epochs with different per-detector models, to account for changes in the camera due to warming and cooling and other discrete events. However, for [DP1](#), [LSSTComCam](#) was assumed to be stable enough that all visits use the same per-detector model. The model itself is a separate two-dimensional polynomial for each detector. For [DP1](#), a degree 4 polynomial was used; the degree of the polynomial mapping is tuned for each instrument and may be different for LSSTCam. Further improvements may be made by including a pixel-based astrometric offset mapping, which would be fit from the ensemble of astrometric residuals, but this is not included in the [DP1](#) processing.

The per-visit model attempts to account for the path of a photon from both atmospheric sources and those dependent on the telescope orientation. This model is also a polynomial mapping, in this case a degree 6 two-dimensional polynomial. Correction for [DCR](#) ([§5.4](#)) was not done for [DP1](#), but will be included in LSSTCam processing during [Rubin Operations](#). Future processing will also likely include a Gaussian Process fit to better account for atmospheric turbulence, as was demonstrated by [W. F. Fortino et al. \(2021\)](#) and [P. F. Léget et al. \(2021\)](#).

The final component of the astrometric [calibration](#) involves the positions of the isolated point sources included in the fit, which are described by five parameters:

sky coordinates, proper motion, and parallax. While proper motions and parallaxes are not released for [DP1](#), they are fitted for these sources in the astrometric solution to improve the astrometric calibration.

4.3.3. Photometric Calibration

Photometric calibration of the [DP1](#) dataset is based on the [Forward Global Calibration Method \(FGCM\)](#) ([FGCM D. L. Burke et al. 2018](#)), adapted for the LSST Science Pipelines ([H. Aihara et al. 2022](#); [P. Fagrelius & E. S. Rykoff 2025](#)). We used the [FGCM](#) to calibrate the full [DP1](#) dataset with a forward model that uses a parameterized model of the atmosphere as a function of airmass along with a model of the instrument throughput as a function of wavelength. The [FGCM](#) process typically begins with measurements of the instrumental throughput, including the mirrors, filters, and detectors. However, because full scans of the [LSSTComCam](#) as-built filters and individual detectors were not available, we instead used the nominal reference throughputs for the Simonyi Survey Telescope and LSSTCam.⁹⁸ These nominal throughputs were sufficient for the [DP1](#) calibration, given the small and homogeneous focal plane consisting of only nine [ITL](#) detectors. The [FGCM](#) atmosphere model, provided by MODTRAN ([A. Berk et al. 1999](#)), was used to generate a look-up table for atmospheric throughput as a function of zenith distance at Cerro Pachón. This model accounts for absorption and scattering by molecular constituents of the atmosphere, including O_2 and O_3 ; absorption by water vapor; and Mie scattering by airborne aerosol particulates. Nightly variations in the atmosphere are modeled by minimizing the variance in repeated observations of stars with a [Signal to Noise Ratio \(SNR\)](#) greater than 10, measured using “compensated aperture fluxes”. These fluxes include a local [background](#) subtraction (see [§4.2.2](#)) to mitigate the impact of [background](#) offsets. The model fitting process incorporates all six bands (*ugrizy*) but does not include any gray (achromatic) terms, except for a linear assumption of mirror reflectance degradation, which is minimal over the short duration of the [DP1](#) observation campaign. As an additional constraint on the fit, we use a subset of stars from the reference catalog ([P. S. Ferguson et al. 2025](#)), primarily to constrain the system’s overall throughput and establish the “absolute” calibration.

4.4. Visit Images and Source Catalogs

With the final [PSF](#) models, [WCS](#) solutions, and photometric calibrations in place, we reprocess each single-

⁹⁸ Available at: <https://github.com/lsst/throughputs/tree/1.9>

epoch image to produce a final set of calibrated visit images and source catalogs. Source detection is performed down to a 5σ threshold using the updated **PSF** models, followed by measurement of **PSF** and aperture fluxes. These catalogs represent the best single-epoch source characterization, but they are not intended for constructing light curves. For time-domain analysis, we recommend using the **forced photometry** tables described in §4.6.2.

4.5. Coaddition Processing

4.5.1. Coaddition

Only exposures with a **seeing** better than 1.7 arcseconds FWHM are included in the deep coadded images. For the template coadds, typically only the top third of visits with the best **seeing** are used (although see §3.1 for more details), resulting in an even tighter image quality cutoff for the template coadds. Exposures with poor **PSF** model quality, identified using internal diagnostics, are excluded to prevent contamination of the coadds with unreliable **PSF** estimates. The remaining exposures are combined using an inverse-variance weighted mean stacking **algorithm**.

To mitigate transient artifacts before coaddition, we apply the artifact rejection procedure described in Y. Al-Sayyad (2018) that identifies and masks features such as satellite trails, optical ghosts, and cosmic rays. It operates on a time series of **PSF**-matched images resampled onto a common pixel grid (“warps”) and leverages their temporal behavior to distinguish persistent astrophysical sources from transient artifacts.

Artifact rejection uses both direct (where no **PSF**-matching is performed) and **PSF**-matched warps, homogenized to a standard **PSF** of 1.8 arcseconds FWHM, broadly consistent with the 1.7 arcsecond FWHM **seeing** threshold used in data screening. A sigma-clipped mean of the **PSF**-matched warps serves as a static sky model, against which individual warps are differenced to identify significant positive and negative residuals. Candidate artifact regions are classified as **transient** if they appear in less than a small percentage of the total number of exposures, with the threshold based on the number of visits, N , as follows:

- $N = 1$ or 2 : threshold = 0 (no clipping).
- $N = 3$ or 4 : threshold = 1.
- $N = 5$: threshold = 2.
- $N > 5$: threshold = $2 + 0.03N$.

Identified **transient** regions are masked before coaddition, improving image quality and reducing contamination in derived catalogs.

4.5.2. Detection, Deblending and Measurement

After constructing coadded images, sources are detected in each band, merged across bands, deblended, and measured to generate the final object catalogs (§3.2). For each coadd in all six bands, we perform source detection at a 5σ detection threshold and then adjust the background with a per-patch constant (coadds are built from background-subtracted images, but the deeper detection on coadds redefines what is considered source versus background). Detections across bands are merged in a fixed priority order, *irzygu*, to form a union detection catalog, which serves as input to deblending.

Deblending is performed using the Scarlet Lite algorithm, which implements the same model as Scarlet (P. Melchior et al. 2018), but operates on a single pixel grid. This allows the use of analytic gradients, resulting in greater computational speed and memory efficiency.

Object measurement is then performed on the deblended detection footprints in each band. Measurements are conducted in three modes: independent per-band measurements, forced measurements in each band, and multiband measurements.

Most measurement algorithms operate through a single-band plugin system, largely as originally described in J. Bosch et al. (2018). The same plugins are run separately for each object on a deblended image, which uses the Scarlet model as a template to re-weight the original noisy coadded pixel values. This effectively preserves the original image in regions where objects are not blended, while dampening the noise elsewhere.

A reference band is chosen for each object based on detection significance and measurement quality using the same priority order as detection merging (*irzygu*) and a second round of measurements is performed in forced mode using the shape and position from the reference band to ensure consistent colors (J. Bosch et al. 2018).

Measurement **algorithm** outputs include object fluxes, centroids, and higher-order moments thereof like sizes and shapes. A variety of **flux** measurements are provided, from aperture fluxes and forward modeling algorithms.

Composite model (CModel) magnitudes (K. Abazajian et al. 2004; J. Bosch et al. 2018) are used to calculate the extendedness parameter, which functions as a star-galaxy classifier. Extendedness is a binary classifier that is set to 1 if the **PSF** model flux is less than 98.5% of the (free, not forced) CModel flux in a given band. Additionally, the extendedness in the reference band is provided as a separate column for convenience as a multiband star-galaxy classification, and is recom-

1670 mended generally but also specifically for objects with
 1671 low signal-to-noise ratio in some bands.

1672 Gaussian-Aperture-and-PSF (Gaussian Aperture and
 1673 PSF (GAaP) K. Kuijken 2008; A. Kannawadi 2025)
 1674 fluxes are provided to ensure consistent galaxy colors
 1675 across bands. Sérsic model (J. L. Sérsic 1963; J. L. Sersic
 1676 1968) fits are run on all available bands simultaneously
 1677 (MultiProFit, D. S. Taranu 2025). The resulting Sérsic
 1678 model fluxes are provided as an alternative to CModel
 1679 and are intended to represent total galaxy fluxes. Like
 1680 CModel, the Sérsic model is a Gaussian mixture approx-
 1681 imation to a true Sérsic profile, convolved with a Gaus-
 1682 sian mixture approximation to the PSF. Sérsic model
 1683 fits also include a free centroid, with all other structural
 1684 parameters shared across all bands. That is, the in-
 1685 trinsic model has no color gradients, but the convolved
 1686 model may have color gradients if the PSF parameters
 1687 vary significantly between bands.

1688 CModel measurements use a double “shapelet” (A.
 1689 Refregier 2003) PSF model with a single shared shape.
 1690 The Sérsic fits are intended to use a double Gaussian
 1691 with independent shape parameters for each component.
 1692 Due to a pipeline misconfiguration, the Sérsic fits actu-
 1693 ally used the shapelet PSF parameters, with the higher-
 1694 order terms ignored (since MultiProFit does not sup-
 1695 port shapelet PSFs). This bug is not expected to im-
 1696 pact the galaxy fluxes significantly, since the higher-
 1697 order shapelet PSF parameters tend to be small, and
 1698 the fix will be applied in future campaigns. Either way,
 1699 the double Gaussian PSF parameters are included for
 1700 each object.

1701 Further details on the performance of these algorithms
 1702 are found in §5.7.

1703 4.6. Variability Measurement

1704 4.6.1. Difference Imaging Analysis

1705 Difference Image Analysis (DIA) uses the decorrelated
 1706 Alard & Lupton image differencing algorithm (D. J.
 1707 Reiss & R. H. Lupton 2016). We detected both pos-
 1708 itive and negative **DIASources** at 5σ in the difference
 1709 image. Sources with footprints containing both positive
 1710 and negative peaks due to offsets from the template po-
 1711 sition or blending were fit with a dipole centroid code,
 1712 , which simultaneously fits offset positive and negative
 1713 PSFs.

1714 We filter a subset of **DIASources** that have pixel
 1715 flags characteristic of artifacts, non-astrophysical trail
 1716 lengths, and unphysically negative direct fluxes. We
 1717 performed a simple spatial association of **DIASources**
 1718 into **DIAObjects** with a one arcsecond matching radius.

1719 The Machine Learning reliability model applied to
 1720 DP1 was developed with the aim to meet the latency

1721 requirements for Rubin Alert Production when executed
 1722 on CPUs. Accordingly we developed a relatively simple
 1723 model: a Convolutional Neural Network with three con-
 1724 volutional layers, and two fully connected layers. The
 1725 convolutional layers have a 5×5 kernel size, with 16, 32,
 1726 and 64 filters, respectively. A max-pooling layer of size 2
 1727 is applied at the end of each convolutional layer, followed
 1728 by a dropout layer of 0.4 to reduce overfitting. The last
 1729 fully connected layers have sizes of 32 and 1. The ReLU
 1730 activation function is used for the convolutional layers
 1731 and the first fully connected layer, while a sigmoid func-
 1732 tion is used for the output layer to provide a probabilistic
 1733 interpretation. The cutouts are generated by extracting
 1734 postage stamps of 51×51 pixels centered on the detected
 1735 sources. The input data of the model consist of the tem-
 1736 plate, science, and difference image stacked to have an
 1737 array of **shape** (3, 51, 51). The model is implemented
 1738 using PyTorch (J. Ansel et al. 2024). The Binary Cross
 1739 Entropy loss function was used, along with the **Adap-
 1740 tive Moment Estimation (Adam)** optimizer with a fixed
 1741 learning rate of 1×10^{-4} , weight decay of 3.6×10^{-2} , and
 1742 a batch size of 128. The final model uses the weights
 1743 that achieved the best precision/purity for the test set.
 1744 Training was done on the **SLAC Shared Scientific Data
 1745 Facility (S3DF)** with an NVIDIA model L40S GPU.

1746 The model was initially trained using simulated data
 1747 from the second DESC Data Challenge (DC2; (LSST
 1748 Dark Energy Science Collaboration (LSST DESC) et al.
 1749 2021)) plus randomly located injections of PSFs to in-
 1750 crease the number of real sources, for a total of 89,066
 1751 real sources. The same number of bogus sources were se-
 1752 lected at random from non-injected **DIASources**. Once
 1753 the **LSSTComCam** data were available, the model was
 1754 fine-tuned on a subset of the data containing 183,046
 1755 sources with PSF injections. On the **LSSTComCam** test
 1756 set, the model achieved an accuracy of 98.06%, purity
 1757 of 97.87%, and completeness of 98.27%. As discussed
 1758 in §5.8, the injections used to train this model version
 1759 do not capture all types of astrophysical variability, so
 1760 performance on the test set will not be representative
 1761 for variable stars, comets, and other types of variable
 1762 objects.

1763 4.6.2. Light Curves

1764 To produce light curves, we perform multi-epoch
 1765 **forced photometry** on both the direct visit images and
 1766 the difference images. For light curves we recom-
 1767 mend the **forced photometry** on the difference images
 1768 (**psDiffFlux** on the **ForcedSource Table**), as it isolates
 1769 the variable component of the flux and avoids contam-
 1770 ination from static sources. In contrast, **forced pho-**
 1771 **tometry** on direct images includes flux from nearby or

blended static objects, and this contamination can vary with seeing. Centroids used in the multi-epoch **forced photometry** stage are taken either from object positions measured on the coadds or from the DIAObjects (the associated DIASources detected on difference images).

4.6.3. Solar System Processing

Solar system processing in **DP1** consists of two key components: the association of observations (sources) with known solar system objects, and the discovery of previously unknown objects by linking sets of *tracklets*⁹⁹.

To generate expected positions, ephemerides are computed for all objects found in the Minor Planet **Center** orbit catalog using the **Sorcha** survey simulation toolkit (Merritt et al., in press)¹⁰⁰. To enable fast lookup of objects potentially present in an observed visit, we use the **mpsky** package (M. Juric 2025). In each image, the closest DiaSource within 1 arcsecond of a known solar system object’s predicted position is associated to that object.

Solar system discovery uses the **heliolinx** package of asteroid identification and linking tools (A. Heinze et al. 2023). The suite consists of the following tasks:

- Tracklet creation with **make_tracklets**
- Multi-night **tracklet** linking with **heliolinc**
- Linkage post processing (orbit fitting, outlier rejection, and de-duplication) with **link_purify**

The inputs to the **heliolinx** suite included all sources detected in difference images produced by an early processing of the **LSSTComCam** commissioning data, including some that were later rejected as part of **DP1** processing and hence are not part of **DP1**.

About 10% of all commissioning visits targeted the near-ecliptic field Rubin_SV_38_7 chosen to facilitate asteroid discovery. Rubin_SV_38_7 produced the vast majority of asteroid discoveries in **DP1**, as expected, but a few were found in off-ecliptic fields as well.

Tracklet creation with **make_tracklets** used an upper limit angular velocity of 1.5 deg/day, faster than any main belt asteroid and in the range of many **Near-Earth Object (NEO)** discoveries. To minimize false tracklets from fields observed multiple times per night, the minimum **tracklet** length was set to three detections, and a minimum on-sky motion of five arcseconds was required for a valid **tracklet**.

⁹⁹ A tracklet is defined as two or more detections of a moving object candidate taken in close succession in a single night.

¹⁰⁰ Available at <https://github.com/dirac-institute/sorcha>

The heart of the discovery **pipeline** is the **heliolinc** task, which connects (“links”) tracklets belonging to the same object over a series of nights. It employs the Heliolinc3D algorithm (S. Eggl et al. 2020; A. Heinze et al. 2022), a refinement of the original HelioLinC algorithm of M. J. Holman et al. (2018).

The **heliolinc** run tested each **tracklet** with 324 different hypotheses spanning heliocentric distances from 1.5 to 9.8 **astronomical unit (au)** and radial velocities spanning the full range of possible bound orbits (eccentricity 0.0 to nearly 1.0). This range of distance encompasses all main belt asteroids and Jupiter Trojans, as well as many comets and Mars-crossers and some **NEOs**. Smaller heliocentric distances were not attempted here because nearby objects move rapidly across the sky and hence were not likely to remain long enough in an **LSSTComCam** field to be discovered. Candidate linkages, groups of tracklets whose propagated orbits cluster within a radius of 1.33×10^3 AU at 1 AU, are identified, then post-processed via **link_purify** to yield a final, non-overlapping set of high-confidence asteroid candidates, ranked by orbit-fit residuals and related metrics.

5. PERFORMANCE CHARACTERIZATION AND KNOWN ISSUES

In this section, we provide an assessment of the **DP1** data quality and known issues.

5.1. Sensor Anomalies and ISR

In addition to the known detector features identified before LSSTComCam commissioning, most of which are handled by the ISR processing (see §4.2.1), we discovered a number of new types of anomalies in the **DP1** data. Since no corrections are currently available for these anomalies, they are masked and excluded from downstream data products.

5.1.1. Vampire Pixels

“Vampire” pixels are visible on the images as a bright defect surrounded by a region of depressed flux, as though the defect is stealing charge from its neighboring pixels. Figure 12 shows an example of a vampire pixel near the center of R22_S11 on an *r*-band flat.

From studies on evenly illuminated images, vampires appear to conserve charge. Unfortunately, no unique optimum way exists to redistribute this stolen flux so, following visual inspection, a defect mask was created to exclude them from processing. We have found some similar features on the ITL detectors on LSSTCam, and will use the same approach to exclude them.

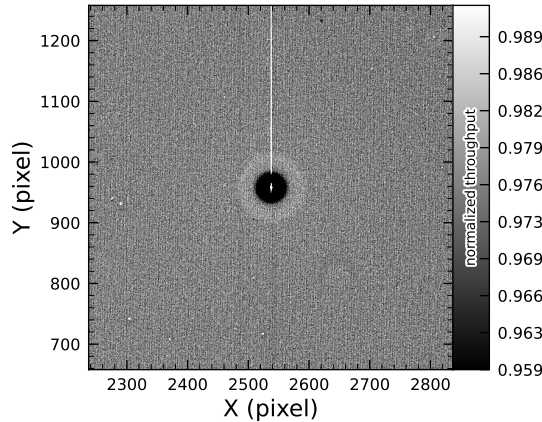


Figure 12. A large vampire pixel near the center of R22_S11, as seen on the *r*-band flat. This clearly shows the central hot "vampire" pixels, surrounded by a region of depressed signal, with a brighter ring surrounding that caused by the local electric field effects. The charge contained in the central pixels is incompletely shifted as the image is read, and that charge leaks out into subsequent rows as they are shifted through the remnant charge. The columns that contain the hot pixels are masked as defects in all processing, as this feature cannot be otherwise corrected.

Figure 13. The top left corner of R22_S01 in the *g*-band flat, showing the many small defect features that are caused by the remnant photoresist wax. A single large defect box masks this region from further analysis to prevent these features from contaminating measurements.

1893 residuals visible on neighboring amplifiers to both sides
1894 on exposure 2024120600239, detector R22_S02.

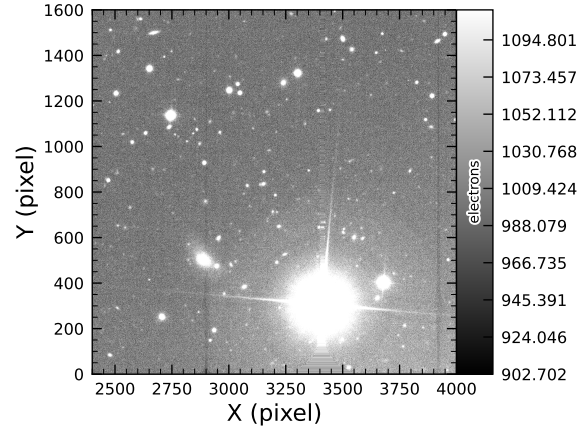


Figure 14. An example of a bright star with over-subtracted crosstalk residuals visible on neighboring amplifiers to both sides (exposure 2024120600239, detector R22_S02). The horizontal banding stretching from the center of the star shows the interpolation pattern covering the saturated core and the ITL edge bleed near the serial register.

5.1.3. Crosstalk

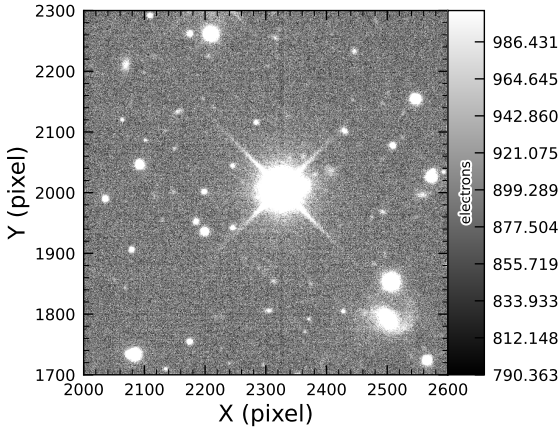
1884 Crosstalk refers to unwanted signal interference be-
1885 tween adjacent pixels or amplifiers. We use an aver-
1886 age inter-amp crosstalk correction based on laboratory
1887 measurements with LSSTCam. These average correc-
1888 tions proved satisfactory, and so have been used as-is
1889 for DP1 processing. There are, however, some residual
1890 crosstalk features present post-correction, with a ten-
1891 dency towards over-subtraction. Figure 14 shows an ex-
1892 ample of a bright star with over-subtracted crosstalk

5.1.4. Bleed Trails

1898 Bleed trails are produced when charge from saturated
1899 pixels spills into adjacent pixels. Bleed trails were an-
1900 ticipated on LSSTComCam sensors, but they appear in
1901 more dramatic forms than had been expected. As a
1902 bleed trail nears the serial register, it fans out into a
1903 "trumpet" shaped feature. Although bright, these fea-

1904 features do not have consistently saturated pixels. In DP1
 1905 these “edge bleeds” were identified and masked.

1906 Saturated sources can create a second type of bleed,
 1907 where the central bleed drops below the background
 1908 level. The depressed columns along these trails extend
 1909 across the entire readout column of the detector, cross-
 1910 ing the detector mid-line. We developed a model for
 1911 these to identify which sources are sufficiently saturated
 1912 to result in such a trail, which is then masked. As this
 1913 kind of trail appears only on the ITL detectors, we’ve
 1914 named these features “ITL dips”. Figure 15 shows an
 1915 example of a bright star exhibiting the “ITL dip” phe-
 1916 nomenon on exposure: 2024121000503, detector: R22_-
 1917 S21.



1918 **Figure 15.** A bright star showing the “ITL dip” phe-
 1919 nomenon, in which a dark trail extends out from the star
 1920 to the top and bottom edges of the detector (exposure:
 1921 2024121000503, detector: R22_S21).

1922
 1923
 1924
 1925
 1926
 1927
 1928
 1929
 1930
 1931
 1932
 1933

5.2. PSF Models

1934 To characterize PSF performance, we use adaptive
 1935 second moments (G. M. Bernstein & M. Jarvis 2002)
 1936 measured on PSF stars and on the PSF model using
 1937 the HSM implementation (C. Hirata & U. Seljak 2003;
 1938 R. Mandelbaum et al. 2005). All measurements are ex-
 1939 pressed in the pixel coordinate frame of each detector.
 1940 We characterize the performance of the PSF using the
 1941 classical trace of the second moment matrix T , along
 1942 with the ellipticity parameters e^1 and e^2 . Measure-
 1943 ments on the observed PSF stars are denoted as
 1944 T_{PSF} , e_{PSF}^1 , e_{PSF}^2 , while those from PSF models are de-
 1945 noted as T_{model} , e_{model}^1 , e_{model}^2 . We compare two PSF
 1946 modeling approaches:

- 1947 • Piff with second-order polynomial interpolation
 1948 (Piff O2), the pipeline’s default, and

Table 4. Observed mean values and comparison of model residuals, across all visits and filters

Quantity	Observed	Piff O2	Piff O4
		$\times 10^{-4}$	$\times 10^{-4}$
$\langle T \rangle$ (pixel 2)	11.366 ± 0.003		
$\langle e^1 \rangle$	$(-6.07 \pm 0.05) \times 10^{-3}$		
$\langle e^2 \rangle$	$(-4.57 \pm 0.05) \times 10^{-3}$		
$\langle e \rangle$	$(8.794 \pm 0.004) \times 10^{-2}$		
$\langle \delta T/T \rangle$		-4.0 ± 0.2	-5.0 ± 0.2
$\langle \delta e^1 \rangle$		0.6 ± 0.1	0.5 ± 0.1
$\langle \delta e^2 \rangle$		0.0 ± 0.1	0.0 ± 0.1

- 1936 • Piff with fourth-order polynomial interpolation
 1937 (Piff O4), which serves as the final DP1 PSF
 1938 model.

1939 **Table 4** summarizes each model’s ability to reconstruct
 1940 the mean T , e^1 , and e^2 on LSSTComCam. Both models
 1941 exhibit a negative residual bias in the reconstructed PSF
 1942 size, with Piff O4 providing improved performance over
 1943 Piff O2.

1944 An alternative approach to evaluating the perfor-
 1945 mance of the PSF model is to examine the average $\delta T/T$,
 1946 where δT is $T_{\text{PSF}} - T_{\text{model}}$, across visits, projected onto
 1947 focal-plane coordinates, as shown in Figure 16. Piff
 1948 reveals strong spatial correlations in the residuals, includ-
 1949 ing a systematic offset consistent with the results pre-
 1950 sented in Table 4. The presence of these spatial struc-
 1951 tures motivated the adoption of fourth-order polynomial
 1952 interpolation in all bands except u -band. Although not
 1953 shown in Figure 16, residual patterns persist even with
 1954 third-order interpolation, indicating that it is insuffi-
 1955 cient to capture the complexity of the PSF variation.
 1956 Increasing the interpolation order to five would nomi-
 1957 nally reduce the residuals further, but the limited num-
 1958 ber of stars available on some CCDs would not provide
 1959 adequate constraints for such a model, while the result-
 1960 ing improvement would likely be minimal. Preliminary
 1961 analysis of LSSTCam data in the laboratory at SLAC
 1962 National Accelerator Laboratory (SLAC) shows that the
 1963 ITL sensors exhibit the same pattern as ITL sensors on
 1964 LSSTComCam.

1965 Another way to look at the PSF modeling quality is
 1966 via whisker plots of the PSF second and fourth moments
 1967 and their modeling residuals projected on a part of the
 1968 sky. In addition to the second moment, the spin-2 fourth

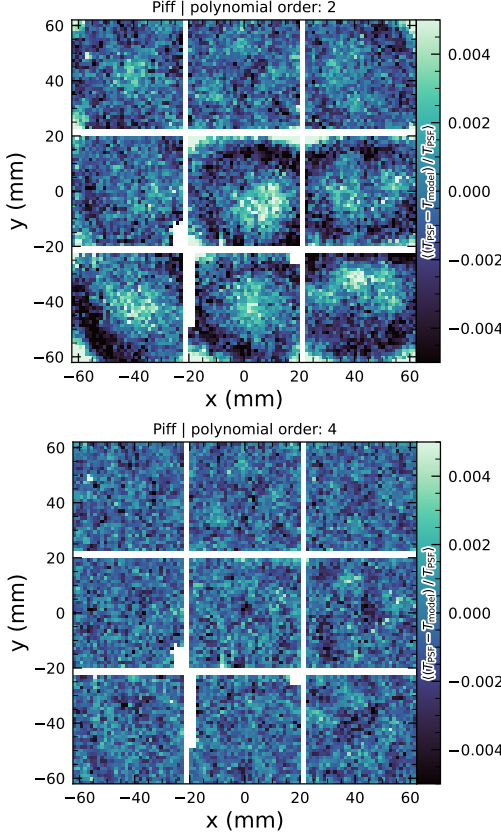


Figure 16. Average across all visits of $\delta T/T$ for Piff O2 and Piff O4 modeling on LSSTComCam. Averages are computed using a 120×120 binning.

moments, $e^{(4)}$, are defined as:

$$e_1^{(4)} = M_{40} - M_{04}$$

$$e_2^{(4)} = 2(M_{31} - M_{13}),$$

where M_{pq} are the standardized higher moments as defined in T. Zhang et al. (2023) measured on stars and PSF models. Figure 17 shows the whisker plots of e , $e^{(4)}$ (top rows), and δe , $\delta e^{(4)}$ in the Extended Chandra Deep Field-South Survey (ECDFS) field. The direction of a whisker represents the orientation of the shape, while the length represents the amplitude $|e|$ or $|e^{(4)}|$. We observe coherent patterns in both the PSF moments and the residuals, the latter of which warrants further investigation if it persists in future data releases. >

Figure 18 shows a plot of $\delta T/T$ versus stellar magnitude, which can reveal any dependencies between PSF size and flux. We also repeat this analysis in color bins to probe chromatic effects. Binning by color uncovers a clear color dependence, as was also seen in DES (M. Jarvis et al. 2021). The residual is consistent with Table 4 and its cause is unknown. DP1 does not include the

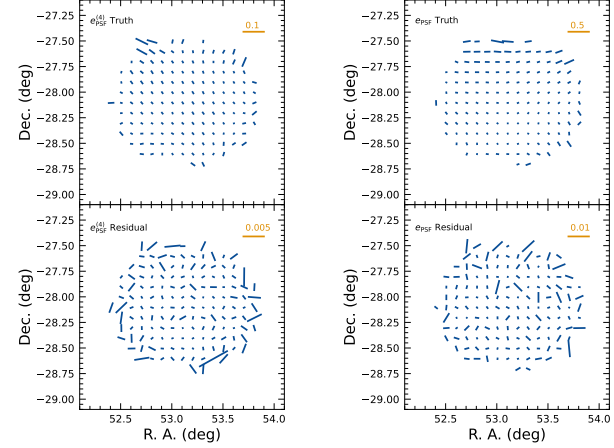


Figure 17. Whisker plots for the ECDFS field for e , $e^{(4)}$ and δe , $\delta e^{(4)}$.

color correction implemented in the DES Year 6 analysis, T. Schutt et al. (2025). This will be included in processing of future data releases.

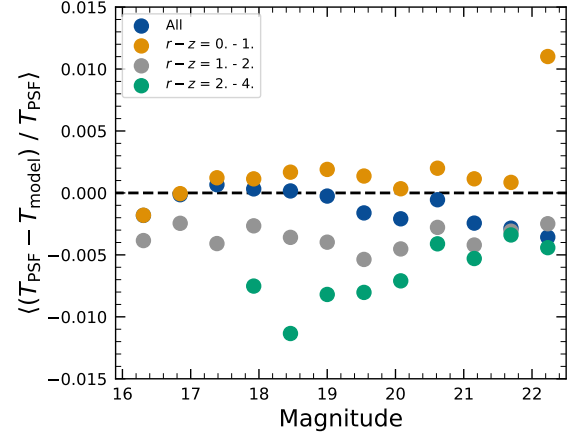


Figure 18. Binned $\delta T/T$ as a function of magnitude across all visits and filters and in bins of stellar colors.

As noted in Rubin Observatory Science Pipelines Developers (2025), two key Piff features were not used in the DP1 processing. PSF color dependence was not implemented, and, while Rubin software allows Piff to work with sky coordinates (including WCS transformations), it does not yet correct for sensor-induced astrometric distortions such as tree rings (H. Y. Park et al. 2017). Both features are planned for upcoming releases.

5.3. Astrometry

To characterize astrometric performance, we evaluate both internal consistency and agreement with an external reference. The primary measure of internal consis-

tency is the repeatability of position measurements for the same object, defined as the RMS of the astrometric distance distribution for stellar pairs having a specified separation in arcminutes. We associate isolated point sources across visits and compute the rms of their fitted positions, rejecting any stars with another star within $2''$. Figure 19 shows the median per-tract rms astrometric error in RA for all isolated point sources, both after the initial calibration and after the final calibration, which includes proper motion corrections. The results indicate that the astrometric solution is already very good after the initial calibration. Global calibration yields only modest improvement, likely due to the short time span of DP1 and the minimal distortions in the LSSTComCam. In the main survey, the longer time baseline and greater distortions near the LSSTCam field edges will make global calibration more impactful. An additional measure of internal consistency is the re-

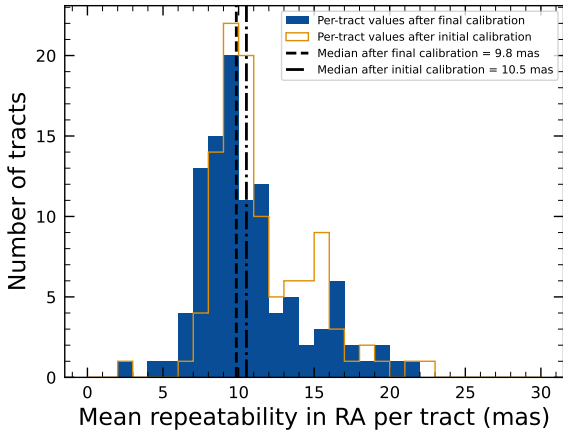


Figure 19. Mean per-tract astrometric repeatability of measurements of isolated point sources in RA in visits across all bands.

peatability of separations between objects at a given distance. To compute this, we identify pairs of objects that are separated by a specified distance and measure their precise separation during each visit in which both objects are observed. The scatter in these separation measurements provides an indication of the internal consistency of the astrometric model. Figure 20 shows the median separation for pairs of objects separated by approximately 5 arcminutes, computed per tract after the final calibration. These values are already approaching the design requirement of 10 mas.

To assess external consistency, we consider the median separation between sources not included in the astrometric fit and associated objects from a reference catalog. For this, we use the Gaia DR3 catalog, with the object

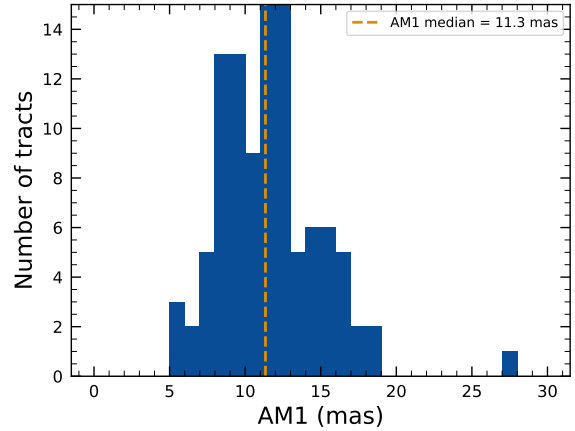


Figure 20. Median per-tract repeatability in separations between isolated point sources 5 arcmin apart in visits across all bands.

positions shifted to the observation epoch using the Gaia proper motion parameters. Figure 21 shows the median separation for each visit in the r -band in tract 4849 in the ECDFS fields (Table 5). The calculated values are almost all within 5 mas, well below the design requirement of 50 mas for the main survey. By examining the astrometric residuals, we can assess whether there are distortions not accounted for by the astrometric model. In some cases, residuals from a single visit exhibit behavior consistent with atmospheric turbulence, as shown in Figure 22, which is characterized by a curl-free gradient field in the two-point correlation function of the residuals (E-mode), P. F. Léget et al. (2021) and W. F. Fortino et al. (2021). However, as seen in Figure 23, the residuals in many visits also have correlation functions with a non-negligible divergence-free B-mode, indicating that some of the remaining residuals are due to unmodeled instrumental effects, such as rotations between visits.

We can see unmodeled camera distortions by stacking the astrometric residuals over many visits as a function of the focal plane position. Figure 24 shows the median residuals in x and y directions for 1792 visits. Spatial structures are evident at the CCD level, as well as at the mid-line break, the discontinuity between the two rows of amplifiers, in the y -direction residuals. Further stacking all the detectors makes certain effects particularly clear. Figure 25 shows distortions very similar to those measured for an LSSTCam ITL sensor in a laboratory setting in J. H. Esteves et al. (2023).

5.4. Differential Chromatic Refraction

Differential Chromatic Refraction (DCR) occurs when light passes through Earth's atmosphere, refracting more for shorter wavelengths, which causes blue light

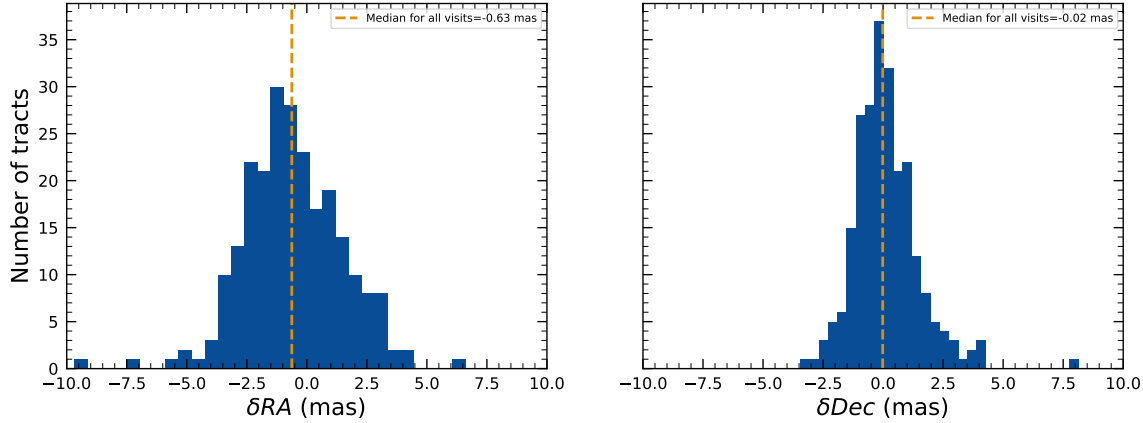


Figure 21. Median absolute offset for all visits in r -band in tract 4849 in the ECDFS field. The offset is the difference between the positions of isolated point sources that were reserved from the astrometric fit and matched objects from the Gaia DR3 catalog.

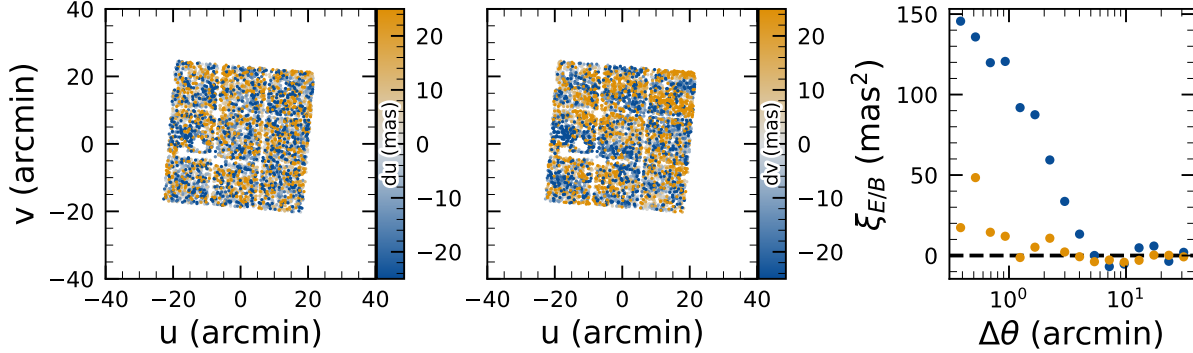


Figure 22. Astrometric residuals in u (left panel) and v (center panel) directions with the E (blue) and B (orange) modes of the two-point correlation function (right panel) seen in visit 2024120200359 in tract 2393 in u band. The residuals show a wave-like pattern characteristic of atmospheric turbulence, and there is significant E-mode and negligible B-mode in the correlation function.

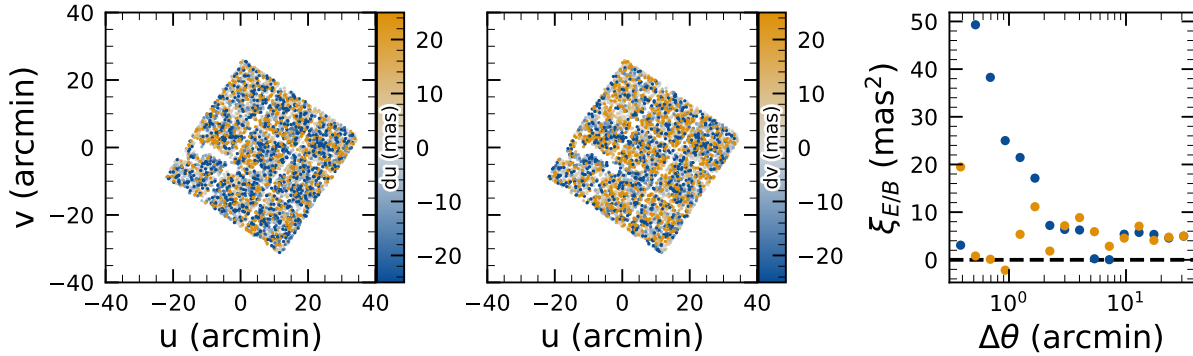


Figure 23. Astrometric residuals in u (left panel) and v (center panel) directions, with the E (blue) and B (orange) modes of the two-point correlation function (right panel) seen in visit 2024120700527 in tract 2393 in u band. There are coherent residuals, but without the wave-like pattern seen in Figure 22, and the correlation function has significant values for both E and B-modes.

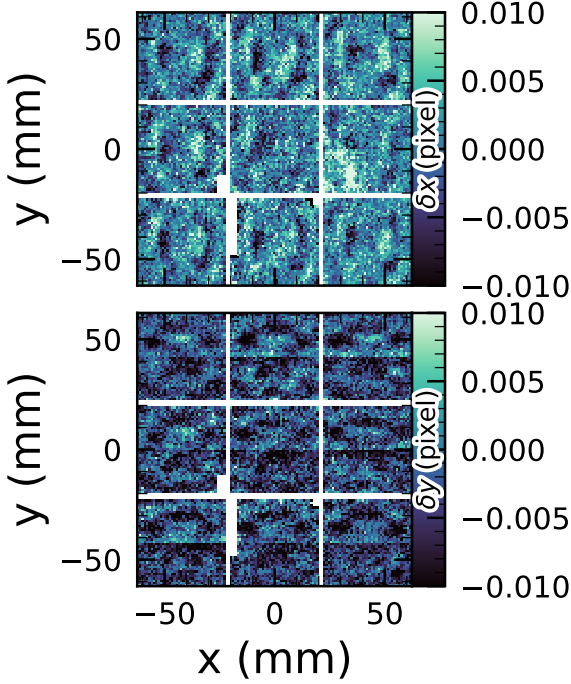


Figure 24. Median astrometric residuals as a function of focal plane position, shown in the left panel for the x direction and in the right panel for the y direction, for all nine LSSTComCam CCDs independently. The range of the color scale is ± 0.01 pixels, corresponding to 2 mas, showing that the effect is small.

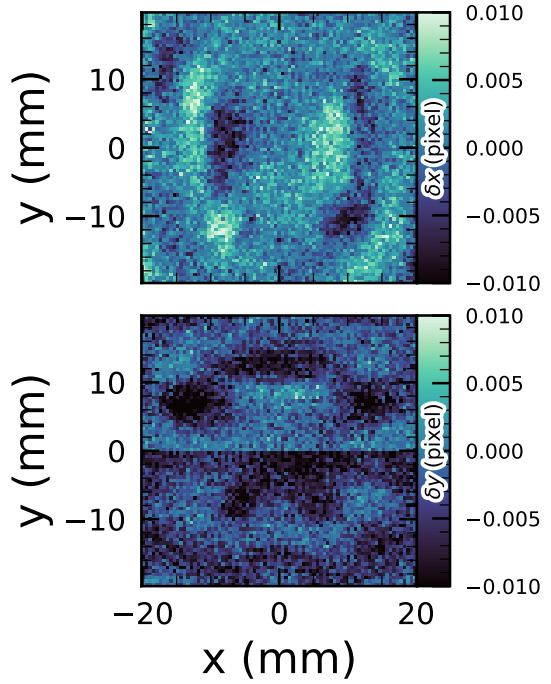


Figure 25. Median residuals as a function of pixel position, shown in the left panel for the x direction and in the right panel for the y direction. These residuals are aggregated across all nine CCDs that comprise the central LSSTComCam raft. The range of the color scale is ± 0.01 pixels, corresponding to 2 mas, showing that the effect is small.

2085 along the zenith direction, specifically parallel to the
 2086 parallactic angle. The DCR effect is observable in
 2087 LSSTComCam data, particularly in the angular offset
 2088 versus $g-i$ band magnitude difference plots, as shown in
 2089 [Figure 26](#). These plots contain 228 visits chosen to max-
 2090 imize the range of observed airmass. When looking at
 2091 data perpendicular to the parallactic angle, sources ex-
 2092 hibit no discernible DCR effect, which is expected, and
 2093 form a clear vertical distribution on the two-dimensional
 2094 density plots in [Figure 26](#).

2095 In contrast, sources aligned with the parallactic angle
 2096 exhibit a tilted, linear distribution, clearly demon-
 2097 strating that the relationship between angular offset and the
 2098 $g-i$ band magnitude difference, thereby providing a vi-
 2099 sual indication of the **DCR** effect. The DCR effect will
 2100 be addressed in future releases.

5.5. Stellar Photometry

2102 The photometric repeatability for isolated bright un-
 2103 resolved sources following the **FGCM** fits was excellent.
 2104 For the 10% of unresolved sources withheld from the fit
 2105 and having signal-to-noise ratios greater than 100, the
 2106 photometric repeatability after applying chromatic cor-

2107 rection was 7.1, 5.4, 5.4, 5.1, 5.9, and 6.5 mmag in the
 2108 *ugriz* bands respectively, across all fields. After ac-
 2109 counting for photometric noise, the intrinsic photomet-
 2110 ric repeatability was approximately 4.8, 2.7, 1.7, 1.0, 2.0,
 2111 and 1.1 mmag in *ugriz*. The DP1 processing does not
 2112 yet include chromatic corrections in the final photome-
 2113 try. In this case the delivered photometric repeatability
 2114 was 3–8 mmag for *griz*.

2115 In [Figure 27](#), we show the stellar loci for *ugriz* for un-
 2116 resolved sources in the DP1 **Object** table ([§3.2](#)). These
 2117 unresolved sources were selected using the extendedness
 2118 parameter ([§3.2](#)) in the **Object** catalog. This parame-
 2119 ter is assigned a value of 0 (unresolved) or 1 (resolved)
 2120 in each band based on the difference between the PSF
 2121 and CModel magnitudes. The extendedness is set to 1
 2122 when this magnitude difference exceeds 0.016 mag, as
 2123 the PSF flux for extended sources is biased low relative
 2124 to the CModel flux. This method has been previously
 2125 employed by the SDSS pipelines, and its statistical prop-
 2126 erties, including the optimal combination of information
 2127 from different bands and repeated measurements, are
 2128 discussed in [C. T. Slater et al. \(2020\)](#).

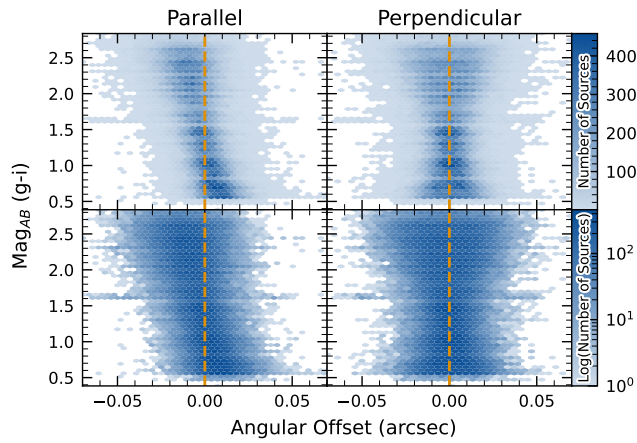


Figure 26. Visualization of Differential Chromatic Refraction (DCR) observed in the LSSTComCam commissioning campaign. The $g - i$ color is computed for every source in the reference catalog that is matched to a direct source in the science image, and the binned density for the full survey is plotted against the angular offset between the reference and detected positions. The angular offset is projected along coordinates parallel and perpendicular to the parallactic angle of the observation, and shows a characteristic correlation along the parallel axis with no correlation along the perpendicular axis. The orange vertical dashed line indicates the expected $g - i$ magnitude distribution at zero angular offset.

Figure 28 illustrates the behavior of the extendness parameter. Its behavior in the g and r bands is similar, with unresolved sources scattered around the vertical line centered on zero. The width of the distribution increases towards fainter magnitudes. Resolved sources are found to the right and the dashed lines in the top panels show the adopted “star-galaxy” separation boundary. The morphology of the two color-magnitude diagrams in the bottom panels suggest that the unresolved sample suffers from increasing contamination by galaxies for $r > 24$. This behavior is consistent with simulation-based predictions from C. T. Slater et al. (2020).

5.6. Detection Completeness on Coadds

We characterize completeness by injecting synthetic sources into coadded images, and by comparing source detections to external catalogs. In both cases, we use a greedy, probabilistic matching algorithm that matches reference objects, in order of descending brightness, to the most likely target within a $0.5''$ radius.

We inject sources in 12 of the patches of the ECDFS region with the deepest coverage. The input catalog contains stars and galaxies from part of the Data Challenge 2 (DC2) simulations (LSST Dark Energy Science Collaboration (LSST DESC) et al. 2021), where the galaxies

consist of an exponential disk and de Vaucouleurs (G. de Vaucouleurs 1948, 1953) bulge. To avoid deblender failures from excessive increases in object density, stars with a total flux (i.e., summed across all six bands) brighter than 17.5 mag are excluded, as are galaxies whose total flux is brighter than 15 mag or fainter than 26.5 mag. Half of the remaining objects are selected for injection. Afterwards, individual bulge and disk components fainter than 29 mag are also excluded, both for computational expediency and because their structural properties are less likely to be representative of real galaxies.

Figure 29 shows completeness as a function of magnitude for these injected objects in the ECDFS field. These completeness estimates are comparable to results from matching external catalogs. Matching to the Hubble Legacy Field catalog (G. Illingworth et al. 2016; K. E. Whitaker et al. 2019) reaches 50% completeness at $F775W = 26.13$, or about $i = 25.83$ from differences in matched object magnitudes. Similarly, completeness drops below 90% at $VIS = 23.80$ from matching to Euclid Q1 (Euclid Collaboration et al. 2025) objects, equivalent to roughly $i = 23.5$. The Euclid imaging is of comparable or shallower depth, so magnitude limits at lower completeness percentages than 90% are unreliable, whereas the HST images cover too small and irregular of an area to accurately characterize 80-90% completeness limits.

At the 80% completeness limit, nearly 20% of objects, primarily injected galaxies, are incorrectly classified as stars based on their reference band extendness. Similarly, the fraction of correctly classified injected stars drops to about 50% at $i = 23.8$ (corresponding to 90% completeness).

This analysis has several caveats. The selection of objects for matching in any catalog is not trivial. Some fraction of the detections are spurious, particularly close to bright stars and their diffraction spikes. Additionally, some objects lie in masked regions of one survey but not another, which has not been accounted for. For injected source matching, the reference catalog does not include real on-sky objects. Based on prior analyses of the DC2 simulations, purity is generally greater than completeness at any given magnitude. Similarly, for bright ($i < 23$) objects classified as stars by reference band extendness, $< 5\%$ are either unmatched to a Euclid or HST object, or misclassified - that is, selecting on extendness alone yields a fairly pure but incomplete sample of stars. We expect to remedy some of these shortcomings in future releases.

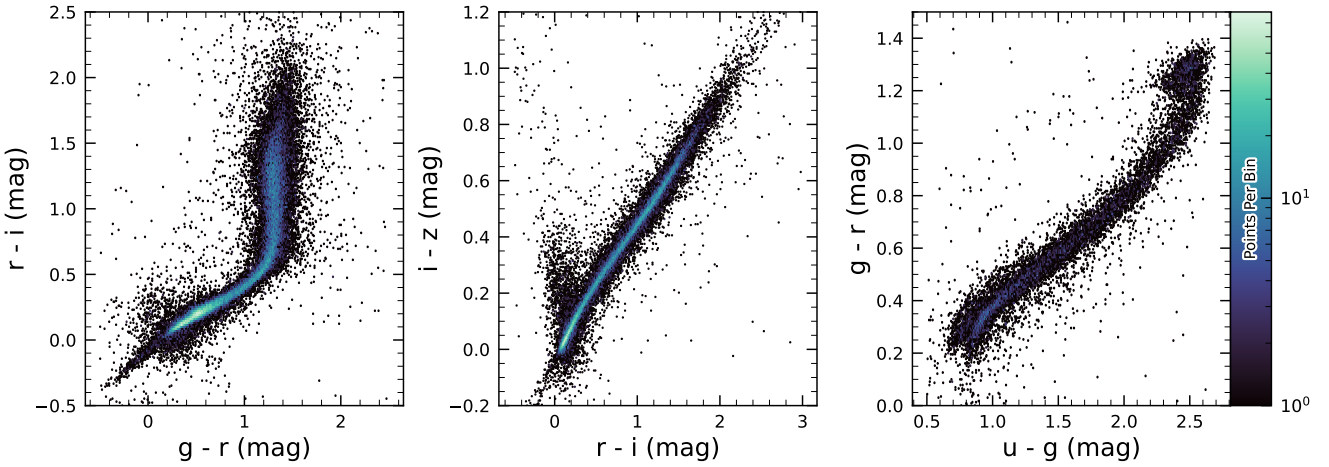


Figure 27. Examples of stellar loci for unresolved sources from the DP1 dataset. From left to right: *gri* stellar locus containing 63,236 stars with signal-to-noise ratio > 200 in the *i* band; *riz* stellar locus containing 46,760 stars with signal-to-noise ratio > 200 in the *i* band *ugr* stellar locus containing 12,779 stars with signal-to-noise ratio > 50 in the *u* band.

5.7. Model Flux and Shape Measurement

Figure 30 shows *i*-band magnitude residuals for CModel and Sérsic measurements using the matched injected galaxies described in §5.6. Similar behavior is seen in other bands. Sérsic fluxes show reduced scatter for galaxies with $i < 22.5$, though CModel fluxes are less biased, with median residuals closer to zero and less magnitude-dependent. For fainter objects, Sérsic fluxes are more biased and less accurate. The magnitude of this bias is considerably larger than previously seen in simulated data. Subsequent testing indicates that this bias can be (roughly) halved by fitting an exponential model first, and then using those parameters to initialize a free Sérsic fit. This approach will be adopted in future releases. Aperture fluxes - including Kron and **GAaP** - are not shown as they are not corrected to yield total fluxes. The correction for Kron fluxes can be derived from the Sérsic index (A. W. Graham & S. P. Driver 2005), but this correction is not provided in object tables.

Figure 31 shows $g - i$ color residuals versus *r*-band magnitude for the same sample of galaxies as Figure 30. For this and most other colors, **GAaP** (with a $1''$ aperture) and Sérsic colors both yield lower scatter; however, the CModel colors have the smallest bias. Curiously, the **GAaP** bias appears to be magnitude-dependent, whereas the Sérsic bias remains stable from $19 < r < 26$. Any of these color measurements are suitable for use for deriving quantities like photometric redshifts, stellar population parameters, etc.

In addition to photometry, some algorithms include measurements of structural parameters like size, ellipticity, and Sérsic index. One particular known issue is

that many (truly) faint objects have significantly overestimated sizes and fluxes. This was also seen in the Dark Energy Survey (K. Bechtol et al. 2025), who dubbed such objects “super-spreaders”. These super-spreaders contribute significantly to overestimated fluxes at the faint end (see e.g. Figure 30), and are particularly problematic for the Kron algorithm (R. G. Kron 1980), which should only be used with caution.

As mentioned in §4.5, the Sérsic fits include a free centroid, which is initialized from the fiducial centroid of the object. Preliminary analyses of matched injected objects suggest that the Sérsic model galaxy **astrometry** residuals are somewhat smaller than for the standard centroids used in other measurements, and so users of the Sérsic photometry should also use these centroid values. One caveat is that for faint objects and/or in crowded regions with unreliable deblending, free centroids can drift significantly and potentially towards other objects, so objects with large differences between the fiducial and Sérsic **astrometry** should be discarded or used with caution.

Sérsic model parameter uncertainties are estimated by computing and inverting the Hessian matrix with the best-fit parameter values, after replacing the pixel data (but not uncertainties) by the best-fit model values. Currently, only the on-diagonal dispersion term (square root of the variance) is provided as an error estimate for each parameter. Future releases may provide more off-diagonal terms of the covariance matrix - particularly for the structural parameters, which are known to be correlated.

A major outstanding issue is that many parameter uncertainties - including but not limited to those for

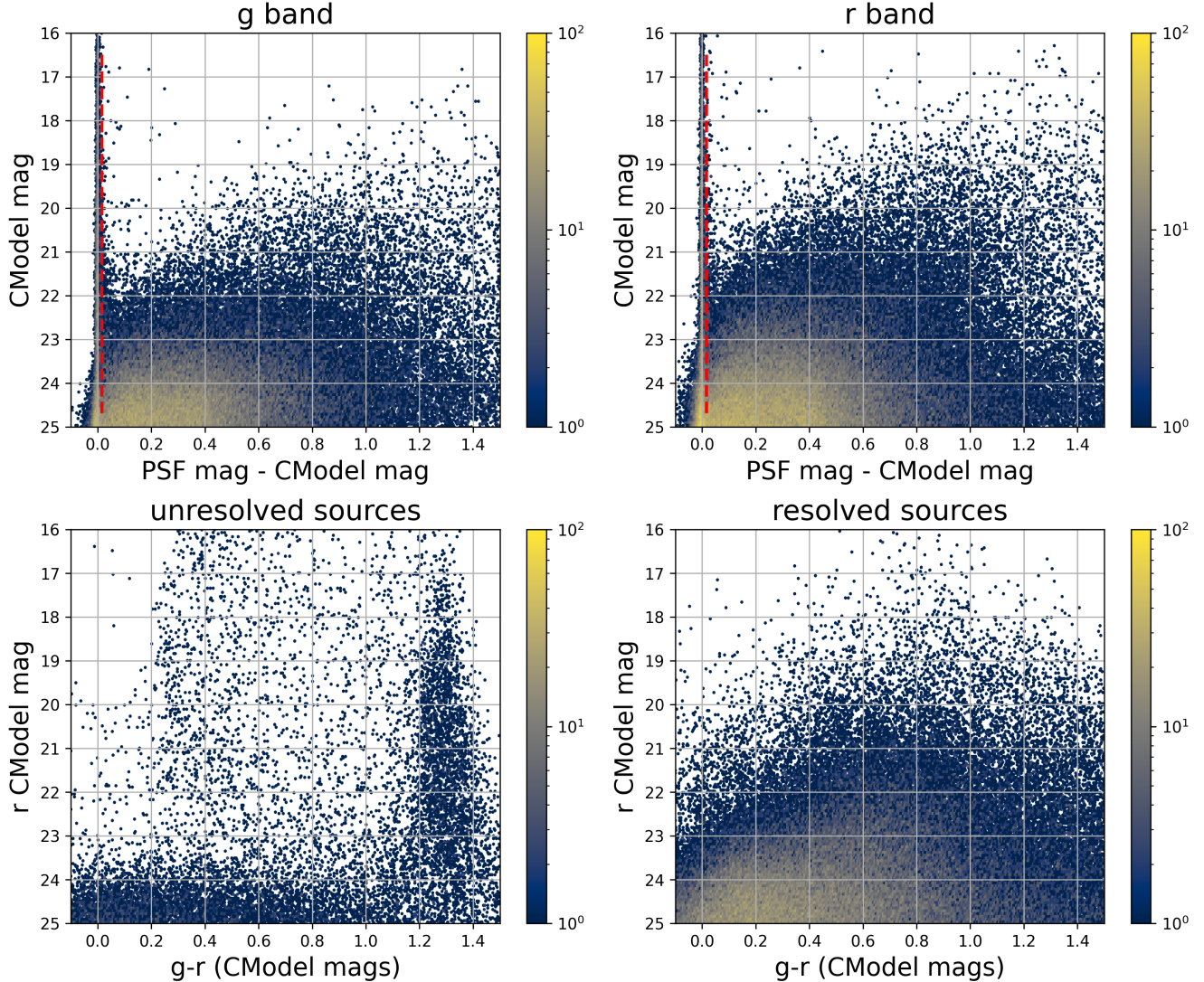


Figure 28. The top two panels shows the difference between the PSF and CModel magnitudes as a function of CModel magnitude in the g and r bands for 178,547 sources with $CModel_r < 25$ from the ECDFS field. The vertical dashed line in each panel marks the minimum value (0.016 mag) for setting the extendedness parameter to 1. The bottom two panels show the r vs. $g - r$ color-magnitude diagrams for 14,701 unresolved (left) and 163,666 resolved (right) sources. Note the unresolved sample suffers from increasing contamination by galaxies for $r > 24$.

2272 fluxes - are underestimated. This is at least partly (but
 2273 not wholly) due to the fact that coaddition introduces
 2274 covariance between pixels, which is not captured in per-
 2275 pixel variances.

2276 The degree to which uncertainties are underestimated
 2277 can depend on the parameter in question and on the
 2278 brightness of the object. In plots of uncertainty-scaled
 2279 residuals, the ideal behavior is for the median (i.e. the
 2280 bias) to lie close to zero, and for the $\pm 1\sigma$ lines to lie at
 2281 ± 1 , without any dependence on magnitude. Figure 32
 2282 shows that flux and color uncertainties for PSF model
 2283 magnitudes of injected stars are both underestimated,
 2284 but by a factor of approximately 1.7 – 2 that is not very

2285 sensitive to **SNR**. This holds for astrometric/centroid
 2286 parameters as well.

2287 In turn, Figure 33 shows that CModel color uncertain-
 2288 ties of galaxies are underestimated by a similar factor at
 2289 the faint end, but with appreciable scaling with mag-
 2290 nitude (and thereby **SNR**). Flux error underestimation
 2291 is both larger than for colors and scales more strongly
 2292 with **SNR**. This indicates that systematic effects domi-
 2293 nate the errors in fluxes, particularly for bright galaxies.
 2294 This is also at least partly but not wholly due to so-
 2295 called model inadequacy - that is, the fact that galaxy
 2296 models, parameteric or otherwise, are insufficiently com-
 2297 plex to capture the structure of real galaxies.

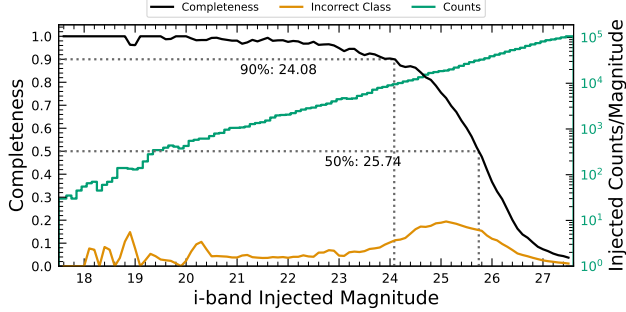


Figure 29. Completeness and incorrect classification fraction as a function of i -band CModel magnitude (Reference Magnitude) for DC2-based injected objects into a portion of the ECDFS field. The “Incorrect Class” line shows the proportion of objects that are matched but classified incorrectly by their reference-band extendedness, i.e. stars with extendedness of 1 or galaxies with extendedness of 0 in the reference band.

Figure 34 shows that Sérsic model fluxes and colors have similar behavior as CModel, but with a greater degree of overestimation. This may be partly due to the fact that Sérsic parameter uncertainties are estimated along with the free centroid and structural (shape and Sérsic index) parameters, whereas the forced CModel fluxes and errors are derived from linear flux fits with a fixed shape and centroid.

Efforts are underway to investigate and quantify the origin of uncertainty underestimates and future releases will, at the least, provide recommendations for mitigations.

5.8. Difference Imaging Purity

We assessed the performance of image differencing using human vetting and source injection (§5.9). Members of the DP1 team labeled more than 9500 DIASource image triplets consisting of cutouts from the science, template, and difference images. We classified these into various real and artifact categories. The raw artifact to real ratio without filtering was roughly 9:1. Bright stars are the main source of artifacts. Correlated noise, primarily in u and g bands, also leads to spurious detections near the flux threshold. We expect to be able to mitigate these effects for LSSTCam.

Applying a reliability threshold improves the purity of transients but not variable stars; technical limitations at the time of model training prevented injection of variable stars into the synthetic training set. Reliability models, described in §4.6.1, for LSSTCam data will be trained on a wider range of input data.

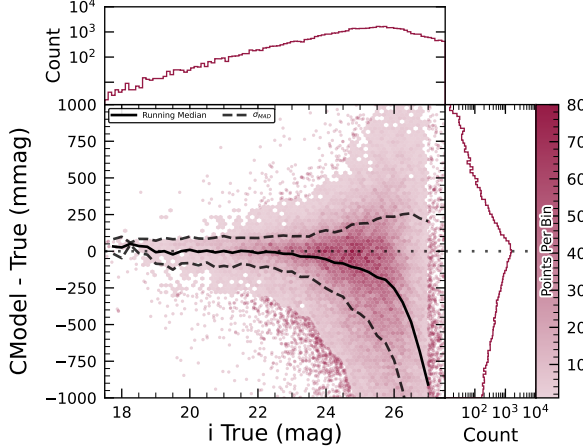
5.9. Difference Imaging Detection Completeness

We assess the performance of our difference imaging pipeline using synthetic source injection on the science images prior to differencing. We construct a catalog of injected sources by joining two different samples of point sources, a set of hosted sources to emulate transients in galaxies and second set of hostless sources. The hosts are selected from the pipeline source catalog that is produced upstream by imposing a cut on their extendedness measurement and selecting $N_{\text{src}} = \min(100, N \times 0.05)$ of the N available sources per detector. For each host we pick a random position angle and radius using its light profile shape to decide where to place the source, and also a random value of brightness for the injected source, with magnitudes higher than the host source.

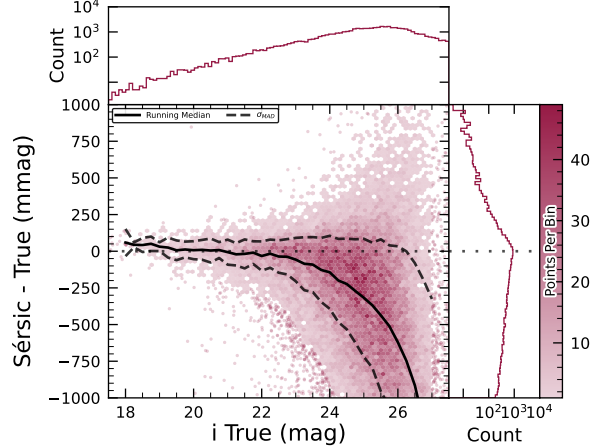
The hostless sources instead have random positions in the CCD focal plane, and magnitudes chosen from a random uniform distribution with $20 \geq m \geq m_{\text{lim}} + 1$, where m_{lim} is the limiting magnitude of the image. We used the LSST source_injection package¹⁰¹ to include these sources in our test images. We performed a coordinate cross-match task, with a threshold of $0.^{\circ}5$ to find which of these sources were detected and which were lost, enabling the calculation of a set of performance metrics.

In Figure 35 we show the detection completeness as a function of the SNR, for sources in the ECDFS field, for filters $griz$. We observe a completeness $> 95\%$ for sources with $\text{SNR} > 6$, with mean completeness $\simeq 99\%$ and standard deviation of $\simeq 0.7\%$. In Figure 36 we show the distribution of the residuals of the recovered sky coordinates for the detected synthetic sources. The marginal distributions are both centered at zero, and for sources of $\text{SNR} > 20$ the residuals are compatible with normal distributions $\mathcal{N}(\mu = 0, \sigma^2 = (0.^{\circ}02)^2)$. In Figure 37 we show photometry results for our detected synthetic sources in the i filter, using PSF photometry on the difference images. We include both the magnitude residuals as well as the flux pulls, defined as $f_{\text{PSF}} - f_{\text{True}})/\sigma_{f_{\text{PSF}}}$ for PSF flux f_{PSF} and error $\sigma_{f_{\text{PSF}}}$, as a function of the true magnitude of the synthetic sources, including the running median and median absolute deviation (MAD) for the whole brightness range. We also include the true magnitude distribution as well as the detection completeness on the top panel, and for reference the 90% and 50% completeness magnitude values in vertical lines. On the right panels we include the marginal distribution for sources brighter

¹⁰¹ <https://pipelines.lsst.io/modules/lsst.source.injection/index.html>

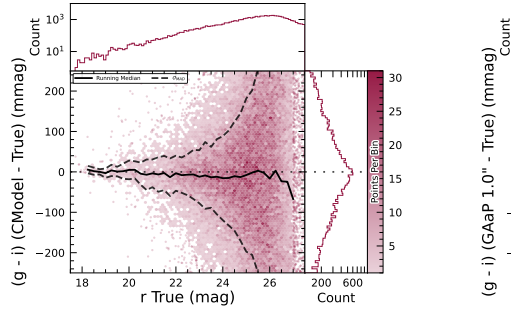


(a) i -band magnitude residuals for CModel measurements of injected galaxies.

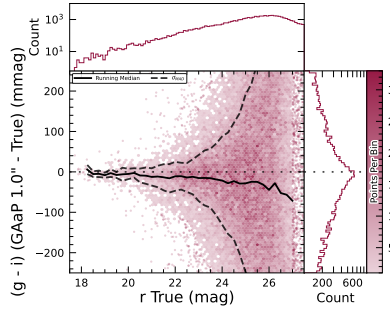


(b) i -band magnitude residuals for Sérsic model measurements of injected galaxies.

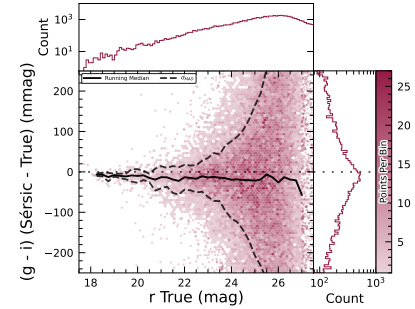
Figure 30. i -band magnitude residuals for matched injected DC2 galaxies with the CModel and Sérsic algorithms in a portion of the ECDFS region, including the median and scatter thereof. The black line is the median.



(a) $g - i$ color residuals for CModel measurements of injected galaxies.



(b) $g - i$ color residuals for GAaP measurements of injected galaxies.



(c) $g - i$ color residuals for Sérsic model measurements of injected galaxies.

Figure 31. $g - i$ color residuals versus true r -band magnitude for matched injected DC2 galaxies with the CModel, GAaP and Sérsic algorithms in a portion of the ECDFS region.

than $mag < 22.5$, splitting the data into hosted and hostless, as well as the robust mean and standard deviation. From this figure we can see that our `flux` measurements are accurate within a wide range of magnitudes, for both hosted and hostless synthetic sources. We find that the median offset is below 0.002 mag for true magnitudes below 21, and with a maximum σ_{MAD} scatter of about 0.02 mag in this range. For true $m_i < 22.5$, the robust running median PSF magnitudes residuals are < 0.02 mag, and when splitting into hosted and hostless both robust median are well below 0.01, and robust σ , i.e. σ_{MAD} are also well below 0.05. For all sources with $m_i < 21.5$ the running median is always $|\langle \delta \rangle| < 0.1$, and $MAD \sigma_\delta < 1$. Extending to sources with $m_i < 22.5$ then hostless sources have a robust mean pull below 0.02, with a robust standard deviation < 1.15 , while these parameters increase to 0.2 and 1.2 for hosted sources,

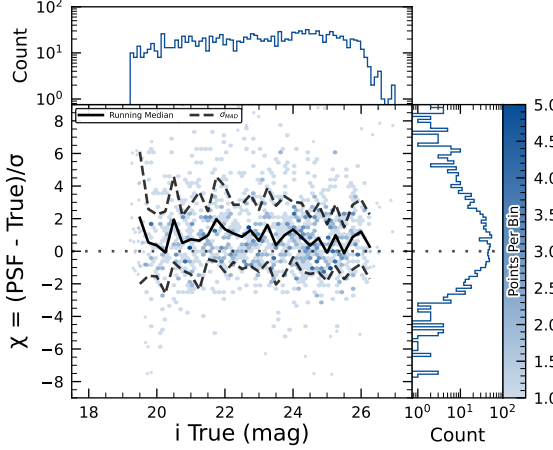
suggesting that we might have contamination from host background sources potentially biasing our fluxes.

5.10. Solar System

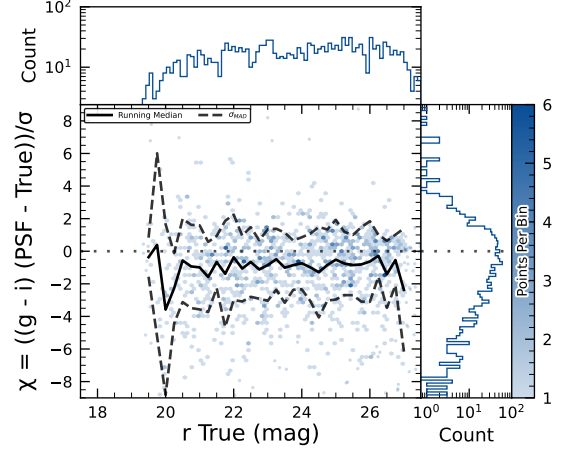
5.10.1. Asteroid Linking Performance

The evaluation of asteroid linking performance in DP1 focused on demonstrating discovery capability. The solar system discovery pipeline produced 269,581 tracklets, 5,691 linkages, and 281 post-processed candidates.

As described in §4.6.3, post-processing of the `heliolinc` output with `link_purify` produced a final set of 281 candidate linkages, ranked with the most promising first. We then used `find_orb` (B. Gray 2025) to derive orbit fits for each candidate, sorting the resulting list by χ_{dof}^2 , a measure of fit quality. A conservative manual investigation of these candidates yielded a curated list of 93 probable new asteroid discoveries. Manual inspection of the linkages indicated that those ranked

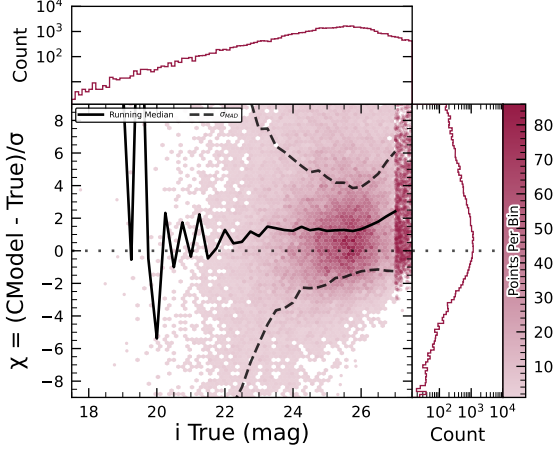


(a) i -band flux uncertainty-scaled residuals for PSF model measurements of injected stars.

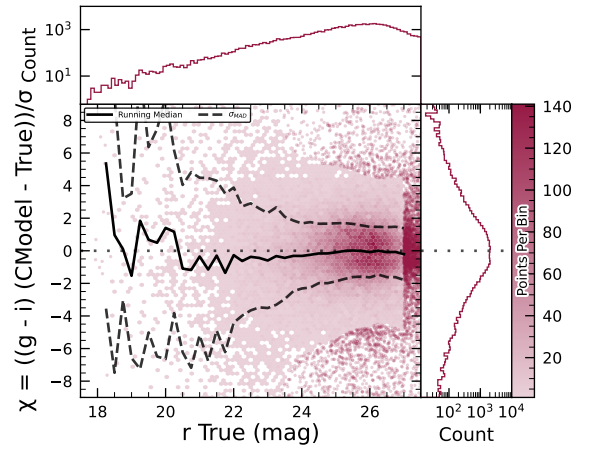


(b) $g - i$ color uncertainty-scaled residuals for PSF model measurements of injected stars.

Figure 32. Color and flux uncertainty-scaled residuals for matched injected DC2 stars' PSF model measurements in a portion of the ECDFS region.



(a) i -band flux uncertainty-scaled residuals for CModel measurements of injected galaxies.



(b) $g - i$ color uncertainty-scaled residuals for CModel measurements of injected galaxies.

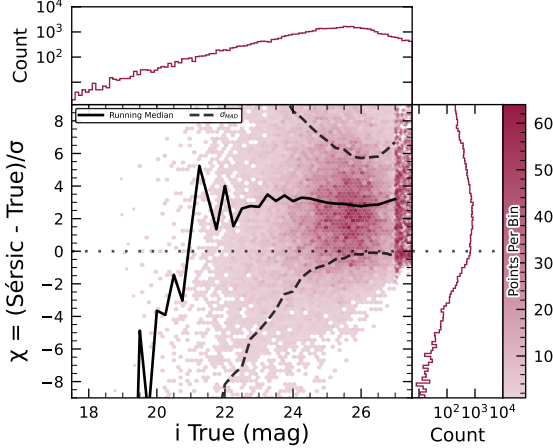
Figure 33. Color and flux uncertainty-scaled residuals for matched injected DC2 galaxies' CModel measurements in a portion of the ECDFS region.

2413 0–137 corresponded to unique real asteroids; ranks 138–
 2414 200 contained additional real objects intermixed with
 2415 some spurious linkages; and ranks higher than 200 were
 2416 essentially all spurious. This analysis indicates that it
 2417 will be possible to identify cuts on quality metrics such
 2418 as χ^2 to define discovery candidate samples with high
 2419 purity; determining the exact quantitative cut values re-
 2420 quires more data with LSSTCam. We next removed all
 2421 observations matched to known asteroids (using Minor
 2422 Planet Center (MPC)'s MPChecker service), reducing
 2423 the number of candidates to 97. Of these, four had
 2424 strong astrometric and/or photometric outliers, likely
 2425 due to self-subtraction in difference images due to the
 2426 unavoidable limitations of template generation from the

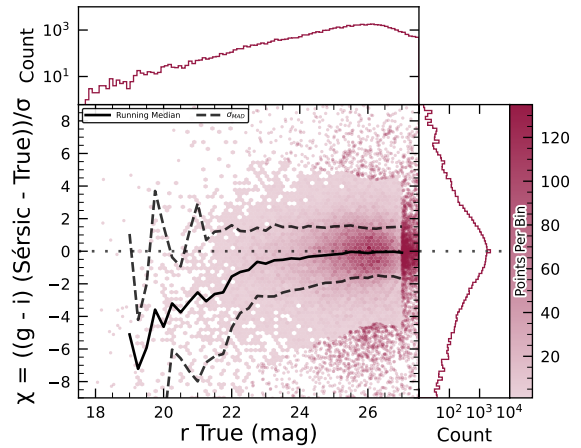
2427 limited quantity of data available from LSSTComCam.
 2428 We suspect these four linkages do correspond to real ob-
 2429 jects, but have chosen to discard them out of an abun-
 2430 dance of caution. The remaining 93 were submitted to
 2431 the Minor Planet Center and accepted as discoveries,
 2432 demonstrating the LSST pipelines are able to success-
 2433 fully discover new solar system objects.

5.10.2. Asteroid Association Performance

2435 During the Solar System association step, 5988 *DiaSources*
 2436 were linked to 431 unique Solar System ob-
 2437 jects. These include 3,934 *DiaSources* with 338 pre-
 2438 viously known objects cataloged by the MPC, and 2,054
 2439 *DiaSources* with the 93 newly-discovered objects. An



(a) i -band flux uncertainty-scaled residuals for Sérsic model measurements of injected galaxies.



(b) $g-i$ color uncertainty-scaled residuals for Sérsic model measurements of injected galaxies.

Figure 34. Color and flux uncertainty-scaled residuals for matched injected DC2 galaxies’ Sérsic measurements in a portion of the [ECDFS](#) region.

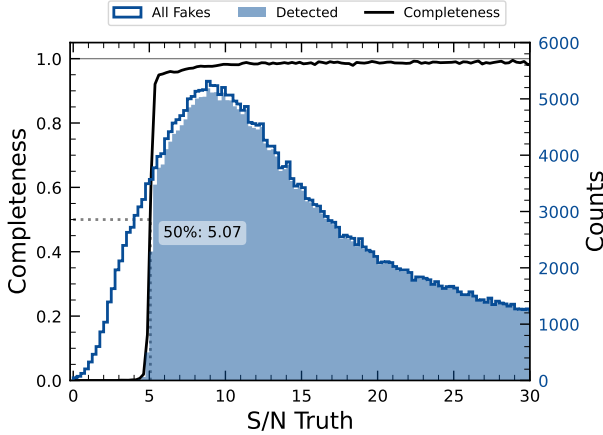


Figure 35. The difference image detection completeness for injected sources in the [ECDFS](#) field, for filters $griz$, as a function of the estimated signal to noise ratio SNR. This completeness is the ratio between the found fake sources (shaded histogram) and all the sources (solid line). The horizontal dashed line represents where the 50% completeness level is reached, at approximately $\text{SNR} \simeq 5.07$.

additional 143 detections of these newly discovered objects were also recovered. These detections were not initially identified by the discovery pipelines, as they did not meet the required criteria for tracklet formation, specifically the minimum number of detections and/or the maximum allowed time span between observations.

The astrometric residuals of known asteroid associations are shown in Figure 38. The astrometric precision for solar system sources is excellent, with the majority of objects detected within $0.^{\circ}1$ of their expected positions. Taking the signed median residuals to search for

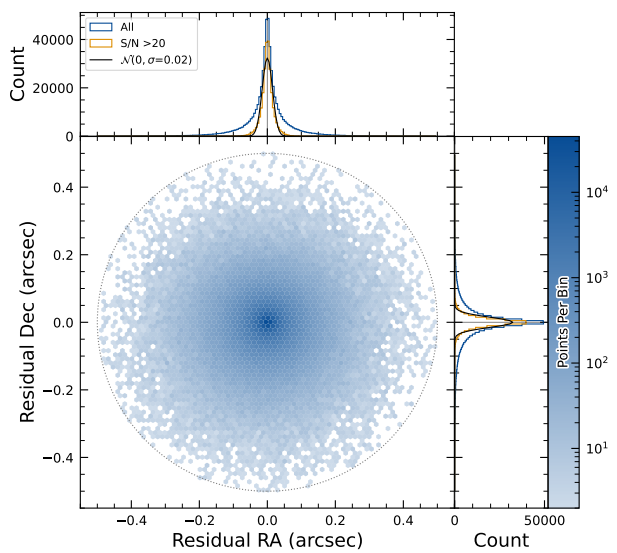


Figure 36. Coordinate residuals for detected synthetic sources in difference images, between recovered and true position of the sources in the [ECDFS](#) field. In the top and right panels we include the distribution of these offsets, for all sources as well as for sources with $\text{SNR} > 20$. These high SNR sources show gaussian coordinate residual distributions with $\sigma = 0.^{\circ}02$ (black solid lines). The circle reflects the matching radius of $0.^{\circ}5$.

biases, we find that previously-known objects have mean residuals of $0.^{\circ}001$ and $-0.^{\circ}016$ in the RA and Dec directions respectively, while newly-discovered objects have mean residuals of $-0.^{\circ}035$ and $-0.^{\circ}010$ in the RA and Dec directions, respectively. These mean residuals are

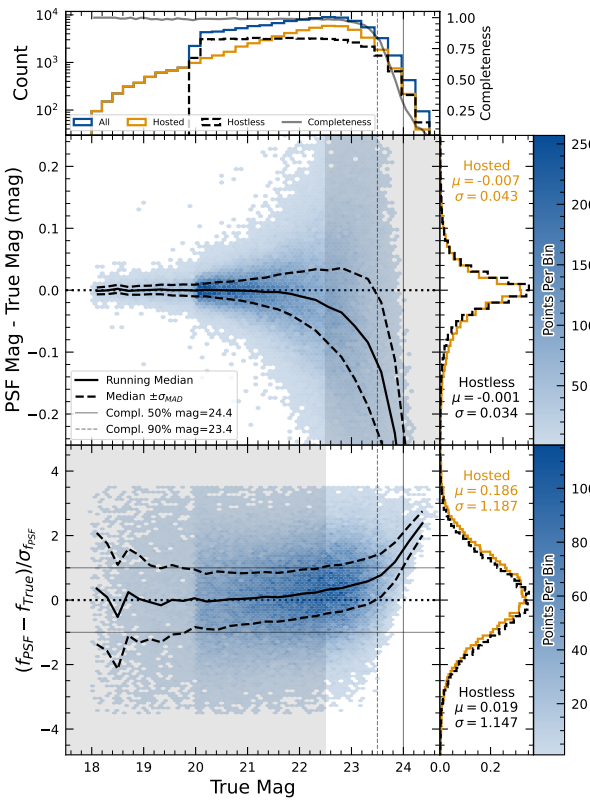


Figure 37. Magnitude residuals and flux pulls for i -band PSF photometry on difference images for ECDFS field in i for detected injected sources. Top panel: Distribution of true magnitudes for injected sources (blue), and split into hostless (black dash) and hosted (orange) sources, with detection completeness as a function of true magnitude (gray line). Vertical dashed lines indicate the 90% and 50% completeness magnitude limits. Center left panel: 2D hexbin plot of PSF magnitude residuals (measured minus true) versus true magnitude for detected sources, with running median (solid black) and σ_{MAD} (dashed black) overlaid. Center right panel: Marginalized distributions of PSF magnitude residuals for hostless (blue) and hosted (orange) sources with true magnitude $m_i < 22.5$, annotated with robust mean and standard deviation. Bottom left panel: 2D hexbin plot of PSF flux pulls versus true magnitude for detected sources, with running median (solid black) and σ_{MAD} (dashed black) overlaid. Bottom right panel: Marginalized distributions of PSF flux pulls for hostless (blue) and hosted (orange) sources with true magnitude $m_i < 22.5$, annotated with robust mean and standard deviation.

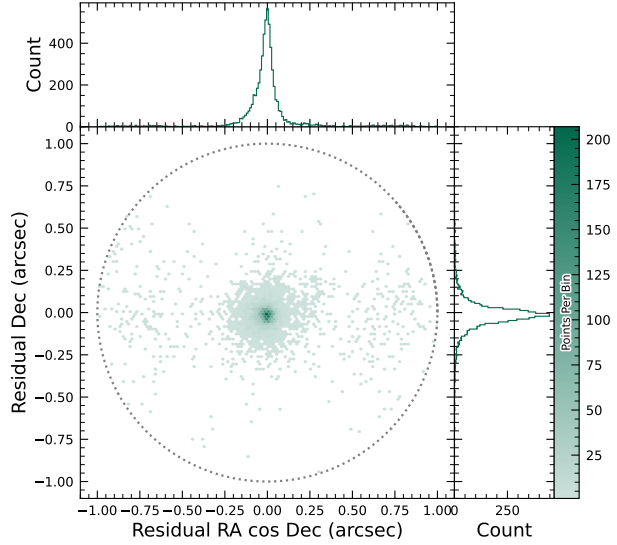


Figure 38. Astrometric residuals between expected and observed positions of Solar System Objects in DP1. The median residuals are $0.^{\circ}001$ and $-0.^{\circ}016$ in R.A./Dec direction, with standard deviations of $0.^{\circ}19$ and $0.^{\circ}10$, respectively. No detectable systematic offset from zero indicates there are no major errors in either timing or astrometry delivered by the Rubin system. The wider scatter in the RA direction is due to objects whose measured orbital elements are less well constrained, translating to larger along-track positional errors in the predicted positions.

2456 small enough to eliminate the possibility of a timing offset
 2457 greater than the second-scale shutter motion, which
 2458 is consistent with the timing studies presented in Section
 2459 2.2.2.

5.11. Crowded Fields

2461 Among the seven Rubin DP1 target fields, two stand
 2462 out for their severe stellar crowding: the globular cluster
 2463 47 Tucanae (47_Tuc) and the Fornax dwarf spheroidal
 2464 galaxy (Fornax dSph). These fields were selected in part
 2465 to stress-test the LSST Science Pipelines under high-
 2466 density conditions. While both exhibit high stellar den-
 2467 sities, the nature and spatial extent of the crowding differ
 2468 significantly.

2469 47 Tuc presents extreme crowding across much of the
 2470 field, encompassing its dense core and the eastern re-
 2471 gions influenced by the Small Magellanic Cloud (SMC).
 2472 This pervasive crowding leads to persistent challenges
 2473 for deblending and reliable source detection, exposing
 2474 field-wide limitations in the current pipeline perfor-
 2475 mance (Y. Choi et al. 2025). In contrast, Fornax dSph
 2476 shows significant crowding only in its central region,

2477 with outer areas remaining well resolved and easier to
 2478 process.

2479 In both 47 Tuc and Fornax, extreme crowding led
 2480 to the deblending step being skipped frequently when
 2481 memory or runtime limits were exceeded, typically due
 2482 to an excessive number of peaks, or large parent foot-
 2483 prints. However, the impact of these limitations dif-
 2484 fered: in 47 Tuc, deblending was often skipped across the
 2485 entire field, resulting in large gaps and substantially re-
 2486 duced completeness. In Fornax, these issues were largely
 2487 confined to the central region, with much better recov-
 2488 ery in the outskirts. This contrast highlights how the
 2489 pipeline’s limitations depend on the spatial extent of
 2490 high-density regions: 47 Tuc exposed systematic, field-
 2491 wide challenges, whereas Fornax revealed more localized,
 2492 density-driven limits.

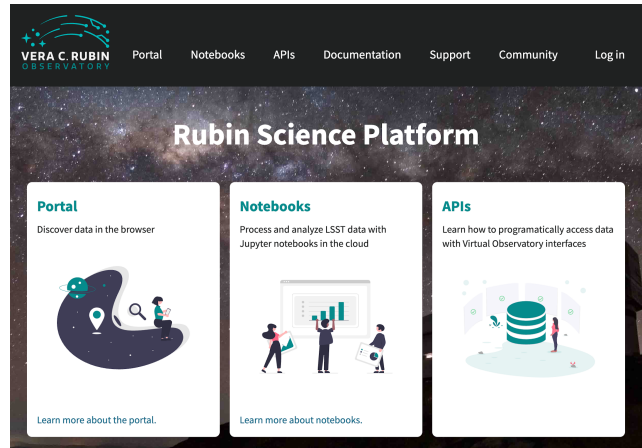
2493 [T. M. Wainer et al. \(2025\)](#) explored the Rubin DP1
 2494 **DiaObject** catalog ([§3.2](#)) in the 47 Tuc field, which
 2495 contains sources detected in difference images. Because
 2496 forced photometry is performed at these positions across
 2497 all single-epoch images, this dataset bypasses the coadd-
 2498 based detection and deblending stages that often fail
 2499 in crowded regions. By computing the median of the
 2500 forced photometry for each **DiaObject** across available
 2501 visits, they recovered approximately three times more
 2502 candidate cluster members than found in the standard
 2503 **Object table** ([Y. Choi et al. 2025](#)). This result under-
 2504 scores the value of difference-imaging-based catalogs
 2505 for probing dense stellar regions inaccessible to standard
 2506 coadd processing in DP1.

2507 Although the DP1 pipeline was not optimized for
 2508 crowded-field photometry, these early studies of 47 Tuc
 2509 and Fornax provide critical benchmarks. They highlight
 2510 both the limitations and opportunities for science with
 2511 Rubin data in crowded environments, and they inform
 2512 future pipeline development aimed at robust source re-
 2513 covery in complex stellar fields.

2514 6. RUBIN SCIENCE PLATFORM

2515 The **RSP** ([M. Jurić et al. 2019](#)) is a powerful, cloud-
 2516 based environment for scientific research and analysis
 2517 of petascale-scale astronomical survey data. It serves
 2518 as the primary interface for scientists to access, visual-
 2519 ize, and conduct next-to-the-data analysis of Rubin and
 2520 LSST data. The **RSP** is designed around a “bring the
 2521 compute to the data” principle, eliminating the need for
 2522 users to download massive datasets. Although **DP1** is
 2523 much smaller in size (3.5 TB) than many current sur-
 2524 vey datasets, future **LSST** datasets will be far larger and
 2525 more complex, making it crucial to co-locate data and
 2526 analysis for effective scientific discovery.

2527 The **RSP** provides users with access to data and
 2528 services through three distinct user-facing Aspects: a
 2529 *Portal*, which facilitates interactive exploration of the
 2530 data; a JupyterLab-based *Notebook* environment for
 2531 data analysis using Python; and an extensive set of
 2532 *Application Programming Interfaces (APIs)* that enable
 2533 programmatic access to both data and services. The
 2534 three Aspects are designed to be fully integrated, en-
 2535 abling seamless workflows across the **RSP**. The data
 2536 products described in [§3](#) are accessible via all three
 2537 Aspects, and the system facilitates operations such as
 2538 starting a query in one Aspect and retrieving its results
 2539 in another. [Figure 39](#) shows the Rubin Science Platform
 2540 landing page in the Google cloud.



2541 **Figure 39.** The Rubin Science Platform landing page at
<https://data.lsst.cloud/> showing the three user-facing As-
 2542 pects as well as links to documentation and support infor-
 2543 mation.

2542 The **RSP** is supported by a number of back-end ser-
 2543 vices, including databases, files, and batch comput-
 2544 ing. Support for collaborative work through shared
 2545 workspaces is also included in the **RSP**.

2546 A preview of the **RSP** was launched on Google Cloud
 2547 in 2022, operating under a shared-risk model to support
 2548 [Data Preview 0](#) ([W. O’Mullane et al. 2024a](#)). This al-
 2549 lowed the community to test the platform, begin prepa-
 2550 rations for science, and provide valuable feedback to in-
 2551 form ongoing development. It was the first time an as-
 2552 tronomical research environment was hosted in a [cloud](#)
 2553 environment. The DP1 release brings major updates to
 2554 **RSP** services, enhancing scientific analysis capabilities.
 2555 The **RSP** remains under active development, with incre-
 2556 mental improvements being rolled out as they mature.
 2557 During the Rubin Early Science Phase, the **RSP** will
 2558 continue to operate under a shared-risk model. This
 2559 section outlines the RSP functionality available at the

2561 time of the DP1 release and provides an overview of
 2562 planned future capabilities.

2563 6.1. Rubin Data Access Center

2564 The Rubin US Data Access Center (US DAC) utilizes
 2565 a novel hybrid on-premises-[cloud](#) architecture, which
 2566 combines on-premises infrastructure at the [USDF](#) at
 2567 SLAC with flexible and scalable resources in the Google
 2568 [cloud](#). This architecture has been deployed and tested
 2569 using the larger simulated data set of DP0.2 ([W.](#)
 2570 [O’Mullane et al. 2024b](#)).

2571 In this hybrid model, user-facing services are deployed
 2572 in the [cloud](#) to support dynamic scaling in response to
 2573 user demand and to simplify the provisioning and man-
 2574 agement of large numbers of science user accounts. The
 2575 majority of the static data products described in §3 are
 2576 stored on-premises at the [USDF](#) to benefit from cost-
 2577 effective mass storage and close integration with Rubin
 2578 data processing infrastructure, also located at the
 2579 [USDF](#). For imaging data, the Data Butler (§6.2.2) pro-
 2580 vides the interface between the [cloud](#)-based users and
 2581 data services, and the on-premises data. For catalog
 2582 data, a [cloud](#)-based TAP client (§6.2.1) submits queries
 2583 to the on-premises [Qserv](#) database cluster (§6.5) and re-
 2584 trieves the results. In the initial DP1 deployment, cat-
 2585 alog data is hosted at the [USDF](#) while image data is
 2586 stored in the [cloud](#). The full hybrid model will be rolled
 2587 out and further tested following the release of DP1. The
 2588 RSP features a single-sign-on authentication and auth-
 2589 orization system to provide secure access for Rubin data
 2590 rights holders ([R. Blum & the Rubin Operations Team](#)
 2591 [2020](#)).

2592 6.2. API Aspect

2593 The [API](#) Aspect provides a comprehensive set of user-
 2594 facing interfaces for programmatic access to the DP1
 2595 data products, through both [IVOA](#)-compliant services
 2596 and the Rubin Data Butler. IVOA services enable stan-
 2597 dard queries and integration with existing tools, while
 2598 the Butler facilitates advanced data processing within
 2599 the LSST Science Pipelines.

2600 At the time of the DP1 release, some [IVOA](#) ser-
 2601 vices are unavailable, and certain data products are
 2602 only accessible via the Butler. This section provides
 2603 an overview of the available [IVOA](#) services and Butler
 2604 access.

2605 6.2.1. IVOA Services

2606 Rubin has adopted a [Virtual Observatory \(VO\)](#)-first
 2607 design philosophy, prioritizing compliance with [IVOA](#)
 2608 standard interfaces to foster interoperability, standard-
 2609 ization, and collaboration. In cases where standardized

2610 protocols have yet to be established, additional services
 2611 have been introduced to complement these efforts. This
 2612 approach ensures that the RSP can be seamlessly inte-
 2613 grated with community-standard tools such as [Tool for](#)
 2614 [OPerations on Catalogues And Tables \(TOPCAT\)](#) ([M.](#)
 2615 [Taylor 2011](#)) and [Aladin](#) ([F. Bonnarel et al. 2000; T.](#)
 2616 [Boch & P. Fernique 2014; M. Baumann et al. 2022](#)), as
 2617 well as libraries such as [PyVO](#) ([M. Graham et al. 2014](#)).

2618 The user-facing [APIs](#) are also used internally within
 2619 the [RSP](#), creating a unified design that ensures consis-
 2620 tent and reproducible workflows across all three Aspects.
 2621 This reduces code duplication, simplifies maintenance,
 2622 and ensures all users, both internal and external, access
 2623 data in the same way. For example, an [Astronomical](#)
 2624 [Data Query Language \(IVOA standard\) \(ADQL\)](#) query
 2625 on the [Object](#) catalog via TAP yields identical results
 2626 whether run from the Portal, Notebook, or an external
 2627 client.

2628 The following [IVOA](#) services are available at the time
 2629 of the DP1 release:

- 2630 • **Table Access Protocol (TAP) Service:** A
 2631 TAP service ([P. Dowler et al. 2019](#)) enables queries
 2632 of catalog data via the IVOA-standard [ADQL](#), a
 2633 dialect of SQL92 with spherical geometry exten-
 2634 sions. The main TAP service for DP1 runs on the
 2635 Rubin-developed [Qserv](#) database (§ 6.5), which
 2636 hosts the core science tables described in §3.2, as
 2637 well as the Visit database. It also provides image
 2638 metadata in the IVOA ObsCore format via the
 2639 standard [ivoa.ObsCore](#) table, making it an “Obs-
 2640 TAP” service (ObsTAP; [M. Louys et al. 2017](#)).
 2641 The TAP service is based on the [Canadian As-
 2642 tronomy Data Centre \(CADC\)](#)’s open-source Java
 2643 TAP implementation¹⁰², modified for the exact
 2644 query language accepted by [Qserv](#). It currently
 2645 supports a large subset of ADQL, with limitations
 2646 documented in the data release materials (see §7.1)
 2647 and exposed via the [TAP capabilities](#) endpoint
 2648 where possible.

2649 The TAP service provides metadata annotations
 2650 consistent with the standard, including table and
 2651 column descriptions, indications of foreign-key re-
 2652 lationships between tables, and column metadata
 2653 such as units and [IVOA](#) Unified Content Descrip-
 2654 tors (UCDs).

- 2655 • **Image Access Services:** Rubin image access
 2656 services are compliant with [IVOA](#) SIAv2 (Sim-
 2657 ple Image Access Protocol, version 2; [T. Jenness](#)

¹⁰² <https://github.com/opencadc/tap>

et al. 2024; P. Dowler et al. 2015) for discovering and accessing astronomical images based on [metadata](#). SIAv2 is a REpresentational State Transfer (REST)-based protocol designed for the discovery and retrieval of image data. It allows, for instance, querying all images in a given band over a defined sky region and time period.

Users identify an image or observation of interest and query the service. The result set includes [metadata](#) about the image, such as the sky position, time, or band, and a data access URL, which includes an IVOA Identifier uniquely identifying the dataset (T. Jenness & G. P. Dubois-Felsmann 2025), allowing the dataset to be retrieved or a cutout requested via [Server-side Operations for Data Access \(IVOA standard\) \(SODA\)](#).

• **Image Cutout Service:** The Rubin Cutout Service (R. Allbery 2023, 2024) is based on the IVOA SODA standard (F. Bonnarel et al. 2017). Users submit requests specifying sky coordinates and the cutout size as the radius from the coordinates, and the service performs the operation on the full image and returns a result set. For DP1, the cutout service is a single cutout service only where N cutout requests will require N independent synchronous calls. We expect some form of bulk cutout service by mid 2026, approximately contemporaneously with DP2.

• **HiPS Data Service:** An authenticated [HiPS](#) (P. Fernique et al. 2017) data service for seamless pan-and-zoom access to large-scale co-adds. It supports fast interactive progressive image exploration at a range of resolutions.

• **WebDAV:** A Web Distributed Authoring and Versioning (WebDav) service is provided to enable users to remotely manage, edit, and organize files and directories on the [RSP](#) as if they were local files on their own computer. This is especially useful for local development.

6.2.2. Data Butler

The Rubin Data Butler (T. Jenness et al. 2022; N. B. Lust et al. 2023), is a high-level interface designed to facilitate seamless access to data for both users and software systems. This includes managing storage formats, physical locations, data staging, and database mappings. A [Butler](#) repository contains two components:

Table 5. Tract coverage of each DP1 field. The size of a tract is larger than the LSSTComCam field of view; however, since each observed field extends across more than one tract, each field covers multiple tracts.

Field Code	Tract ID
47_Tuc	453, 454
ECDFS	4848, 4849, 5062, 5063, 5064
EDFS_comcam	2234, 2235, 2393, 2394
Fornax_dSph	4016, 4017, 4217, 4218
Rubin_SV_095_-25	5305, 5306, 5525, 5526
Rubin_SV_38_7	10221, 10222, 10463, 10464, 10704, 10705
Seagull	7610, 7611, 7849, 7850

- the *Data Store*: A physical storage system for datasets, e.g., a [Portable Operating System Interface \(POSIX\)](#) file system or S3 object store; and
- the *Registry*: An [Structured Query Language \(SQL\)](#)-compatible database that stores metadata about the datasets in the data store.

For DP1, the Butler repository is hosted in the Google Cloud, using an [\(Amazon\) Simple Storage Service \(S3\)](#)-compatible store for datasets and AlloyDB, a PostgreSQL-compatible database, for the registry.

In the context of the [Butler](#), a *dataset* refers to a unique data product, such as an image, catalog or map, generated by the observatory or processing pipelines. Datasets belong to one of the various types of data products, described in §3. The [Butler](#) ensures that each dataset is uniquely identifiable by a combination of three pieces of information: a data coordinate, a dataset type, and a run collection. For example, a dataset that represents a single raw image in the i band taken on the night starting 2024-11-11 with exposure ID 2024111100074 would be represented as `dataId='exposure':2024111100074, 'band':'i', 'instrument':'LSSTComCam'` and is associated with the `raw` `DatasetType`. For a deep coadd on a `patch` of sky in the Seagull field, there would be no exposure dimensions and instead the tract, `patch` and band would be specified as `dataId='tract':7850, 'patch':6, 'band':'g', 'instrument':'LSSTComCam', 'skymap='lsst_cells_v1'` and is associated with the `deep_coadd` `DatasetType`. The tract identification numbers and corresponding target names for these tracts are listed in [Table 5](#).

The data coordinate is used to locate a dataset in multi-dimensional space, where dimensions are defined

Table 6. Descriptions of and valid values for the key data dimensions in DP1. YYYYMMDD signifies date and # signifies a single 0–9 digit.

Dimension	Format/Valid values	Description
day_obs	YYYYMMDD	A day and night of observations that rolls over during daylight hours.
visit	YYYYMMDD#####	A sequence of observations processed together; synonymous with “exposure” in DP1.
exposure	YYYYMMDD#####	A single exposure of all nine ComCam detectors.
instrument	LSSTComCam	The instrument name.
detector	0–8	A ComCam detector.
skymap	lsst_cells_v1	A set of tracts and patches that subdivide the sky into rectangular regions with simple projections and intentional overlaps.
tract	See Table 5	A large rectangular region of the sky.
patch	0–99	A rectangular region within a tract.
physical_filter	u_02, g_01, i_06, r_03, z_03, y_04	A physical filter.
band	u, g, r, i, z, y	An conceptual astronomical passband.

in terms of scientifically meaningful concepts, such as instrument, visit, detector or band. For example, a calibrated single-visit image (§3.1) has dimensions including band, instrument, and detector. In contrast, the visit table (§3.2), a catalog of all calibrated single-epoch visits in DP1, has only the instrument dimension. The main dimensions used in DP1 are listed, together with a brief description, in Table 6. To determine which dimensions are relevant for a specific dataset, the Butler defines dataset types, which associate each dataset with its specific set of relevant dimensions, as well as the associated Python type representing the dataset. The dataset type defines the kind of data a dataset represents, such as a raw image (raw), a processed catalog (object_forced_source), or a sky map (skyMap). Table 7 lists all the dataset types available via the Butler in DP1, together with the dimensions needed to uniquely identify a specific dataset and the number of unique datasets of each type.

It is important to highlight a key difference between accessing catalog data via the TAP service versus the Butler. While the TAP service contains entire catalogs, many of the same catalogs in the Butler are split into multiple separate catalogs. This is partly due to how these catalogs are generated, but also because of the way data is stored within and retrieved from the Butler repository – it is inefficient to retrieve the entire Source catalog, for example, from the file system. Instead, because the Source catalog contains data for sources detected in the visit_images, there is one Source catalog in the Butler for each visit_image. Similarly, there is one Object catalog for each deep_coadd. All the catalogs described in §3.2, aside from the CcdVisit, SSOB-

ject, SSSource, and Calibration catalogs, are split within the Butler.

A dataset is associated with one or more Collections; logical groupings of datasets within the Butler system that were created or processed together by the same batch operation. Collections allow multiple datasets with the same data coordinate to coexist without conflict. Collections support flexible, parallel processing by enabling repeated analyses of the same input data using different configurations.

For DP1, a subset of the consolidated database contents (§6.5.2) is accessible through the Data Butler. However, not all metadata from the Visit table (§3.5) are available. The DP1 Butler is read-only; a writeable Butler is expected by mid-2026, around the time of DP2.

6.2.3. Remote Programmatic Access

The Rubin RSP API can be accessed from a local system by data rights holders outside of the RSP, by creating a user security token. This token can then be used as a bearer token for API calls to the RSP TAP service. This capability is especially useful for remote data analysis using tools such as TOPCAT, as well as enabling third-party systems, e.g., Community Alert Brokers, to access Rubin data. Additionally, it supports remote development, allowing for more flexible workflows and integration with external systems.

6.3. Portal Aspect

The Portal Aspect provides an interactive web-based environment for exploratory data discovery, filtering, querying, and visualization of both image and catalog data, without requiring programming expertise. It en-

Table 7. The name and number of each type of data product in the Butler and the dimensions required to identify a specific dataset.

Data Product	Name in Butler	Required Dimensions	Number in DP1
Image Data Products			
raw	raw	instrument, detector, exposure	16125
visit_image	visit_image	instrument, detector, visit	15972
deep_coadd	deep_coadd	band, skymap, tract, patch	2644
template_coadd	template_coadd	band, skymap, tract, patch	2730
difference_image	difference_image	instrument, detector, visit	15972
Catalog Data Products			
Source	source	instrument, visit	1786
Object	object	skymap, tract	29
ForcedSource	object_forced_source	skymap, tract, patch	636
DiaSource	dia_source	skymap, tract	25
DiaObject	dia_object	skymap, tract	25
ForcedSourceOnDiaObject	dia_object_forced_source	skymap, tract, patch	597
SSSource	ss_source	—	1
SSObject	ss_object	—	1
Visit	visit_table	instrument	1
CCDVisit	visit_detector_table	instrument	1

ables users to access and analyze large datasets via tools for catalog queries, image browsing, time-series inspection, and cross-matching.

The Portal is built on [Firefly](#) (X. Wu et al. 2019), a web application framework developed by the Infrared Processing and Analysis Center (IPAC). [Firefly](#) provides interactive capabilities such as customizable table views, image overlays, multi-panel visualizations, and synchronized displays linking catalog and image data.

Designed to support both exploratory data access and detailed scientific investigation, the Portal delivers an intuitive user experience, allowing users to visually analyze data while retaining access to underlying metadata and query controls.

6.4. Notebook Aspect

The Notebook Aspect provides an interactive, web-based environment built on Jupyter Notebooks, enabling users to write and execute Python code directly on Rubin and [LSST](#) data without downloading it locally. It offers programmatic access to Rubin and [LSST](#) data products, allowing users to query and retrieve datasets, manipulate and display images, compute derived properties, plot results, and reprocess data using the [LSST](#) Science Pipelines (§4.1). The environment comes pre-installed with the pipelines and a broad set of widely used astronomical software tools, supporting immediate and flexible data analysis.

6.5. Databases

The user-facing Aspects of the [RSP](#) are supported by several backend databases that store catalog data products, image metadata, and other derived datasets. The [schema](#) for DP1 and other Rubin databases are available online at <https://sdm-schemas.lsst.io>.

6.5.1. [Qserv](#)

The final 10-year [LSST](#) catalog is expected to reach 15 PB and contain measurements for billions of stars and galaxies across trillions of detections. To support efficient storage, querying, and analysis of this dataset, Rubin Observatory developed [Qserv](#) (D. L. Wang et al. 2011; F. Mueller et al. 2023) – a scalable, parallel, distributed SQL database system. [Qserv](#) partitions data over approximately equal-area regions of the celestial sphere, replicates data to ensure resilience and high availability, and uses shared scanning to reduce overall I/O load. It also supports a package of scientific user-defined functions (SciSQL: <https://smonkewitz.github.io/scisql/>) simplifying complex queries involving spherical geometry, statistics, and photometry. [Qserv](#) is built on robust production-quality components, including MariaDB (<https://www.mariadb.org/>) and XRootD (<https://xrootd.org/>). [Qserv](#) runs at the [USDF](#) and user access to catalog data is via the TAP service (§6.2.1). This enables catalog-based analysis through both the [RSP](#) Portal and Notebook Aspects.

2858 Although the small **DP1** dataset does not require
 2859 Qserv's full capabilities, we nevertheless chose to use
 2860 it for **DP1** to accurately reflect the future data access
 2861 environment and to gain experience with scientifically-
 2862 motivated queries ahead of full-scale deployment. **Qserv**
 2863 is open-source and available on GitHub: <https://github.com/lsst/qserv>.

2865 6.5.2. *Consolidated Database*

2866 The Consolidated Database (ConsDB) (K.-T. Lim
 2867 2025) is an SQL-compatible database designed to store
 2868 and manage metadata for Rubin Observatory science
 2869 and calibration images. Metadata are recorded on a per-
 2870 exposure basis and includes information such as the tar-
 2871 get name, pointing coordinates, observation time, physi-
 2872 cal filter and band, exposure duration, and environmen-
 2873 tal conditions (e.g., temperature, humidity, and wind
 2874 speed). These key image metadata are also stored in
 2875 the Butler Registry (§6.2.2), however the ConsDB stores
 2876 additional information including derived metrics from
 2877 image processing and information from the **Engineering**
 2878 and **Facility Database (EFD)** transformed from the time
 2879 dimension to the exposure dimension.

2880 The ConsDB schema is organized into instrument-
 2881 specific tables, e.g., **LSSTComCam** and LSSTCam, fa-
 2882 cilitating instrument-specific queries. Within the **LSST-**
 2883 **ComCam** schema, data is further structured into ta-
 2884 bles for individual exposures and detectors. An example
 2885 query on the **DP1** dataset might retrieve all visits within
 2886 a specified time range in the r-band for a given **DP1** tar-
 2887 get.

2888 The ConsDB is hosted at the **USDF**. Following the
 2889 initial release of DP1, a release of the DP1 exposure-
 2890 specific ConsDB data will be made available through the
 2891 **RSP**, and accessible externally via TAP. The detailed
 2892 **LSSTComCam** schema can be found at: [https://sdm-](https://sdm-schemas.lsst.io/cdb_lsstcomcam.html)
 2893 [schemas.lsst.io/cdb_lsstcomcam.html](https://sdm-schemas.lsst.io/cdb_lsstcomcam.html)

2894 7. SUPPORT FOR COMMUNITY SCIENCE

2895 The Rubin Observatory has a science community that
 2896 encompasses thousands of individuals worldwide, with
 2897 a broad range of experience and expertise in astronomy
 2898 in general, and in the analysis of optical imaging data
 2899 specifically.

2900 Rubin's model to support this diverse community to
 2901 access and analyze **DP1** emphasizes self-help via docu-
 2902 mentation and tutorials, and employs an open platform
 2903 for asynchronous issue reporting that enables crowd-
 2904 sourced solutions. These two aspects of community sup-
 2905 port are augmented by virtual engagement activities. In
 2906 addition, Rubin supports its Users Committee to advo-
 2907 cate on behalf of the science community, and supports
 2908 the eight **LSST** Science Collaborations (§7.6).

2909 All of the resources for scientists that are discussed in
 2910 this section are discoverable by browsing the For Scien-
 2911 tists pages of the Rubin Observatory website¹⁰³.

2912 7.1. *Documentation*

2913 The data release documentation for DP1¹⁰⁴ provides
 2914 an overview of the LSSTComCam observations, detailed
 2915 descriptions of the data products, and a high-level sum-
 2916 mary of the processing pipelines. Although much of its
 2917 content overlaps significantly with this paper, the doc-
 2918 umentation is presented as a searchable, web-based re-
 2919 source built using Sphinx¹⁰⁵, with a focus on enabling
 2920 scientific use of the data products.

2921 7.2. *Tutorials*

2922 A suite of tutorials (N.-D. V. C. R. Observatory 2021)
 2923 that demonstrate how to access and analyze **DP1** using
 2924 the RSP accompanies the **DP1** release¹⁰⁶. Jupyter Note-
 2925 book tutorials are available via the “Tutorials” drop-
 2926 down menu within the Notebook aspect of the **RSP**.
 2927 Tutorials for the Portal and API aspects of the **RSP** can
 2928 be found in the data release documentation.

2929 These tutorials are designed to be inclusive, accessi-
 2930 ble, clear, focused, and consistent. Their format and
 2931 contents follow a set of guidelines (M. L. Graham et al.
 2932 2025) that are informed by modern standards in tech-
 2933 nical writing.

2934 7.3. *Community Forum*

2935 The venue for all user support is the Rubin Commu-
 2936 nity Forum¹⁰⁷.

2937 Questions about any and all aspects of the Rubin
 2938 data products, pipelines, and services – including **DP1**
 2939 – should be posted as new topics in the Support cate-
 2940 gory. This includes beginner-level and “how-to” ques-
 2941 tions, advanced scientific analysis questions, technical
 2942 bug reports, account and data access issues, and every-
 2943 thing in between. The Support category of the Forum
 2944 is monitored by Rubin staff, who follow an established
 2945 internal workflow for following-up and resolving all re-
 2946 ported issues.

2947 The Rubin Community Forum is built on the open-
 2948 source Discourse platform. It was chosen because, for
 2949 a worldwide community of ten thousand Rubin users, a
 2950 traditional (i.e., closed) help desk represents a risk to
 2951 Rubin science (e.g., many users with the same question

103 <https://rubinobservatory.org/for-scientists>

104 <https://dp1.lsst.io>

105 <https://www.sphinx-doc.org/>

106 <https://dp1.lsst.io/tutorials>

107 <https://community.lsst.org/>

2952 having to wait for responses). The open nature of the
 2953 Forum enables self-help by letting users search for sim-
 2954 ilar issues, and enables crowd-sourced problem solving
 2955 (and avoids knowledge bottlenecks) by letting users help
 2956 users.

2957 The Rubin Community Forum, and the internal staff
 2958 workflows for user support, were set up, tested, and re-
 2959 fined with /glsDP0 so that it was ready for use with
 2960 DP1.

2961 7.4. Engagement Activities

2962 A variety of live virtual and in-person workshops and
 2963 seminars offer learning opportunities to scientists and
 2964 students working with the Rubin data products, ser-
 2965 vices, and tools.

- 2966 • Rubin Science Assemblies (weekly, virtual, 1
 2967 hour): alternates between hands-on tutorials
 2968 based on the most recent data release and open
 2969 drop-in “office hours” with Rubin staff.
- 2970 • Rubin Data Academy (annual, virtual, 3-4 days):
 2971 an intense set of hands-on tutorials based on the
 2972 most recent data release, along with co-working
 2973 and networking sessions.
- 2974 • Rubin Community Workshop (annual, virtual, 5
 2975 days), a science-focused conference of contributed
 2976 posters, talks, and sessions led by members of the
 2977 Rubin science community and Rubin staff.

2978 Following the release of DP1, all of these engagement
 2979 activities focused on use of DP1 by the science commu-
 2980 nity. In particular, the 2025 Rubin Data Academy was
 2981 run the week of the DP1 release, in order to immediately
 2982 facilitate community access. The 2025 Rubin Commu-
 2983 nity Workshop had several sessions to introduce people
 2984 to the DP1 dataset and demonstrate how to access and
 2985 analyze it with the RSP.

2986 For schedules, connection information, zoom record-
 2987 ings, and associated materials, visit the For Scientists
 2988 pages of the Rubin Observatory website¹⁰⁸. Requests for
 2989 custom tutorials and presentations for research groups
 2990 are also accommodated.

2991 7.5. Users Committee

2992 This committee is charged with soliciting feedback
 2993 from the science community, advocating on their behalf,
 2994 and recommending science-driven improvements to the
 2995 LSST data products and the Rubin Science Platform

2996 tools and services. Community members are encour-
 2997 aged to attend their virtual meetings and raise issues
 2998 to their attention, so they can be included in the com-
 2999 mittee’s twice-yearly reports to the Rubin Observatory
 3000 Director.

3001 Like the Forum, the Users Committee was established
 3002 and began its work with DP0, and that feedback was
 3003 implemented for DP1. The community’s response to
 3004 DP1 will be especially valuable input to DP2 and Data
 3005 Release 1 (DR1), and the Users Committee encourages
 3006 all users to interact with them. For a list of members
 3007 and contact information, visit the For Scientists pages
 3008 of the Rubin Observatory website.

3009 7.6. Science Collaborations

3010 The eight LSST Science Collaborations are indepen-
 3011 dent, worldwide communities of scientists, self-organized
 3012 into collaborations based on their research interests and
 3013 expertise. Members work together to apply for funding,
 3014 build software infrastructure and analysis algorithms,
 3015 and incorporate external data sets into their LSST-
 3016 based research.

3017 The Science Collaborations also provide valuable ad-
 3018 vice to Rubin Observatory on the operational strategies
 3019 and data products to accomplish specific science goals,
 3020 and Rubin Observatory supports the collaborations via
 3021 staff liaisons and regular virtual meetings with Rubin
 3022 operations leadership.

3023 The Science Collaborations have been functioning for
 3024 many years, and their engagement and feedback on DP0
 3025 was implemented into the community science model for
 3026 DP1, as it will for future data releases.

3027 8. SUMMARY AND FUTURE RELEASES

3028 Rubin Data Preview 1 (DP1) offers an initial look at
 3029 the first on-sky data products and access services from
 3030 the Vera C. Rubin Observatory. DP1 forms part of Ru-
 3031 bin’s Early Science Program, and provides the sci-
 3032 entific community with an early opportunity to familiarize
 3033 themselves with the data formats and access infrastruc-
 3034 ture for the forthcoming Legacy Survey of Space and
 3035 Time. This early release has a proprietary period of two
 3036 years, during which time it is available to Rubin data
 3037 rights holders only via the cloud-based Rubin Science
 3038 Platform (RSP).

3039 In this paper we have described the completion status
 3040 of the observatory at the time of data acquisition, the
 3041 commissioning campaign that forms the basis of DP1,
 3042 and the processing pipelines used to produce early ver-
 3043 sions of data products. We provide details on the data
 3044 products, their characteristics and known issues, and
 3045 describe the Rubin Science Platform for access to and
 3046 analysis of DP1.

108 <https://rubinobservatory.org/for-scientists/events-deadlines>

3047 The data products described in this paper derive from
 3048 observations obtained by **LSSTComCam**. **LSSTCom-**
 3049 **Cam** contains only around 5% the number of CCDs as
 3050 the full LSST Science Camera (LSSTCam), yet the DP1
 3051 dataset that it has produced will already enable a very
 3052 broad range of science. At 3.5 TB in size, DP1 covers
 3053 a total area of ~ 15 deg 2 and contains 1792 single-epoch
 3054 images, 2644 deep coadded images and 2.3 million dis-
 3055 tinct astrophysical objects, including 93 new asteroid
 3056 discoveries.

3057 While some data products anticipated from the LSST
 3058 are not yet available, e.g., cell-based coadds, DP1 in-
 3059 cludes several products that will not be provided in fu-
 3060 ture releases. Notably, difference images are included in
 3061 DP1 as pre-generated products; in future releases, these
 3062 will instead be generated on demand via dedicated ser-
 3063 vices. The inclusion of pre-generated difference images
 3064 in DP1 is feasible due to the relatively small size of the
 3065 dataset, an approach that will not scale to the signifi-
 3066 cantly larger data volumes expected in subsequent re-
 3067 leases.

3068 The **RSP** is continually under development, and new
 3069 functionality will continue to be deployed incrementally
 3070 as it becomes available, and independent of the future
 3071 data release schedule. User query history capabilities,
 3072 context-aware documentation and a bulk cutout services
 3073 are just a few of the services currently under develop-
 3074 ment.

3075 Coincident with the release of DP1, Rubin Obser-
 3076 vatory begins its Science Validation Surveys with the
 3077 LSST Science Camera. This final commissioning phase
 3078 will produce a dataset that will form the foundation for
 3079 the second Rubin Data Preview, **DP2**. Full operations,
 3080 marking the start of the **LSST**, are expected to com-
 3081 mence in 2026.

3113

ACKNOWLEDGMENTS

3082 . This material is based upon work supported in part by
 3083 the National Science Foundation through Cooperative
 3084 Agreements AST-1258333 and AST-2241526 and Co-
 3085 operative Support Agreements AST-1202910 and AST-
 3086 2211468 managed by the Association of Universities for
 3087 Research in Astronomy (AURA), and the Department of
 3088 Energy under Contract No. DE-AC02-76SF00515 with
 3089 the SLAC National Accelerator Laboratory managed
 3090 by Stanford University. Additional Rubin Observatory
 3091 funding comes from private donations, grants to univer-
 3092 sities, and in-kind support from LSST-DA Institutional
 3093 Members.

3094 This work has been supported by the French Na-
 3095 tional Institute of Nuclear and Particle Physics (IN2P3)
 3096 through dedicated funding provided by the National
 3097 Center for Scientific Research (CNRS).

3098 This work has been supported by STFC fund-
 3099 ing for UK participation in LSST, through grant
 3100 ST/Y00292X/1.

3102 *Facilities:* Rubin:Simonyi (LSSTComCam), Ru-
 3103 bin:USDAC

3104 *Software:* Rubin Data Butler (T. Jenness et al.
 3105 2022), LSST Science Pipelines (Rubin Observatory
 3106 Science Pipelines Developers 2025), LSST Feature Based
 3107 Scheduler v3.0 (P. Yoachim et al. 2024; E. Naghib et al.
 3108 2019) Astropy (Astropy Collaboration et al. 2013, 2018,
 3109 2022) PIFF (M. Jarvis et al. 2021), GBDES (G. M.
 3110 Bernstein 2022), Qserv (D. L. Wang et al. 2011; F.
 3111 Mueller et al. 2023), Slurm, HTCondor, CVMFS, FTS3,
 3112 ESNet

APPENDIX

REFERENCES

3114 Abazajian, K., Adelman-McCarthy, J. K., Agüeros, M. A.,
 3115 et al. 2004, AJ, 128, 502, doi: [10.1086/421365](https://doi.org/10.1086/421365)
 3116 Ahumada, R., Allende Prieto, C., Almeida, A., et al. 2020,
 3117 ApJS, 249, 3, doi: [10.3847/1538-4365/ab929e](https://doi.org/10.3847/1538-4365/ab929e)
 3118 Aihara, H., AlSayyad, Y., Ando, M., et al. 2022, PASJ, 74,
 3119 247, doi: [10.1093/pasj/psab122](https://doi.org/10.1093/pasj/psab122)
 3120 Allbery, R. 2023, IVOA SODA implementation experience,
 3121 SQuaRE Technical Note SQR-063, NSF-DOE Vera C.
 3122 Rubin Observatory. <https://sqr-063.lsst.io/>
 3123 Allbery, R. 2024, Draft IVOA SODA web service
 3124 specification, SQuaRE Technical Note SQR-093,
 3125 NSF-DOE Vera C. Rubin Observatory.
 3126 <https://sqr-093.lsst.io/>
 3127 AlSayyad, Y. 2018, Coaddition Artifact Rejection and
 3128 CompareWarp, Data Management Technical Note
 3129 DMTN-080, NSF-DOE Vera C. Rubin Observatory,
 3130 doi: [10.71929/rubin/2583441](https://doi.org/10.71929/rubin/2583441)

3131 Ansel, J., Yang, E., He, H., et al. 2024, in 29th ACM
 3132 International Conference on Architectural Support for
 3133 Programming Languages and Operating Systems, Volume
 3134 2 (ASPLOS '24) (ACM), doi: [10.1145/3620665.3640366](https://doi.org/10.1145/3620665.3640366)

3135 Antilogus, P., Astier, P., Doherty, P., Guyonnet, A., &
 3136 Regnault, N. 2014, Journal of Instrumentation, 9,
 3137 C03048, doi: [10.1088/1748-0221/9/03/C03048](https://doi.org/10.1088/1748-0221/9/03/C03048)

3138 Astropy Collaboration, Robitaille, T. P., Tollerud, E. J.,
 3139 et al. 2013, A&A, 558, A33,
 3140 doi: [10.1051/0004-6361/201322068](https://doi.org/10.1051/0004-6361/201322068)

3141 Astropy Collaboration, Price-Whelan, A. M., Sipőcz, B. M.,
 3142 et al. 2018, AJ, 156, 123, doi: [10.3847/1538-3881/aae4f4](https://doi.org/10.3847/1538-3881/aae4f4)

3143 Astropy Collaboration, Price-Whelan, A. M., Lim, P. L.,
 3144 et al. 2022, ApJ, 935, 167, doi: [10.3847/1538-4357/ac7c74](https://doi.org/10.3847/1538-4357/ac7c74)

3145 Baumann, M., Boch, T., Pineau, F.-X., et al. 2022, in
 3146 Astronomical Society of the Pacific Conference Series,
 3147 Vol. 532, Astronomical Data Analysis Software and
 3148 Systems XXX, ed. J. E. Ruiz, F. Pierfederici, &
 3149 P. Teuben, 7

3150 Bechtol, K., Sevilla-Noarbe, I., Drlica-Wagner, A., et al.
 3151 2025, arXiv e-prints, arXiv:2501.05739,
 3152 doi: [10.48550/arXiv.2501.05739](https://doi.org/10.48550/arXiv.2501.05739)

3153 Berk, A., Anderson, G. P., Bernstein, L. S., et al. 1999, in
 3154 Society of Photo-Optical Instrumentation Engineers
 3155 (SPIE) Conference Series, Vol. 3756, Optical
 3156 Spectroscopic Techniques and Instrumentation for
 3157 Atmospheric and Space Research III, ed. A. M. Larar,
 3158 348–353, doi: [10.1117/12.366388](https://doi.org/10.1117/12.366388)

3159 Bernstein, G. M. 2022, gbdes: DECam instrumental
 3160 signature fitting and processing programs,, Astrophysics
 3161 Source Code Library, record ascl:2210.011
 3162 <http://ascl.net/2210.011>

3163 Bernstein, G. M., & Jarvis, M. 2002, AJ, 123, 583,
 3164 doi: [10.1086/338085](https://doi.org/10.1086/338085)

3165 Bernstein, G. M., Armstrong, R., Plazas, A. A., et al. 2017,
 3166 PASP, 129, 074503, doi: [10.1088/1538-3873/aa6c55](https://doi.org/10.1088/1538-3873/aa6c55)

3167 Bertin, E. 2011, in Astronomical Society of the Pacific
 3168 Conference Series, Vol. 442, Astronomical Data Analysis
 3169 Software and Systems XX, ed. I. N. Evans,
 3170 A. Accomazzi, D. J. Mink, & A. H. Rots, 435

3171 Bianco, F. B., Ivezić, Ž., Jones, R. L., et al. 2022, ApJS,
 3172 258, 1, doi: [10.3847/1538-4365/ac3e72](https://doi.org/10.3847/1538-4365/ac3e72)

3173 Blum, R., & the Rubin Operations Team. 2020, Vera C.
 3174 Rubin Observatory Data Policy, Data Management
 3175 Operations Controlled Document RDO-013, NSF-DOE
 3176 Vera C. Rubin Observatory. <https://ls.st/RDO-013>

3177 Boch, T., & Fernique, P. 2014, in Astronomical Society of
 3178 the Pacific Conference Series, Vol. 485, Astronomical
 3179 Data Analysis Software and Systems XXIII, ed.
 3180 N. Manset & P. Forshay, 277

3181 Bonnarel, F., Dowler, P., Demleitner, M., Tody, D., &
 3182 Dempsey, J. 2017, IVOA Server-side Operations for Data
 3183 Access Version 1.0,, IVOA Recommendation 17 May 2017
 3184 doi: [10.5479/ADS/bib/2017ivoa.spec.0517B](https://doi.org/10.5479/ADS/bib/2017ivoa.spec.0517B)

3185 Bonnarel, F., Fernique, P., Bienaymé, O., et al. 2000,
 3186 A&AS, 143, 33, doi: [10.1051/aas:2000331](https://doi.org/10.1051/aas:2000331)

3187 Bosch, J., Armstrong, R., Bickerton, S., et al. 2018, PASJ,
 3188 70, S5, doi: [10.1093/pasj/psx080](https://doi.org/10.1093/pasj/psx080)

3189 Broughton, A., Utsumi, Y., Plazas Malagón, A. A., et al.
 3190 2024, PASP, 136, 045003, doi: [10.1088/1538-3873/ad3aa2](https://doi.org/10.1088/1538-3873/ad3aa2)

3191 Burke, D. L., Rykoff, E. S., Allam, S., et al. 2018, AJ, 155,
 3192 41, doi: [10.3847/1538-3881/aa9f22](https://doi.org/10.3847/1538-3881/aa9f22)

3193 Chambers, K. C., Magnier, E. A., Metcalfe, N., et al. 2016,
 3194 arXiv e-prints, arXiv:1612.05560,
 3195 doi: [10.48550/arXiv.1612.05560](https://doi.org/10.48550/arXiv.1612.05560)

3196 Choi, Y., Olsen, K. A. G., Carlin, J. L., et al. 2025, arXiv
 3197 e-prints, arXiv:2507.01343,
 3198 doi: [10.48550/arXiv.2507.01343](https://doi.org/10.48550/arXiv.2507.01343)

3199 de Vaucouleurs, G. 1948, Annales d'Astrophysique, 11, 247

3200 de Vaucouleurs, G. 1953, MNRAS, 113, 134,
 3201 doi: [10.1093/mnras/113.2.134](https://doi.org/10.1093/mnras/113.2.134)

3202 Dowler, P., Bonnarel, F., & Tody, D. 2015, IVOA Simple
 3203 Image Access Version 2.0,, IVOA Recommendation 23
 3204 December 2015
 3205 doi: [10.5479/ADS/bib/2015ivoa.spec.1223D](https://doi.org/10.5479/ADS/bib/2015ivoa.spec.1223D)

3206 Dowler, P., Rixon, G., Tody, D., & Demleitner, M. 2019,
 3207 Table Access Protocol Version 1.1,, IVOA
 3208 Recommendation 27 September 2019
 3209 doi: [10.5479/ADS/bib/2019ivoa.spec.0927D](https://doi.org/10.5479/ADS/bib/2019ivoa.spec.0927D)

3210 Eggli, S., Juric, M., Moeyens, J., & Jones, L. 2020, in
 3211 AAS/Division for Planetary Sciences Meeting Abstracts,
 3212 Vol. 52, AAS/Division for Planetary Sciences Meeting
 3213 Abstracts, 211.01

3214 Esteves, J. H., Utsumi, Y., Snyder, A., et al. 2023, PASP,
 3215 135, 115003, doi: [10.1088/1538-3873/ad0a73](https://doi.org/10.1088/1538-3873/ad0a73)

3216 Euclid Collaboration, Romelli, E., Kümmel, M., et al. 2025,
 3217 arXiv e-prints, arXiv:2503.15305,
 3218 doi: [10.48550/arXiv.2503.15305](https://doi.org/10.48550/arXiv.2503.15305)

3219 Fagrelius, P., & Rykoff, E. S. 2025, Rubin Observatory
 3220 Baseline Calibration Plan, Commissioning Technical
 3221 Note SITCOMTN-086, NSF-DOE Vera C. Rubin
 3222 Observatory, doi: [10.71929/rubin/2583850](https://doi.org/10.71929/rubin/2583850)

3223 Ferguson, P. S., Rykoff, E. S., Carlin, J. L., Saunders, C., &
 3224 Parejko, J. K. 2025, The Monster: A reference catalog
 3225 with synthetic ugrizy-band fluxes for the Vera C. Rubin
 3226 observatory, Data Management Technical Note
 3227 DMTN-277, NSF-DOE Vera C. Rubin Observatory,
 3228 doi: [10.71929/rubin/2583688](https://doi.org/10.71929/rubin/2583688)

3229 Fernique, P., Allen, M. G., Boch, T., et al. 2015, A&A, 578,
 3230 A114, doi: [10.1051/0004-6361/201526075](https://doi.org/10.1051/0004-6361/201526075)

3231 Fernique, P., Allen, M., Boch, T., et al. 2017, HiPS -
 3232 Hierarchical Progressive Survey Version 1.0., IVOA
 3233 Recommendation 19 May 2017
 3234 doi: [10.5479/ADS/bib/2017ivoa.spec.0519F](https://doi.org/10.5479/ADS/bib/2017ivoa.spec.0519F)

3235 Fortino, W. F., Bernstein, G. M., Bernardinelli, P. H., et al.
 3236 2021, AJ, 162, 106, doi: [10.3847/1538-3881/ac0722](https://doi.org/10.3847/1538-3881/ac0722)

3237 Gaia Collaboration, Montegriffo, P., Bellazzini, M., et al.
 3238 2023a, A&A, 674, A33,
 3239 doi: [10.1051/0004-6361/202243709](https://doi.org/10.1051/0004-6361/202243709)

3240 Gaia Collaboration, Vallenari, A., Brown, A. G. A., et al.
 3241 2023b, A&A, 674, A1, doi: [10.1051/0004-6361/202243940](https://doi.org/10.1051/0004-6361/202243940)

3242 Górski, K. M., Hivon, E., Banday, A. J., et al. 2005, ApJ,
 3243 622, 759, doi: [10.1086/427976](https://doi.org/10.1086/427976)

3244 Graham, A. W., & Driver, S. P. 2005, PASA, 22, 118,
 3245 doi: [10.1071/AS05001](https://doi.org/10.1071/AS05001)

3246 Graham, M., Plante, R., Tody, D., & Fitzpatrick, M. 2014,
 3247 PyVO: Python access to the Virtual Observatory,,
 3248 Astrophysics Source Code Library, record ascl:1402.004

3249 Graham, M. L., Carlin, J. L., Adair, C. L., et al. 2025,
 3250 Guidelines for User Tutorials, Technical Note RTN-045,
 3251 NSF-DOE Vera C. Rubin Observatory,
 3252 doi: [10.71929/rubin/2584020](https://doi.org/10.71929/rubin/2584020)

3253 Gray, B. 2025, find_orb: Orbit determination from
 3254 observations, https://github.com/Bill-Gray/find_orb

3255 Guy, L. P., Bechtol, K., Bellm, E., et al. 2025, Rubin
 3256 Observatory Plans for an Early Science Program,
 3257 Technical Note RTN-011, NSF-DOE Vera C. Rubin
 3258 Observatory, doi: [10.71929/rubin/2584021](https://doi.org/10.71929/rubin/2584021)

3259 Heinze, A., Eggel, S., Juric, M., et al. 2022, in AAS/Division
 3260 for Planetary Sciences Meeting Abstracts, Vol. 54,
 3261 AAS/Division for Planetary Sciences Meeting Abstracts,
 3262 504.04

3263 Heinze, A., Juric, M., & Kurlander, J. 2023, heliolinx: Open
 3264 Source Solar System Discovery Software,
 3265 <https://github.com/heliolinx/heliolinx>

3266 Hirata, C., & Seljak, U. 2003, MNRAS, 343, 459,
 3267 doi: [10.1046/j.1365-8711.2003.06683.x](https://doi.org/10.1046/j.1365-8711.2003.06683.x)

3268 Holman, M. J., Payne, M. J., Blankley, P., Janssen, R., &
 3269 Kuindersma, S. 2018, AJ, 156, 135,
 3270 doi: [10.3847/1538-3881/aad69a](https://doi.org/10.3847/1538-3881/aad69a)

3271 Howard, J., Reil, K., Claver, C., et al. 2018, in Society of
 3272 Photo-Optical Instrumentation Engineers (SPIE)
 3273 Conference Series, Vol. 10700, Ground-based and
 3274 Airborne Telescopes VII, ed. H. K. Marshall &
 3275 J. Spyromilio, 107003D, doi: [10.1117/12.2312684](https://doi.org/10.1117/12.2312684)

3276 Illingworth, G., Magee, D., Bouwens, R., et al. 2016, arXiv
 3277 e-prints, arXiv:1606.00841,
 3278 doi: [10.48550/arXiv.1606.00841](https://doi.org/10.48550/arXiv.1606.00841)

3279 Ingraham, P., Fagrelius, P., Stubbs, C. W., et al. 2022, in
 3280 Society of Photo-Optical Instrumentation Engineers
 3281 (SPIE) Conference Series, Vol. 12182, Ground-based and
 3282 Airborne Telescopes IX, ed. H. K. Marshall,
 3283 J. Spyromilio, & T. Usuda, 121820R,
 3284 doi: [10.1117/12.2630185](https://doi.org/10.1117/12.2630185)

3285 Ivezić, Ž., Kahn, S. M., Tyson, J. A., et al. 2019a, ApJ,
 3286 873, 111, doi: [10.3847/1538-4357/ab042c](https://doi.org/10.3847/1538-4357/ab042c)

3287 Ivezić, Ž., Kahn, S. M., Tyson, J. A., et al. 2019b, ApJ,
 3288 873, 111, doi: [10.3847/1538-4357/ab042c](https://doi.org/10.3847/1538-4357/ab042c)

3289 Jarvis, M., et al. 2021, Mon. Not. Roy. Astron. Soc., 501,
 3290 1282, doi: [10.1093/mnras/staa3679](https://doi.org/10.1093/mnras/staa3679)

3291 Jenness, T., & Dubois-Felsmann, G. P. 2025, IVOA
 3292 Identifier Usage at the Rubin Observatory, Data
 3293 Management Technical Note DMTN-302, NSF-DOE Vera
 3294 C. Rubin Observatory, doi: [10.71929/rubin/2583848](https://doi.org/10.71929/rubin/2583848)

3295 Jenness, T., Voutsinas, S., Dubois-Felsmann, G. P., &
 3296 Salnikov, A. 2024, arXiv e-prints, arXiv:2501.00544,
 3297 doi: [10.48550/arXiv.2501.00544](https://doi.org/10.48550/arXiv.2501.00544)

3298 Jenness, T., Bosch, J. F., Salnikov, A., et al. 2022, in
 3299 Society of Photo-Optical Instrumentation Engineers
 3300 (SPIE) Conference Series, Vol. 12189, Software and
 3301 Cyberinfrastructure for Astronomy VII, 1218911,
 3302 doi: [10.1117/12.2629569](https://doi.org/10.1117/12.2629569)

3303 Jones, R. L., Yoachim, P., Ivezić, Ž., Neilsen Jr., E. H., &
 3304 Ribeiro, T. 2021, Survey Strategy and Cadence Choices
 3305 for the Vera C. Rubin Observatory Legacy Survey of
 3306 Space and Time (LSST), Project Science Technical Note
 3307 PSTN-051, NSF-DOE Vera C. Rubin Observatory,
 3308 doi: [10.71929/rubin/2584084](https://doi.org/10.71929/rubin/2584084)

3309 Juric, M. 2025, mpsky: Multi-purpose sky catalog
 3310 cross-matching, <https://github.com/mjuric/mpsky>

3311 Jurić, M., Ciardi, D., Dubois-Felsmann, G., & Guy, L.
 3312 2019, LSST Science Platform Vision Document, Systems
 3313 Engineering Controlled Document LSE-319, NSF-DOE
 3314 Vera C. Rubin Observatory, doi: [10.71929/rubin/2587242](https://doi.org/10.71929/rubin/2587242)

3315 Jurić, M., Axelrod, T. S., Becker, A. C., et al. 2023, Data
 3316 Products Definition Document, Systems Engineering
 3317 Controlled Document LSE-163, NSF-DOE Vera C. Rubin
 3318 Observatory, doi: [10.71929/rubin/2587118](https://doi.org/10.71929/rubin/2587118)

3319 Kannawadi, A. 2025, Consistent galaxy colors with
 3320 Gaussian-Aperture and PSF photometry, Data
 3321 Management Technical Note DMTN-190, NSF-DOE Vera
 3322 C. Rubin Observatory, doi: [10.71929/rubin/2583849](https://doi.org/10.71929/rubin/2583849)

3323 Kron, R. G. 1980, ApJS, 43, 305, doi: [10.1086/190669](https://doi.org/10.1086/190669)

3324 Kuijken, K. 2008, A&A, 482, 1053,
 3325 doi: [10.1051/0004-6361:20066601](https://doi.org/10.1051/0004-6361:20066601)

3326 Lange, T., Nordby, M., Pollek, H., et al. 2024, in Society of
 3327 Photo-Optical Instrumentation Engineers (SPIE)
 3328 Conference Series, Vol. 13096, Ground-based and
 3329 Airborne Instrumentation for Astronomy X, ed. J. J.
 3330 Bryant, K. Motohara, & J. R. D. Vernet, 130961O,
 3331 doi: [10.1117/12.3019302](https://doi.org/10.1117/12.3019302)

3332 Léget, P. F., Astier, P., Regnault, N., et al. 2021, A&A,
 3333 650, A81, doi: [10.1051/0004-6361/202140463](https://doi.org/10.1051/0004-6361/202140463)

3334 Lim, K.-T. 2023, Proposal and Prototype for Prompt
 3335 Processing, Data Management Technical Note
 3336 DMTN-219, NSF-DOE Vera C. Rubin Observatory,
 3337 doi: [10.71929/rubin/2585429](https://doi.org/10.71929/rubin/2585429)

3338 Lim, K.-T. 2025, The Consolidated Database of Image
 3339 Metadata, Data Management Technical Note
 3340 DMTN-227, NSF-DOE Vera C. Rubin Observatory,
 3341 doi: [10.71929/rubin/2586436](https://doi.org/10.71929/rubin/2586436)

3342 Louys, M., Tody, D., Dowler, P., et al. 2017, Observation
 3343 Data Model Core Components, its Implementation in the
 3344 Table Access Protocol Version 1.1., IVOA
 3345 Recommendation 09 May 2017
 3346 doi: [10.5479/ADS/bib/2017ivoa.spec.0509L](https://doi.org/10.5479/ADS/bib/2017ivoa.spec.0509L)

3347 LSST Dark Energy Science Collaboration (LSST DESC),
 3348 Abolfathi, B., Alonso, D., et al. 2021, ApJS, 253, 31,
 3349 doi: [10.3847/1538-4365/abd62c](https://doi.org/10.3847/1538-4365/abd62c)

3350 Lupton, R., Blanton, M. R., Fekete, G., et al. 2004, PASP,
 3351 116, 133, doi: [10.1086/382245](https://doi.org/10.1086/382245)

3352 Lust, N. B., Jenness, T., Bosch, J. F., et al. 2023, arXiv
 3353 e-prints, arXiv:2303.03313,
 3354 doi: [10.48550/arXiv.2303.03313](https://doi.org/10.48550/arXiv.2303.03313)

3355 Mandelbaum, R., Hirata, C. M., Seljak, U., et al. 2005,
 3356 MNRAS, 361, 1287,
 3357 doi: [10.1111/j.1365-2966.2005.09282.x](https://doi.org/10.1111/j.1365-2966.2005.09282.x)

3358 Megias Homar, G., Kahn, S. M., Meyers, J. M., Crenshaw,
 3359 J. F., & Thomas, S. J. 2024, The Astrophysical Journal,
 3360 974, 108, doi: [10.3847/1538-4357/ad6cdc](https://doi.org/10.3847/1538-4357/ad6cdc)

3361 Megias Homar, G., Tighe, R., Thomas, S., et al. 2024, in
 3362 Ground-based and Airborne Telescopes X, ed. H. K.
 3363 Marshall, J., Spyromilio, & T. Usuda, Vol. 13094,
 3364 International Society for Optics and Photonics (SPIE),
 3365 130943C, doi: [10.1117/12.3019031](https://doi.org/10.1117/12.3019031)

3366 Melchior, P., Moolekamp, F., Jerdee, M., et al. 2018,
 3367 Astronomy and Computing, 24, 129,
 3368 doi: [10.1016/j.ascom.2018.07.001](https://doi.org/10.1016/j.ascom.2018.07.001)

3369 Mueller, F., et al. 2023, in ASP Conf. Ser., Vol. TBD,
 3370 ADASS XXXII, ed. S. Gaudet, S. Gwyn, P. Dowler,
 3371 D. Bohlender, & A. Hincks (San Francisco: ASP), in
 3372 press. <https://dmtn-243.lsst.io>

3373 Naghib, E., Yoachim, P., Vanderbei, R. J., Connolly, A. J.,
 3374 & Jones, R. L. 2019, The Astronomical Journal, 157, 151,
 3375 doi: [10.3847/1538-3881/aafece](https://doi.org/10.3847/1538-3881/aafece)

3376 NSF-DOE Vera C. Rubin Observatory. 2025a, Legacy
 3377 Survey of Space and Time Data Preview 1 [Data set],
 3378 NSF-DOE Vera C. Rubin Observatory,
 3379 doi: [10.71929/RUBIN/2570308](https://doi.org/10.71929/RUBIN/2570308)

3380 NSF-DOE Vera C. Rubin Observatory. 2025b, Legacy
 3381 Survey of Space and Time Data Preview 1: raw dataset
 3382 type [Data set], NSF-DOE Vera C. Rubin Observatory,
 3383 doi: [10.71929/RUBIN/2570310](https://doi.org/10.71929/RUBIN/2570310)

3384 NSF-DOE Vera C. Rubin Observatory. 2025c, Legacy
 3385 Survey of Space and Time Data Preview 1: visit_image
 3386 dataset type [Data set], NSF-DOE Vera C. Rubin
 3387 Observatory, doi: [10.71929/RUBIN/2570311](https://doi.org/10.71929/RUBIN/2570311)

3388 NSF-DOE Vera C. Rubin Observatory. 2025d, Legacy
 3389 Survey of Space and Time Data Preview 1: deep_coadd
 3390 dataset type [Data set], NSF-DOE Vera C. Rubin
 3391 Observatory, doi: [10.71929/RUBIN/2570313](https://doi.org/10.71929/RUBIN/2570313)

3392 NSF-DOE Vera C. Rubin Observatory. 2025e, Legacy
 3393 Survey of Space and Time Data Preview 1:
 3394 template_coadd dataset type [Data set], NSF-DOE Vera
 3395 C. Rubin Observatory, doi: [10.71929/RUBIN/2570314](https://doi.org/10.71929/RUBIN/2570314)

3396 NSF-DOE Vera C. Rubin Observatory. 2025f, Legacy
 3397 Survey of Space and Time Data Preview 1:
 3398 difference_image dataset type [Data set], NSF-DOE Vera
 3399 C. Rubin Observatory, doi: [10.71929/RUBIN/2570312](https://doi.org/10.71929/RUBIN/2570312)

3400 NSF-DOE Vera C. Rubin Observatory. 2025g, Legacy
 3401 Survey of Space and Time Data Preview 1: Source
 3402 searchable catalog [Data set], NSF-DOE Vera C. Rubin
 3403 Observatory, doi: [10.71929/RUBIN/2570323](https://doi.org/10.71929/RUBIN/2570323)

3404 NSF-DOE Vera C. Rubin Observatory. 2025h, Legacy
 3405 Survey of Space and Time Data Preview 1: Object
 3406 searchable catalog [Data set], NSF-DOE Vera C. Rubin
 3407 Observatory, doi: [10.71929/RUBIN/2570325](https://doi.org/10.71929/RUBIN/2570325)

3408 NSF-DOE Vera C. Rubin Observatory. 2025i, Legacy
 3409 Survey of Space and Time Data Preview 1: ForcedSource
 3410 searchable catalog [Data set], NSF-DOE Vera C. Rubin
 3411 Observatory, doi: [10.71929/RUBIN/2570327](https://doi.org/10.71929/RUBIN/2570327)

3412 NSF-DOE Vera C. Rubin Observatory. 2025j, Legacy
 3413 Survey of Space and Time Data Preview 1: DiaSource
 3414 searchable catalog [Data set], NSF-DOE Vera C. Rubin
 3415 Observatory, doi: [10.71929/RUBIN/2570317](https://doi.org/10.71929/RUBIN/2570317)

3416 NSF-DOE Vera C. Rubin Observatory. 2025k, Legacy
 3417 Survey of Space and Time Data Preview 1: DiaObject
 3418 searchable catalog [Data set], NSF-DOE Vera C. Rubin
 3419 Observatory, doi: [10.71929/RUBIN/2570319](https://doi.org/10.71929/RUBIN/2570319)

3420 NSF-DOE Vera C. Rubin Observatory. 2025l, Legacy
 3421 Survey of Space and Time Data Preview 1:
 3422 ForcedSourceOnDiaObject searchable catalog [Data set],
 3423 NSF-DOE Vera C. Rubin Observatory,
 3424 doi: [10.71929/RUBIN/2570321](https://doi.org/10.71929/RUBIN/2570321)

3425 NSF-DOE Vera C. Rubin Observatory. 2025m, Legacy
 3426 Survey of Space and Time Data Preview 1: SSOObject
 3427 searchable catalog [Data set], NSF-DOE Vera C. Rubin
 3428 Observatory, doi: [10.71929/RUBIN/2570335](https://doi.org/10.71929/RUBIN/2570335)

3429 NSF-DOE Vera C. Rubin Observatory. 2025n, Legacy
 3430 Survey of Space and Time Data Preview 1: SSSource
 3431 searchable catalog [Data set], NSF-DOE Vera C. Rubin
 3432 Observatory, doi: [10.71929/RUBIN/2570333](https://doi.org/10.71929/RUBIN/2570333)

3433 NSF-DOE Vera C. Rubin Observatory. 2025o, Legacy
 3434 Survey of Space and Time Data Preview 1: CcdVisit
 3435 searchable catalog [Data set], NSF-DOE Vera C. Rubin
 3436 Observatory, doi: [10.71929/RUBIN/2570331](https://doi.org/10.71929/RUBIN/2570331)

3437 NSF-DOE Vera C. Rubin Observatory. 2025p, Legacy
 3438 Survey of Space and Time Data Preview 1: survey
 3439 property dataset type [Data set], NSF-DOE Vera C.
 3440 Rubin Observatory, doi: [10.71929/RUBIN/2570315](https://doi.org/10.71929/RUBIN/2570315)

3441 Observatory, N.-D. V. C. R. 2021, Rubin Observatory
 3442 LSST Tutorials [Computer Software], NSF-DOE Vera C.
 3443 Rubin Observatory, doi: [10.11578/rubin/dc.20250909.20](https://doi.org/10.11578/rubin/dc.20250909.20)

3444 Oke, J. B., & Gunn, J. E. 1983, *ApJ*, 266, 713,
 3445 doi: [10.1086/160817](https://doi.org/10.1086/160817)

3446 O'Mullane, W., Economou, F., Huang, F., et al. 2024a, in
 3447 Astronomical Society of the Pacific Conference Series,
 3448 Vol. 535, Astromical Data Analysis Software and Systems
 3449 XXXI, ed. B. V. Hugo, R. Van Rooyen, & O. M.
 3450 Smirnov, 227, doi: [10.48550/arXiv.2111.15030](https://doi.org/10.48550/arXiv.2111.15030)

3451 O'Mullane, W., AlSayyad, Y., Chiang, J., et al. 2024b, in
 3452 Society of Photo-Optical Instrumentation Engineers
 3453 (SPIE) Conference Series, Vol. 13101, Software and
 3454 Cyberinfrastructure for Astronomy VIII, ed. J. Ibsen &
 3455 G. Chiozzi, 131012B, doi: [10.1117/12.3018005](https://doi.org/10.1117/12.3018005)

3456 Onken, C. A., Wolf, C., Bessell, M. S., et al. 2019, *PASA*,
 3457 36, e033, doi: [10.1017/pasa.2019.27](https://doi.org/10.1017/pasa.2019.27)

3458 Park, H. Y., Nomerotski, A., & Tsybychev, D. 2017,
 3459 *Journal of Instrumentation*, 12, C05015,
 3460 doi: [10.1088/1748-0221/12/05/C05015](https://doi.org/10.1088/1748-0221/12/05/C05015)

3461 Petrosian, V. 1976, *ApJL*, 210, L53,
 3462 doi: [10.1086/18230110.1086/182253](https://doi.org/10.1086/18230110.1086/182253)

3463 Plazas, A. A., Shapiro, C., Smith, R., Huff, E., & Rhodes,
 3464 J. 2018, *Publications of the Astronomical Society of the*
 3465 *Pacific*, 130, 065004, doi: [10.1088/1538-3873/aab820](https://doi.org/10.1088/1538-3873/aab820)

3466 Plazas Malagón, A. A., Digel, S. W., Roodman, A.,
 3467 Broughton, A., & LSST Camera Team. 2025, LSSTCam
 3468 and LSSTComCam Focal Plane Layouts, Camera
 3469 Technical Note CTN-001, NSF-DOE Vera C. Rubin
 3470 Observatory, doi: [10.71929/rubin/2584019](https://doi.org/10.71929/rubin/2584019)

3471 Plazas Malagón, A. A., Waters, C., Broughton, A., et al.
 3472 2025, *Journal of Astronomical Telescopes, Instruments,*
 3473 and Systems, 11, 011209,
 3474 doi: [10.1117/1.JATIS.11.1.011209](https://doi.org/10.1117/1.JATIS.11.1.011209)

3475 Refregier, A. 2003, *ARA&A*, 41, 645,
 3476 doi: [10.1146/annurev.astro.41.111302.102207](https://doi.org/10.1146/annurev.astro.41.111302.102207)

3477 Reiss, D. J., & Lupton, R. H. 2016, Implementation of
 3478 Image Difference Decorrelation, Data Management
 3479 Technical Note DMTN-021, NSF-DOE Vera C. Rubin
 3480 Observatory, doi: [10.71929/rubin/2586490](https://doi.org/10.71929/rubin/2586490)

3481 Roodman, A., Rasmussen, A., Bradshaw, A., et al. 2024, in
 3482 Society of Photo-Optical Instrumentation Engineers
 3483 (SPIE) Conference Series, Vol. 13096, Ground-based and
 3484 Airborne Instrumentation for Astronomy X, ed. J. J.
 3485 Bryant, K. Motohara, & J. R. D. Vernet, 130961S,
 3486 doi: [10.1117/12.3019698](https://doi.org/10.1117/12.3019698)

3487 Rubin, V. C., & Ford, Jr., W. K. 1970, *ApJ*, 159, 379,
 3488 doi: [10.1086/150317](https://doi.org/10.1086/150317)

3489 Rubin, V. C., Ford, Jr., W. K., & Thonnard, N. 1980, *ApJ*,
 3490 238, 471, doi: [10.1086/158003](https://doi.org/10.1086/158003)

3491 Rubin Observatory Science Pipelines Developers. 2025, The
 3492 LSST Science Pipelines Software: Optical Survey
 3493 Pipeline Reduction and Analysis Environment, Project
 3494 Science Technical Note PSTN-019, NSF-DOE Vera C.
 3495 Rubin Observatory, doi: [10.71929/rubin/2570545](https://doi.org/10.71929/rubin/2570545)

3496 Rubin's Survey Cadence Optimization Committee, Bauer,
 3497 F. E., Brough, S., et al. 2022, Survey Cadence
 3498 Optimization Committee's Phase 1 Recommendation,
 3499 Project Science Technical Note PSTN-053, NSF-DOE
 3500 Vera C. Rubin Observatory, doi: [10.71929/rubin/2584276](https://doi.org/10.71929/rubin/2584276)

3501 Rubin's Survey Cadence Optimization Committee, Bauer,
 3502 F. E., Bianco, F. B., et al. 2023, Survey Cadence
 3503 Optimization Committee's Phase 2 Recommendations,
 3504 Project Science Technical Note PSTN-055, NSF-DOE
 3505 Vera C. Rubin Observatory, doi: [10.71929/rubin/2585249](https://doi.org/10.71929/rubin/2585249)

3506 Rubin's Survey Cadence Optimization Committee, Bianco,
 3507 F. B., Jones, R. L., et al. 2025, Survey Cadence
 3508 Optimization Committee's Phase 3 Recommendations,
 3509 Project Science Technical Note PSTN-056, NSF-DOE
 3510 Vera C. Rubin Observatory, doi: [10.71929/rubin/2585402](https://doi.org/10.71929/rubin/2585402)

3511 Rykoff, E. S., Tucker, D. L., Burke, D. L., et al. 2023, arXiv
 3512 e-prints, arXiv:2305.01695,
 3513 doi: [10.48550/arXiv.2305.01695](https://doi.org/10.48550/arXiv.2305.01695)

3514 Saunders, C. 2024, Astrometric Calibration in the LSST
 3515 Pipeline, Data Management Technical Note DMTN-266,
 3516 NSF-DOE Vera C. Rubin Observatory,
 3517 doi: [10.71929/rubin/2583846](https://doi.org/10.71929/rubin/2583846)

3518 Schutt, T., Jarvis, M., Roodman, A., et al. 2025, The Open
 3519 Journal of Astrophysics, 8, 26, doi: [10.33232/001c.132299](https://doi.org/10.33232/001c.132299)

3520 Sérsic, J. L. 1963, *Boletin de la Asociacion Argentina de*
 3521 *Astronomia La Plata Argentina*, 6, 41

3522 Sérsic, J. L. 1968, *Atlas de Galaxias Australes (Cordoba,*
 3523 *Argentina: Observatorio Astronomico)*

3524 Shanks, T., Metcalfe, N., Chehade, B., et al. 2015,
 3525 *MNRAS*, 451, 4238, doi: [10.1093/mnras/stv1130](https://doi.org/10.1093/mnras/stv1130)

3526 SLAC National Accelerator Laboratory, & NSF-DOE Vera
 3527 C. Rubin Observatory. 2024, LSST Commissioning
 3528 Camera, SLAC National Accelerator Laboratory (SLAC),
 3529 Menlo Park, CA (United States),
 3530 doi: [10.71929/RUBIN/2561361](https://doi.org/10.71929/RUBIN/2561361)

3531 Slater, C. T., Ivezić, Ž., & Lupton, R. H. 2020, *AJ*, 159, 65,
 3532 doi: [10.3847/1538-3881/ab6166](https://doi.org/10.3847/1538-3881/ab6166)

3533 Smith, G. E. 2010, *Rev. Mod. Phys.*, 82, 2307,
 3534 doi: [10.1103/RevModPhys.82.2307](https://doi.org/10.1103/RevModPhys.82.2307)

3535 Stalder, B., Reil, K., Claver, C., et al. 2020, in Society of
 3536 Photo-Optical Instrumentation Engineers (SPIE)
 3537 Conference Series, Vol. 11447, Ground-based and
 3538 Airborne Instrumentation for Astronomy VIII, ed. C. J.
 3539 Evans, J. J. Bryant, & K. Motohara, 114470L,
 3540 doi: [10.1117/12.2561132](https://doi.org/10.1117/12.2561132)

3541 Stalder, B., Reil, K., Aguilar, C., et al. 2022, in Society of
 3542 Photo-Optical Instrumentation Engineers (SPIE)
 3543 Conference Series, Vol. 12184, Ground-based and
 3544 Airborne Instrumentation for Astronomy IX, ed. C. J.
 3545 Evans, J. J. Bryant, & K. Motohara, 121840J,
 3546 doi: [10.1117/12.2630184](https://doi.org/10.1117/12.2630184)

3547 Stalder, B., Munoz, F., Aguilar, C., et al. 2024, in Society
 3548 of Photo-Optical Instrumentation Engineers (SPIE)
 3549 Conference Series, Vol. 13094, Ground-based and
 3550 Airborne Telescopes X, ed. H. K. Marshall, J. Spyromilio,
 3551 & T. Usuda, 1309409, doi: [10.1117/12.3019266](https://doi.org/10.1117/12.3019266)

3552 Swinbank, J. D., Axelrod, T. S., Becker, A. C., et al. 2020,
 3553 Data Management Science Pipelines Design, Data
 3554 Management Controlled Document LDM-151, NSF-DOE
 3555 Vera C. Rubin Observatory, doi: [10.71929/rubin/2587108](https://doi.org/10.71929/rubin/2587108)

3556 Taranu, D. S. 2025, The MultiProFit astronomical source
 3557 modelling code, Data Management Technical Note
 3558 DMTN-312, NSF-DOE Vera C. Rubin Observatory,
 3559 doi: [10.71929/rubin/2584108](https://doi.org/10.71929/rubin/2584108)

3560 Taylor, M. 2011, TOPCAT: Tool for OPerations on
 3561 Catalogues And Tables,, *Astrophysics Source Code*
 3562 Library, record ascl:1101.010

3563 Thomas, S., Connolly, A., Crenshaw, J. F., et al. 2023, in
 3564 Adaptive Optics for Extremely Large Telescopes
 3565 (AO4ELT7), 67, doi: [10.13009/AO4ELT7-2023-069](https://doi.org/10.13009/AO4ELT7-2023-069)

3566 Tonry, J. L., Denneau, L., Heinze, A. N., et al. 2018, *PASP*,
 3567 130, 064505, doi: [10.1088/1538-3873/aabadf](https://doi.org/10.1088/1538-3873/aabadf)

3568 Wainer, T. M., Davenport, J. R. A., Bellm, E. C., et al.
 3569 2025, *Research Notes of the American Astronomical*
 3570 *Society*, 9, 171, doi: [10.3847/2515-5172/adecef](https://doi.org/10.3847/2515-5172/adecef)

3571 Wang, D. L., Monkewitz, S. M., Lim, K.-T., & Becla, J.
 3572 2011, in *State of the Practice Reports, SC '11* (New
 3573 York, NY, USA: ACM), 12:1–12:11,
 3574 doi: [10.1145/2063348.2063364](https://doi.org/10.1145/2063348.2063364)

3575 Waters, C. Z., Magnier, E. A., Price, P. A., et al. 2020,
 3576 *ApJS*, 251, 4, doi: [10.3847/1538-4365/abb82b](https://doi.org/10.3847/1538-4365/abb82b)

3577 Whitaker, K. E., Ashas, M., Illingworth, G., et al. 2019,
 3578 *ApJS*, 244, 16, doi: [10.3847/1538-4365/ab3853](https://doi.org/10.3847/1538-4365/ab3853)

3579 Wu, X., Roby, W., Goldian, T., et al. 2019, in *Astronomical*
 3580 *Society of the Pacific Conference Series*, Vol. 521,
 3581 *Astronomical Data Analysis Software and Systems*
 3582 XXVI, ed. M. Molinaro, K. Shortridge, & F. Pasian, 32

3583 Xin, B., Claver, C., Liang, M., et al. 2015, *ApOpt*, 54,
 3584 9045, doi: [10.1364/AO.54.009045](https://doi.org/10.1364/AO.54.009045)

3585 Yoachim, P. 2022, *Survey Strategy: Rolling Cadence,*
 3586 *Project Science Technical Note PSTN-052*, NSF-DOE
 3587 Vera C. Rubin Observatory, doi: [10.71929/rubin/2584109](https://doi.org/10.71929/rubin/2584109)

3588 Yoachim, P., Jones, L., Eric H. Nielsen, J., & Becker, M. R.
 3589 2024, *lsst/rubin_scheduler*: v3.0.0, v3.0.0 Zenodo,
 3590 doi: [10.5281/zenodo.13985198](https://doi.org/10.5281/zenodo.13985198)

3591 Zhang, T., Almoubayyed, H., Mandelbaum, R., et al. 2023,
 3592 *MNRAS*, 520, 2328, doi: [10.1093/mnras/stac3350](https://doi.org/10.1093/mnras/stac3350)